

SYNTHESIS AND STABILITY OF PEROVSKITE OXYNITRIDES

BY

MATTHEW R. BROPHY

A THESIS

SUBMITTED TO THE FACULTY OF

ALFRED UNIVERSITY

IN PARTIAL FULFILLMENT OF THE REQUIREMENTS  
FOR THE DEGREE OF

DOCTOR OF PHILOSOPHY

IN

CERAMICS

ALFRED, NEW YORK

DECEMBER, 2010

Alfred University theses are copyright protected and may be used for education or personal research only. Reproduction or distribution in part or whole is prohibited without written permission from the author.

Signature page may be viewed at Scholes Library, New York State College of Ceramics, Alfred University, Alfred, New York.

SYNTHESIS AND STABILITY OF PEROVSKITE OXYNITRIDES

BY

MATTHEW R. BROPHY

B.S. ALFRED UNIVERSITY (2005)

SIGNATURE OF AUTHOR \_\_\_\_\_ (Signature on file) \_\_\_\_\_ (S

APPROVED BY \_\_\_\_\_ (Signature on file)  
WALTER A. SCHULZE, ADVISOR

\_\_\_\_\_  
(Signature on file)  
NATHAN MELLOTT, ADVISORY COMMITTEE

\_\_\_\_\_  
(Signature on file)  
SCOTT MISTURE, ADVISORY COMMITTEE

\_\_\_\_\_  
(Signature on file)  
DOREEN EDWARDS, ADVISORY COMMITTEE

\_\_\_\_\_  
(Signature on file)  
STEVEN PILGRIM, ADVISORY COMMITTEE

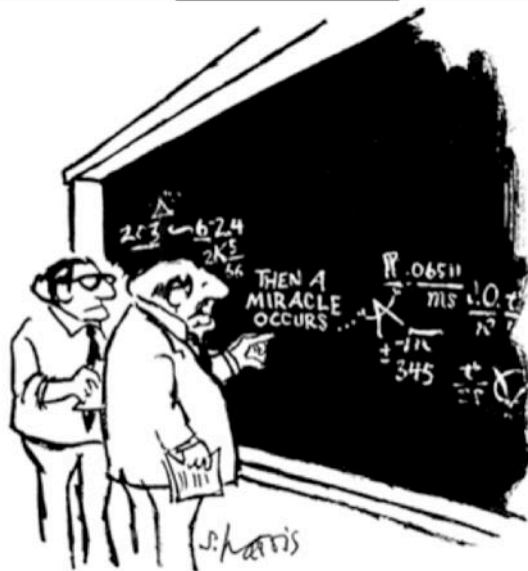
\_\_\_\_\_  
(Signature on file)  
WILLIAM B. CARLSON, CHAIR, ORAL THESIS DEFENSE

ACCEPTED BY \_\_\_\_\_ (Signature on file)  
DOREEN D. EDWARDS, DEAN  
KAZUO INAMORI SCHOOL OF ENGINEERING

ACCEPTED BY \_\_\_\_\_ (Signature on file)  
NANCY J. EVANGELISTA, ASSOCIATE PROVOST  
FOR GRADUATE AND PROFESSIONAL PROGRAMS  
ALFRED UNIVERSITY

## ACKNOWLEDGMENTS

### Dr. Schulze



"I think you should be more explicit here in step two"

### Committee

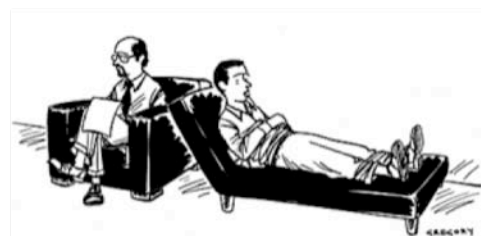


"Have you tried Googling that?"

### Peers



### Family



"Could we up the dosage?  
I still have feeling"

# TABLE OF CONTENTS

	<b>Page</b>
Acknowledgments .....	vi
Table of Contents.....	vii
List of Tables.....	xi
List of Figures.....	xii
<b>ABSTRACT.....</b>	<b>2</b>
<b>1 MOTIVATION.....</b>	<b>4</b>
<b>2 NITRIDING WITH AMMONIA.....</b>	<b>6</b>
2.1 INTRODUCTION .....	6
2.1.1 Motivation .....	6
2.1.2 Literature Review.....	6
2.1.3 Work Plan.....	8
2.2 EXPERIMENTAL .....	8
2.2.1 Ammonia Concentration Measurement.....	8
2.3 RESULTS AND DISCUSSION .....	10
2.3.1 Temperature Distribution .....	10
2.3.2 Maximum Temperature and Flow Velocity.....	11
2.3.3 Sample Placement and Furnace Configuration .....	12
2.4 CONCLUSION.....	15
<b>3 SOLID STATE POWDER SYNTHESIS.....</b>	<b>16</b>
3.1 INTRODUCTION .....	16
3.1.1 Motivation .....	16
3.1.2 Literature.....	16
3.1.3 Work Plan.....	17
3.2 EXPERIMENTAL .....	18
3.2.1 Precursor Formation.....	18
3.2.2 Ammonolysis Reaction .....	19
3.2.3 Powder X-Ray Diffraction.....	19
3.2.4 Chemical Composition Analysis.....	19
3.2.5 X-Ray Photoelectron Spectroscopy (XPS) .....	20
3.2.6 Environmental Scanning Electron Microscopy (ESEM) .....	20
3.3 RESULTS AND DISCUSSION .....	21
3.3.1 Sample Position .....	21

3.3.2 Flow velocity .....	25
3.3.3 A-Site Exchange .....	27
<b>3.3.3.1 Cation Stoichiometry</b> .....	33
3.3.4 Temperature.....	41
3.3.5 Furnace Configuration.....	43
3.3.6 Precursor Form .....	44
<b>3.3.6.1 Reaction Rate (Powder XRD)</b> .....	45
<b>3.3.6.2 Perovskite Structure (Powder XRD)</b> .....	47
<b>3.3.6.3 Anion Composition (LECO Hot-Gas Extraction)</b> .....	49
<b>3.3.6.4 Powder Microstructure (SEM)</b> .....	50
3.6 CONCLUSION.....	51
<b>4 STABILITY AND SINTERING .....</b>	<b>53</b>
4.1 INTRODUCTION .....	53
4.1.1 Motivation .....	53
4.1.2 Literature Review.....	53
<b>4.1.2.1 Oxynitride and Nitride Stability</b> .....	53
<b>4.1.2.2 Perovskite Oxynitride Stability</b> .....	54
<b>4.1.2.3 Nitride and Oxynitride Sintering</b> .....	55
4.1.3 Work Plan.....	56
4.2 EXPERIMENTAL .....	57
4.2.1 Powder Synthesis.....	57
4.2.2 Thermogravimetric Analysis .....	57
4.2.3 <i>In situ</i> , High Temperature DRIFT.....	57
4.2.4 <i>In situ</i> , High Temperature XRD.....	58
4.2.5 Room Temperature Powder XRD.....	58
4.2.6 XPS .....	58
4.2.7 Gas Overpressure.....	59
4.2.8 Axial Pressure (Spark Plasma Sintering).....	59
4.3 RESULTS AND DISCUSSION .....	60
4.3.1 Thermal Stability .....	60
<b>4.3.1.1 Thermogravimetric Analysis</b> .....	60
<b>4.3.1.2 In situ High Temperature XRD</b> .....	63
4.3.2 Sintering .....	65
<b>4.3.2.1 Pressure-less Sintering</b> .....	65
<b>4.3.2.2 Gas Overpressure</b> .....	69
<b>4.3.2.3 Spark Plasma Sintering</b> .....	73

4.4 CONCLUSION.....	77
<b>5 WET CHEMISTRY TACTICS .....</b>	<b>78</b>
5.1 INTRODUCTION .....	78
5.1.1 Motivation .....	78
5.1.2 Literature Review.....	78
<b>5.1.2.1 Wet Chemistry Overview and Selection .....</b>	<b>78</b>
<b>5.1.2.4 Hybrid .....</b>	<b>79</b>
<b>5.1.2.5 Pechini.....</b>	<b>80</b>
5.1.3 Work Plan.....	80
5.4 EXPERIMENTAL .....	81
5.4.1 Hybrid Synthesis Route.....	81
5.4.2 Pechini Sol Synthesis Route .....	82
5.4.3 XRD.....	83
5.4.4 TGA-DTA .....	83
5.5 RESULTS AND DISCUSSION .....	83
5.5.1 Creation of Sol.....	83
5.5.2 Gelation and Drying.....	84
5.5.3 Pyrolysis.....	85
5.5.4 Crystallization Behavior.....	87
5.6 CONCLUSION.....	91
<b>6 PEROVSKITE OXYNITRIDE FILM FORMATION.....</b>	<b>92</b>
6.1 INTRODUCTION .....	92
6.1.1 Motivation .....	92
6.1.2 Literature Review.....	92
6.1.3 Work Plan.....	94
6.2 EXPERIMENTAL .....	94
6.2.1 Thin film deposition.....	94
6.2.2 Ammonolysis Reaction .....	95
6.2.3 XRD.....	95
6.2.4 ESEM-EDS.....	96
6.2.5 WDS.....	96
6.2.6 XPS.....	97
6.3 RESULTS.....	98
6.3.1 Phase Composition and Structure (C1).....	98
<b>6.3.1.1 XRD Analysis .....</b>	<b>98</b>
<b>6.3.1.2 XPS Analysis .....</b>	<b>100</b>

6.3.2 Anion Composition (C2).....	102
<b>6.3.2.1 WDS Analysis</b> .....	102
<b>6.3.2.2 XPS Analysis</b> .....	105
6.3.3 Phase Homogeneity (C3).....	107
<b>6.3.3.1 EDS Analysis</b> .....	107
<b>6.3.3.2 XPS Analysis</b> .....	108
6.3.4 Valence State (C4).....	110
<b>6.3.4.1 XPS Analysis</b> .....	110
6.3.5 Microstructure (C5).....	117
<b>6.3.5.1 SEM Analysis</b> .....	117
4.0 Conclusion.....	119
4.1 Optimized Reaction Conditions.....	119
4.2 Mechansim for producing a SrTaO <sub>x</sub> N <sub>y</sub> phase.....	120
<b>REFERENCES .....</b>	<b>122</b>

# LIST OF TABLES

	<b>Page</b>
<b>Table I.</b> Electrical Response of Various Oxynitrides <sup>1</sup> .....	4
<b>Table II.</b> Synthesis Variables .....	18
<b>Table III.</b> Tolerance Factor ( $t$ ) and Ionic Radii ( $r_{\text{eff}}$ ) in $\text{ATaO}_2\text{N}$ ( $A=\text{Ca},\text{Sr},\text{Ba}$ ) Compounds. C.N. is the Coordination Number for the Obtained .....	33
<b>Table IV.</b> Potential Mechanisms for Reaction with Excess $\text{CaCO}_3$ .....	37
<b>Table V.</b> Resultant Change in Anion Chemistry for M1-M4 as a Function of Increasing Excess $\text{CaCO}_3$ .....	37
<b>Table VI.</b> Various Sintering Tactics Identified in Literature (* - Investigated in this Study) .....	56
<b>Table VII.</b> Assessment Criteria for Dowselecting the Final Wet Chemistry Route .....	81
<b>Table VIII.</b> Processing Conditions Investigated During $\text{SrTaO}_2\text{N}$ Film Production .....	95
<b>Table IX.</b> EDS, Compositional Results on Reduced Areas of the S. 2-1 Film .....	107
<b>Table X.</b> EDS, Compositional Results on Reduced Areas of the S. 6-5 Film .....	108

## LIST OF FIGURES

	<b>Page</b>
<b>Figure 2.2.1a</b>	Configuration for separating NH <sub>3</sub> , N <sub>2</sub> and H <sub>2</sub> at the furnace outtake (Wilmad-Labglass). ..... 9
<b>Figure 2.3.1a:</b>	Furnace configuration to minimize heating of gas prior to reaction zone. ....10
<b>Figure 2.3.1b:</b>	Temperature profile of furnace at a setpoint of 1000°C.....11
<b>Figure 2.3.2a</b>	Estimation of available ammonia as a function of time at temperature (or flow velocity) at 3 different temperatures. ....12
<b>Figure 2.3.3a</b>	Estimation of available ammonia at 1000°C as a function of distance from gas inlet at 3 different NH <sub>3</sub> flow velocities. ....14
<b>Figure 2.3.3b</b>	Gas penetration into sample powder bed depth.....14
<b>Figure 2.3.3c:</b>	“Dead Zones” after a change in the circumference of the gas carrier. ....15
<b>Figure 3.2.1a:</b>	Synthesis furnace setup. Measurements correspond to sample center.....19
<b>Figure 3.3.1a</b>	BaTaO <sub>2</sub> N cell volume as a function of distance from gas inlet (1000°C, 20hrs, 2.5cm/min NH <sub>3</sub> flow) .....22
<b>Figure 3.3.1b</b>	Minor phase concentration as a function of distance from gas inlet (1000°C, 20hrs, 2.5cm/min NH <sub>3</sub> flow). ....22
<b>Figure 3.3.1c</b>	BaTaO <sub>2</sub> N cell volume as a function of distance from gas inlet without samples at the first 3 locations.....24
<b>Figure 3.3.1d</b>	Minor phase concentration as a function of distance from gas inlet without samples at the first 3 locations.....24
<b>Figure 3.3.2a</b>	BaTaO <sub>2</sub> N cell volume as as a function of distance from gas inlet at 3 different flow velocities (1000°C, 20hrs). ....26

<b>Figure 3.3.2b</b>	Ta <sub>3</sub> N <sub>5</sub> concentration as a function of distance from gas inlet at 3 different flow velocities (1000°C, 20hrs). ....27
<b>Figure 3.3.3a</b>	SrTaO <sub>2</sub> N cell volume as a function of distance from gas inlet (1000°C, 20hrs, 2.5cm/min NH <sub>3</sub> flow). ....28
<b>Figure 3.3.3b</b>	Ta <sub>3</sub> N <sub>5</sub> and Sr <sub>2</sub> Ta <sub>2</sub> O <sub>7</sub> concentrations as a function of distance from gas inlet (1000°C, 20hrs, 2.5cm/min NH <sub>3</sub> flow). ....29
<b>Figure 3.3.3c</b>	CaTaO <sub>2</sub> N cell volume as a function of distance from gas inlet (1000°C, 20hrs, 2.5cm/min NH <sub>3</sub> flow). ....29
<b>Figure 3.3.3d</b>	Ta <sub>3</sub> N <sub>5</sub> and Ca <sub>2</sub> Ta <sub>2</sub> O <sub>7</sub> concentrations as a function of distance from gas inlet (1000°C, 20hrs, 2.5cm/min NH <sub>3</sub> flow). ....30
<b>Figure 3.3.3e</b>	Linear bond schematic for describing inductive effects. ....31
<b>Figure 3.3.3.1a</b>	CaTaO <sub>2</sub> N cell volume after batching with excess calcium carbonate (1000°C, 5hrs, 2.5cm/min.....34
<b>Figure 3.3.3.1b</b>	CaTaO <sub>2</sub> N cell parameters after batching with excess calcium carbonate (1000°C, 5hrs, 2.5cm/min.....35
<b>Figure 3.3.3.1c</b>	CaTaO <sub>2</sub> N diffraction patterns after batching with excess calcium carbonate (1000°C, 5hrs, 2.5cm/min.....35
<b>Figure 3.3.3.1d</b>	Change in relative area of each XPS peak after batching with different levels of excess calcium carbonate. ....38
<b>Figure 3.3.3.1e</b>	Comparison between experimental (Exp.) rates of atomic concentration change with the theoretical (The.) ....39
<b>Figure 3.3.3.1f</b>	Comparison between experimental (Exp.) rates of atomic concentration change with the theoretical (The.) ....40
<b>Figure 3.3.3.1g</b>	Comparison between experimental (Exp.) rates of atomic concentration change with the theoretical (The.) ....40
<b>Figure 3.3.4a</b>	BaTaO <sub>2</sub> N cell volume as a function of distance from gas inlet at 2 different temperatures. (20hrs, 2.5cm/min NH <sub>3</sub> flow).....41

<b>Figure 3.3.4b</b>	Minor phase concentration as a function of distance from gas inlet. (1150°C, 20hrs, 2.5cm/min NH <sub>3</sub> flow) .....	42
<b>Figure 3.3.5a</b>	BaTaO <sub>2</sub> N cell volume and minor phase concentration as a function of flow velocity with a rotary furnace design.....	43
<b>Figure 3.3.6.1a</b>	SrTaO <sub>2</sub> N cell volume as a function of distance from gas inlet (1000°C, 20hrs, 2.5cm/min NH <sub>3</sub> flow) .....	46
<b>Figure 3.3.6.1b</b>	Sr <sub>2</sub> Ta <sub>2</sub> O <sub>7</sub> minor phase concentration as a function of distance from gas inlet (1000°C, 20hrs, 2.5cm/min NH <sub>3</sub> flow).....	46
<b>Figure 3.3.6.2a</b>	Peak profiles after synthesizing SrTaO <sub>2</sub> N in ammonia (20hrs, 0.5” sample position, 1000°C) .....	47
<b>Figure 3.3.6.2b-c</b>	Microstrain and grain size response of SrTaO <sub>2</sub> N derived from (b) a SrCO <sub>3</sub> -Ta <sub>2</sub> O <sub>5</sub> precursor (ST) and.....	48
<b>Figure 3.3.6.2d</b>	SrTaO <sub>2</sub> N diffraction peak profile after synthesizing in ammonia (20hrs and 40hrs, 1.3cm sample position, 1000°C) .....	49
<b>Figure 3.3.6.4a-b</b>	SrTaO <sub>3.5</sub> powder after reacting at 1000°C for 48hrs in air.....	50
<b>Figure 3.3.6.4c-e</b>	Different precursor chemistries reacted at 1000°C for 20hrs under an NH <sub>3</sub> flow of 2.5cm/min. ....	51
<b>Figure 4.2.8a:</b>	SPS setup.....	59
<b>Figure 4.3.1.1a:</b>	Thermogravimetric results of BaTaO <sub>2</sub> N and SrTaO <sub>2</sub> N under UHP nitrogen .....	60
<b>Figure 4.3.1.1b:</b>	Thermal treatment of “As synthesized” SrTaO <sub>2</sub> N in <i>in situ</i> , high temperature under UHP nitrogen.....	61
<b>Figure 4.3.1.1c:</b>	Diffraction results after thermogravimetric analysis of SrTaO <sub>2</sub> N powder (1300°C for 1hr under UHP nitrogen atmosphere). ....	62
<b>Figure 4.3.1.1d:</b>	SrTaO <sub>2</sub> N diffraction patterns of thermally treated (1300°C for 1hr under UHP nitrogen atmosphere). ....	62
<b>Figure 4.3.1.1e:</b>	Diffraction results of BaTaO <sub>2</sub> N powder after thermogravimetric analysis (*)=Ta <sub>4</sub> N <sub>5</sub> minor phase .....	63

<b>Figure 4.3.1.2a:</b>	XRD of SrTaO <sub>2</sub> N powder as a function of temperature under a nitrogen atmosphere (oxygen content ~15ppm). ....64
<b>Figure 4.3.1.2b:</b>	Cell volume of SrTaO <sub>2</sub> N powder as a function of temperature under a nitrogen atmosphere (oxygen content ~15ppm).....64
<b>Figure 4.3.2.1a:</b>	Mass loss and shrinkage of BaTaO <sub>2</sub> N powder as a function of temperature under a 4% H <sub>2</sub> -balance N <sub>2</sub> atmosphere.....66
<b>Figure 4.3.2.1b:</b>	XRD of SrTaO <sub>2</sub> N pellet after sintering at 1275°C in nitrogen. ....66
<b>Figure 4.3.2.1c-d:</b>	XPS spectra of N <sub>1s</sub> environment before (left) and after (right) sintering a SrTaO <sub>2</sub> N pellet at 1275°C for 5hrs. in nitrogen. ....67
<b>Figure 4.3.2.1e:</b>	Spectra of Ta <sub>4f</sub> environment in the SrTaO <sub>2</sub> N pellet interior after sintering at 1275°C in nitrogen. ....68
<b>Figure 4.3.2.2a:</b>	Minor phases observed in SrTaO <sub>2</sub> N after 1400°C heat treatments for 1hr and 0.2MPa pressure. ....70
<b>Figure 4.3.2.2b:</b>	Minor phases observed in SrTaO <sub>2</sub> N after 1400°C heat treatments at 1hr and 10MPa pressure.....70
<b>Figure 4.3.2.2c:</b>	Minor impurity phases of SrTaO <sub>2</sub> N at various pressure and 1500°C for 1hr. (STO= Sr <sub>1.407</sub> Ta <sub>0.563</sub> O <sub>2.73</sub> and TaC=Tantalum carbide). ..71
<b>Figure 4.3.2.2d:</b>	Observed minor phases in SrTaO <sub>2</sub> N at various temperatures and nitrogen pressures for 1hr heat treatments. ....72
<b>Figure 4.3.2.2e:</b>	Density of SrTaO <sub>2</sub> N powder compacts after various sintering treatments under ~102 atmospheres nitrogen.....72
<b>Figure 4.3.2.3a</b>	Densification characteristics of spark plasma sintered BaTaO <sub>2</sub> N. 73
<b>Figure 4.3.2.3b</b>	Densification characteristics of spark plasma sintered SrTaO <sub>2</sub> N. 73
<b>Figure 4.3.2.3c:</b>	Diffraction data of spark plasma sintered BaTaO <sub>2</sub> N by SPS. ....74
<b>Figure 4.3.2.3d:</b>	Diffraction data of spark plasma sintered SrTaO <sub>2</sub> N by SPS. ....75
<b>Figure 4.3.2.3e:</b>	Visual appearance of spark plasma sintered BaTaO <sub>2</sub> N and SrTaO <sub>2</sub> N pellets. ....75

<b>Figure 4.3.2.3f</b>	Nitrogen content of spark plasma sintered BaTaO <sub>2</sub> N derived from LECO hot-gas extraction analysis. ....76
<b>Figure 4.3.2.3g</b>	Microstructure of spark plasma sintered BaTaO <sub>2</sub> N. ....76
<b>Figure 5.4.1a:</b>	Procedures for creating carboxylate and β-diketonate sols (left) as well as alkanolamine sols (right). ....82
<b>Figure 5.4.2a:</b>	Procedure for creating strontium-tantalum citrate sol.....83
<b>Figure 5.5.2a:</b>	Creation of non-stoichiometric oxides in the Pechini precursor after 1000°C air crystallization .....85
<b>Figure 5.5.3a</b>	Pyrolysis behavior of the carboxylate and β-diketone precursors in air. ....86
<b>Figure 5.5.3b</b>	Pyrolysis behavior of the alkanolamine precursors in air. ....87
<b>Figure 5.5.3c</b>	Pyrolysis behavior of the Pechini precursor in air. ....87
<b>Figure 5.5.4a:</b>	Crystallization behavior of the acetate precursor in air at various temperatures for 1hr. ....88
<b>Figure 5.5.4b:</b>	Crystallization behavior of the Pechini precursor in air at various temperatures for 1hr. ....88
<b>Figure 5.5.4c:</b>	Crystallization products of the alkanolamine precursor in air after 800°C for 1hr. ....89
<b>Figure 5.5.4c:</b>	Overlay of standard SrO and SrCO <sub>3</sub> on the experimental Sr <sub>0.7</sub> TaO <sub>3</sub> diffraction pattern (800°C, 1hr, air). ....90
<b>Figure 5.5.4c:</b>	Comparison of Ta <sub>4f</sub> spectra in Sr <sub>0.7</sub> TaO <sub>3</sub> (800°C, 1hr, air) and SrTaO <sub>3.5</sub> (1000°C, 48hr, air).....91
<b>Figure 6.2.5a</b>	WDS calibration curve correlating relative nitrogen peak area (N/Ta) to nitrogen content. ....97
<b>Figure 6.3.1.1a</b>	Diffraction patterns of oxynitride films on an alumina substrate (S) after synthesis under different reaction conditions .....99

<b>Figure 6.3.1.1</b>	SrTaO <sub>2</sub> N cell volume of films as a function of flow velocity (950°C, 5hrs.) (b) & reaction time (c).....	100
<b>Figure 6.3.1.2a</b>	Comparison of the N <sub>15s</sub> peak location between a SrTaO <sub>2</sub> N powder, SrTaO <sub>2</sub> N films and Ta <sub>3</sub> N <sub>5</sub> powder.....	101
<b>Figure 6.3.1.2b</b>	Deconvolution of the O <sub>1s</sub> chemical environment. ....	102
<b>Figure 6.3.2.1a-b</b>	Nitrogen content (x) in SrTaO <sub>y</sub> N <sub>x</sub> films obtained via WDS as a function of (a) flow velocity (950°C-5hrs) .....	103
<b>Figure 6.3.2.1c</b>	Cell volume as a function of WDS-derived nitrogen content for SrTaO <sub>x</sub> N <sub>y</sub> films.....	104
<b>Figure 6.3.2.2a</b>	The relative O <sub>1s</sub> /Ta <sub>4f</sub> peak area as a function of reaction time at different flow velocities .....	106
<b>Figure 6.3.3.2a</b>	XPS sputtering profile of the S.18-5 film (3keV Ar <sup>+</sup> , 1x1mm, 0.3min per cycle) & (950°C, 5hrs, 18cm/min). ....	109
<b>Figure 6.3.3.2b</b>	XPS sputtering profile of the S.1-20 film (3keV Ar <sup>+</sup> , 1x1mm, 0.3min per cycle) & (950°C, 20hrs, 1cm/min). ....	109
<b>Figure 6.3.4.1a</b>	Deconvolution of the Sr <sub>3d</sub> environment. ....	111
<b>Figure 6.3.4.1b</b>	Concentration of each Sr <sub>3d</sub> state as a function of XPS-derived nitrogen content. ....	111
<b>Figure 6.3.4.1c</b>	Ta <sub>4f</sub> environment as a function of nitrogen content and flow conditions. ....	112
<b>Figure 6.3.4.1d-g</b>	Deconvolution of the Ta <sub>4f</sub> environment for films with various nitrogen content .....	113
<b>Figure 6.3.4.1h</b>	Concentration of each Ta <sub>4f</sub> state as a function of XPS-derived nitrogen content. ....	114
<b>Figure 6.3.4.1i</b>	Deconvolution of the Ta <sub>4f</sub> environment for a solid-state synthesized SrTaO <sub>2</sub> N powder.....	115
<b>Figure 6.3.4.1j</b>	Binding energy for each Ta <sub>4f</sub> <sup>7/2</sup> state as a function of XPS-derived nitrogen content. ....	115

<b>Figure 6.3.4.1k</b>	Deconvolution of the $Ta_{4f}$ environment of a S. 18-5 film with a new, lower BE state (950°C, 5hrs, 18cm/min). .....116
<b>Figure 6.3.5.1a-b</b>	Secondary images of SrTaO <sub>2</sub> N films at varying flow velocity (950°C, 5hrs).....118

## ABSTRACT

In the field of materials, there is continuous search for new compounds with enhanced performance for a variety of applications. Historically, perovskite oxides have been of particular interest, due to the ease of compositional-property manipulation and availability of inexpensive manufacturing processes. A new class of ceramic materials with a perovskite crystal structure has been synthesized by substituting nitrogen for oxygen in the anion lattice, e.g.  $A^{+2}B^{+5}O_2N$  ( $A=Ca, Sr, Ba$  and  $B = Nb, Ta$ ),  $A^{+3}B^{+5}ON_2$  ( $A=Ln$  and  $B = Ta, Nb$ ) and  $A^{+3}B^{+4}O_2N$  ( $A=Ln$  and  $B = Ti, Zr$ ).

Of interest in present work are applications as capacitors and lead-free piezoelectrics. Kim et al. characterized permittivity, dielectric loss and conductivity of  $ATaO_2N$  ( $A=Ca, Sr, Ba$ ) and  $BaNbO_2N$  powder compacts (~45% porosity).<sup>1</sup> Results indicated high permittivity for  $BaTaO_2N$  ( $\kappa \sim 4870$ ) and  $SrTaO_2N$  ( $\kappa \sim 2870$ ) that was relatively constant over a range of temperature (273K to 373K) and frequency (0.1 kHz to 1MHz).

The origin of the high permittivity is not fully understood, since both compounds possess non-polar crystal symmetries and therefore, cannot exhibit permanent nonzero dipole moments. Various hypotheses have been proposed. Kim et al. contend that anion disorder varies the local structure thus inducing  $Ta^{+5}$  displacements and dipoles. Alternatively, formation of internal barrier layers was considered, but Kim et al. reason that the impedance results do not support this model. In contrast, Marchand et al. report that the dielectric response of a  $BaTaO_2N$  polycrystalline pellet, deduced from infrared reflection spectra, is not high.<sup>2</sup> The contradicting results merit further study and a

property-material relationship as undetermined. In addition, dielectric loss was high (~0.2) and material had insufficient density (~55%) for use in application.

Dense, low defect concentration oxynitride ceramic are essential for electrical property measurements. However, to control purity, while creating dense ceramic, requires an understanding of oxynitride synthesis and stability. Therefore, current work created a fundamental knowledge base for synthesizing oxynitride compounds that allowed large-batch production of phase-pure oxynitride powders. Unfortunately, investigations into sintering oxynitride powders identified material instabilities at high temperatures causing difficulties in forming dense ceramic. This led to development of a liquid precursor process for fabricating thin-film oxynitrides. Results indicate an insulating and dense thin-film that allowed a true characterization of electrical properties.

# 1 MOTIVATION

Compared to oxygen, nitrogen has higher electronegativity, providing a greater covalent bonding nature. Electronically, this shifts the band gap of oxynitride perovskites to lower energies compared to oxides and creates adsorption in the visible regime, providing possible utility as non-toxic dye pigments and photocatalysts.<sup>3,4</sup> Previous work also shows promise for oxynitrides as capacitors and lead-free piezoelectrics.<sup>1,5,6</sup>

Kim et al. characterized permittivity, dielectric loss and conductivity of oxynitride powder compacts (~45% porosity).<sup>1</sup> (**Table I**) Results indicated high permittivity for BaTaO<sub>2</sub>N and SrTaO<sub>2</sub>N that was relatively constant over a range of temperature (273K to 373K) and frequency (0.1 kHz to 100kHz).

**Table I.** Electrical Response of Various Oxynitrides<sup>1</sup>

Compound	Calculated Grain Permittivity	Dielectric Loss (@1MHz)	Calculated Grain Conductivity (S/cm)
BaNbO <sub>2</sub> N	-	-	~10 <sup>-1</sup> S/cm
BaTaO <sub>2</sub> N	4870	0.2	1.1x10 <sup>-5</sup> S/cm
SrTaO <sub>2</sub> N	2870	0.2	1.8x10 <sup>-5</sup> S/cm
CaTaO <sub>2</sub> N	30	-	~10 <sup>-8</sup> S/cm

Cohen et al. first described use of perovskite oxynitrides as lead-free piezoelectrics for the A<sup>+3</sup>B<sup>+4</sup>O<sub>2</sub>N systems.<sup>6</sup> Employing 1<sup>st</sup>-principle DFT calculations, Cohen et al. systematically searched all combinations of A<sup>+3</sup> and B<sup>+4</sup> elements, optimizing structural stability, resistivity and polarization response. Results pointed to

YSiO<sub>2</sub>N and YGeO<sub>2</sub>N as the best candidates. Although no synthetic route to octahedral Si<sup>4+</sup> or Ge<sup>4+</sup> seemed feasible, use of oxynitrides in ferroelectric and lead-free piezoelectric applications is still an intriguing pursuit. Comparison of experimental and theoretical results would provide valuable mechanistic and scientific insight. In addition, there is need for investigation into the large, untapped compositional space (A<sup>+2</sup>B<sup>+5</sup>O<sub>2</sub>N, A<sup>+3</sup>B<sup>+5</sup>O<sub>2</sub>N, etc.) not investigated in the computational study.

The goal of the current work is to improve processing for the promising new class of oxynitrides to provide low defect, dense ceramic. This will allow establishment of an electrical property-structure relationship. Furthermore, newly obtained knowledge on oxynitride processing can lead to use in other applications to aid in further developments.

## 2 NITRIDING WITH AMMONIA

### 2.1 INTRODUCTION

#### 2.1.1 Motivation

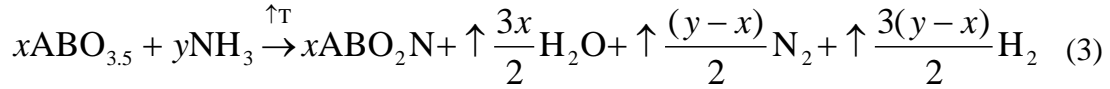
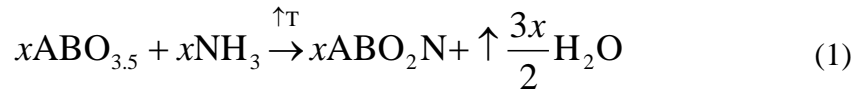
Before a true property-structure relationship can be established, the powder material needs to be well processed and defect-free. This requires an in-depth understanding of synthesis. The present literature does not provide the requisite understanding. Therefore, the scope of this chapter is to provide a systematic investigation of variables affecting synthesis reaction rate and purity. Chapter 3 will then apply this knowledge to the synthesis of oxynitride powders.

#### 2.1.2 Literature Review

Ammonolysis is a widely used tactic for synthesizing perovskite oxynitrides.<sup>7</sup> Conventional processing involves placing homogeneously mixed precursors with the intended stoichiometric ratio into a stream of gaseous ammonia at elevated temperatures, which then acts as a nitriding and reducing agent. Variations invoke use of a flux to enhance nitridation kinetics or pre-reacting precursors to form a multicomponent oxide (such as  $ABO_{3.5}$ ), thus preventing formation of impurity phases (such as binary nitrides).<sup>8,9</sup>

The formation of an oxynitride,  $ABO_2N$ , from an oxide,  $ABO_{3.5}$ , via high temperature ammonolysis is described in equation 1. As  $NH_3$  dissociates, hydrogen passes rapidly into a molecular state and nitrogen forms an “active” species.<sup>10</sup> Hydrogen then removes oxygen as water vapor, allowing active nitrogen to be incorporated into the lattice. The form of active nitrogen is currently not known, but is assumed to reside in an atomic state.<sup>10</sup>

Equation 1 assumes a perfectly efficient reaction and is not achievable under normal synthesis conditions, because of the competing reaction shown in equation 2. Here, as  $\text{NH}_3$  dissociates, nitrogen forms the molecular gas.<sup>10</sup> Once nitrogen forms the molecular gas,  $\text{N}_2$ , the activity becomes negligible at typical ammonolysis synthesis temperatures (800°C-1200°C), limiting the efficiency of equation 1 and the oxynitride reaction.<sup>11</sup> This is a direct result of the high dissociation enthalpy of  $\text{N}_2$  ( $\Delta H_{\text{diss}} = 995\text{kJ/mol @ } 1300\text{K}$ ).<sup>12</sup> Hence, equation 3 illustrates the combination of equations 1 and 2 and the experimentally-observed oxynitride reaction.



Ideally, the reaction proceeds without production of  $\text{N}_2$  and excess  $\text{H}_2$  (eqn 1). Experimentally this is not the case, since  $\text{NH}_3$  dissociation occurs from many experimental factors. Below ~550°C, ammonia dissociation to form active nitrogen is limited unless a surface capable of catalyzing the reaction exists.<sup>10,13</sup> Synthesis in the present work is assumed to have little catalytic response and relies on the use of high temperature processing to provide active species. In addition, oxynitride synthesis from an oxide involves other high temperature reactions: oxide reduction, transport of atomic nitrogen and molecular water as well as solid-state diffusion.

Unfortunately, as temperature increases, the formation rate of inert, molecular nitrogen increases (increase in efficiency of eqn 2).<sup>7</sup> Therefore, oxynitride production is only realized through non-equilibrium conditions and proper control of the gas phase composition. Consequently, this forces a constant replenishing of ammonia and active nitrogen, through either recirculation or regulation of gas flow. Other experimental factors controlling ammonia activity, besides temperature and flow conditions, are sample position, temperature distribution and furnace design.<sup>11</sup>

### **2.1.3 Work Plan**

Synthesis of oxynitride material requires control over gas phase composition. Hence, this study investigated  $\text{NH}_3$  concentration (at the furnace outtake) and  $\text{NH}_3$  dissociation rate (to  $\text{N}_2$  and  $\text{H}_2$ ) as a function of the reaction conditions: temperature ( $900^\circ\text{C}$ - $1100^\circ\text{C}$ ), flow velocity (2-125cm/min), sample placement (1.3-19.0cm), temperature distribution and furnace configuration. Gas control is the key to desirable reaction rate and purity of  $\text{ATaO}_2\text{N}$  (A=Ca,Sr,Ba) powders and  $\text{SrTaO}_2\text{N}$  films as discussed in Chapters 3 and 6, respectively.

## **2.2 EXPERIMENTAL**

### **2.2.1 Ammonia Concentration Measurement**

Ammonia,  $\text{H}_2$  and  $\text{N}_2$  were separated by utilizing differences in water solubility, where  $\text{NH}_3$  has a much higher solubility than  $\text{N}_2$  and  $\text{H}_2$ . This is a commonly employed tactic for analyzing chemical composition of effluent gas in ammonia nitriding of stainless steels.<sup>14</sup> The measurement setup was obtained from Wilmad-Labglass and is shown in **Figure 2.2.1a**.

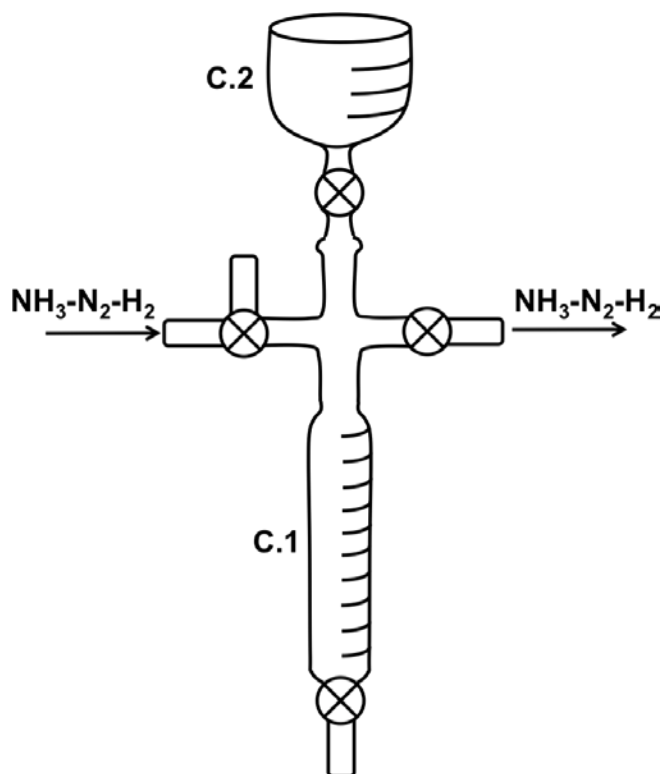


**Figure 2.2.1a** Configuration for separating  $\text{NH}_3$ ,  $\text{N}_2$  and  $\text{H}_2$  at the furnace outtake (Wilmad-Labglass).

The procedure begins with isolating a known quantity of effluent gas (100ml) in gas chamber **C.1**. Next, a water reservoir, **C.2**, (>100ml) located above the gas chamber is opened. Ammonia will rapidly dissolve in water, where  $\text{H}_2$  and  $\text{N}_2$  will not. Pressure equilibration at  $\sim 1\text{atm}$ , between water above the chamber and the chamber constituents (gas/water mixture), traps a known quantity of gas and water in the chamber. The volume of gas in **C.1** is the dissociated  $\text{NH}_3$  present as stoichiometric  $\text{H}_2$  and  $\text{N}_2$ . The volume of trapped water in **C.1** corresponds to volume of non-dissociated  $\text{NH}_3$ . The procedure was repeated for multiple flow rates (10ml/min-2,500ml/min) at various temperatures ( $800^\circ\text{C}$ - $1000^\circ\text{C}$ ). Temperature of the effluent gas never exceeded  $\sim 25^\circ\text{C}$ .

## 2.3 RESULTS AND DISCUSSION

### 2.3.1 Temperature Distribution

It is important to limit exposure of  $\text{NH}_3$  to elevated temperatures prior to the reaction zone, to minimize premature dissociation to  $\text{N}_2$  and  $\text{H}_2$ . **Figure 2.3.1a** shows the furnace configuration and **Figure 2.3.1b** shows that the temperature upstream or downstream of the reaction zone was limited through use of high temperature alumina refractory (with drilled holes for gas flow) and alumina fiber at positions 0 and 20cm.

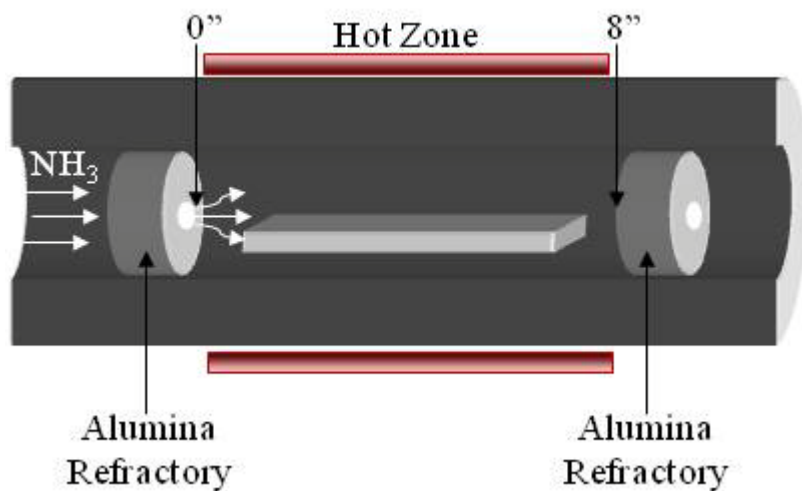


**Figure 2.3.1a:** Furnace configuration to minimize heating of gas prior to reaction zone.

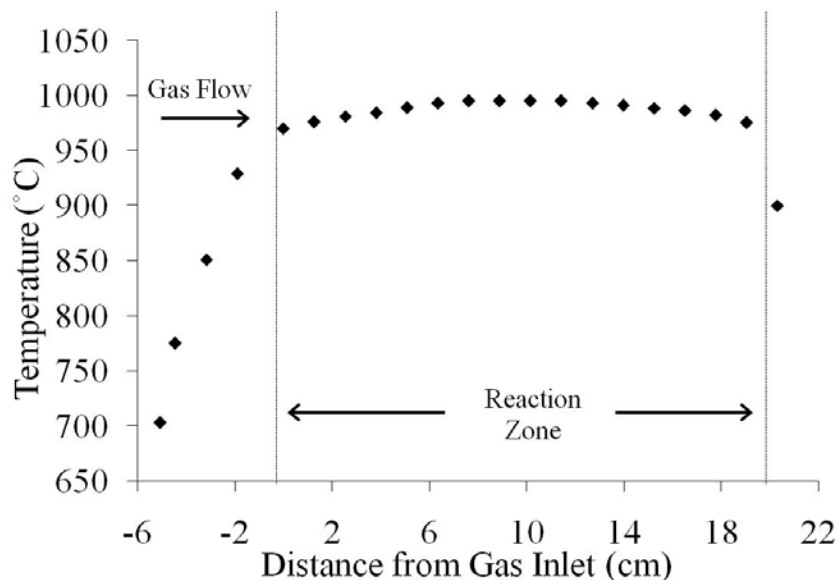


**Figure 2.3.1b:** Temperature profile of furnace at a setpoint of 1000°C.

### 2.3.2 Maximum Temperature and Flow Velocity

NH<sub>3</sub> concentration (at the furnace outlet) was measured as a function of flow rate at three different temperatures. Each flow rate of NH<sub>3</sub> was then corrected for volumetric expansion upon dissociation, from 1 to 2 moles (assuming isobaric conditions). Finally, through using the defined reaction zone area and hot zone length (shown in figure 2.3.1a), each flow rate was converted to a time during which the gas experienced the reaction temperature. By evaluating the NH<sub>3</sub> concentration (at the outlet) as a function of time at processing temperature, a dissociation rate can be extracted. **(Figure 2.3.2a)**

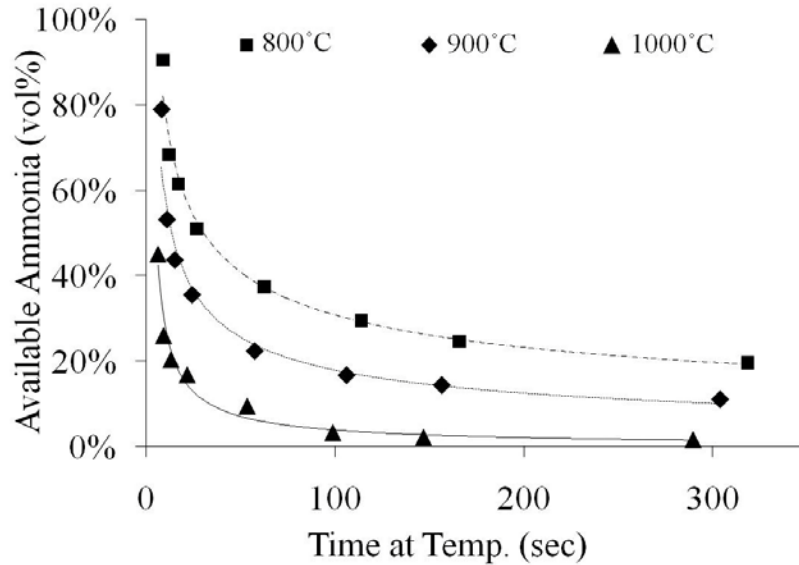


**Figure 2.3.2a** Estimation of available ammonia as a function of time at temperature (or flow velocity) at 3 different temperatures.

Results indicate that greater temperatures enhance the  $\text{NH}_3$  dissociation rate. Prolonged times at temperature (or lower flow velocities) further increase dissociation to  $\text{N}_2$  and  $\text{H}_2$ . In addition, the dissociation rate shows exponential decay. Exponential functions occur when decay or growth rate is proportional to the current function value. As  $\text{NH}_3$  dissociates, the next discrete step (of time) starts at a new, lower initial concentration than the previous, changing the boundary conditions and making the decay rate dependent upon the pre-existing concentration value.

### 2.3.3 Sample Placement and Furnace Configuration

Ideally, the decay rate relationship (in figure 2.3.2a) can model  $\text{NH}_3$  concentration as a function of distance from the inlet at a defined flow velocity. (**Figure 2.3.3a**) Experimentally these values should be taken with caution, since the model is based on many simplifying assumptions (see below). However, results do indicate the importance of sample placement, since  $\text{NH}_3$  concentration decreases as gas progresses further from

the inlet. In addition, evaluation of assumptions (A1-A2) provides important insight for optimizing furnace design.

The degree of gas intermixing perpendicular to flow is uncertain (A1). **(Figure 2.3.3b)** If intermixing is low, this may cause depletion of reactive gas ( $\text{NH}_3$ ) at the sample-gas interface as well as limited gas penetration into the powder bed. Rotary calcining furnaces are a common practice to minimize this potential problem and are investigated in section 3.3.5. Gas flow requires a certain time (or distance) to establish a stable flow after a change in circumference of the gas carrier vessel, which is observed in these experiments (A2). Flow instability produces “dead zones” within the reaction zone. **(Figure 2.3.3c)** The current furnace design uses alumina refractory with drilled holes directly upstream of the reaction zone. (refer to Figure 2.3.1a) Therefore, samples were positioned in-line with the alumina refractory inlet hole, eliminating sample placement in possible “dead zones.”

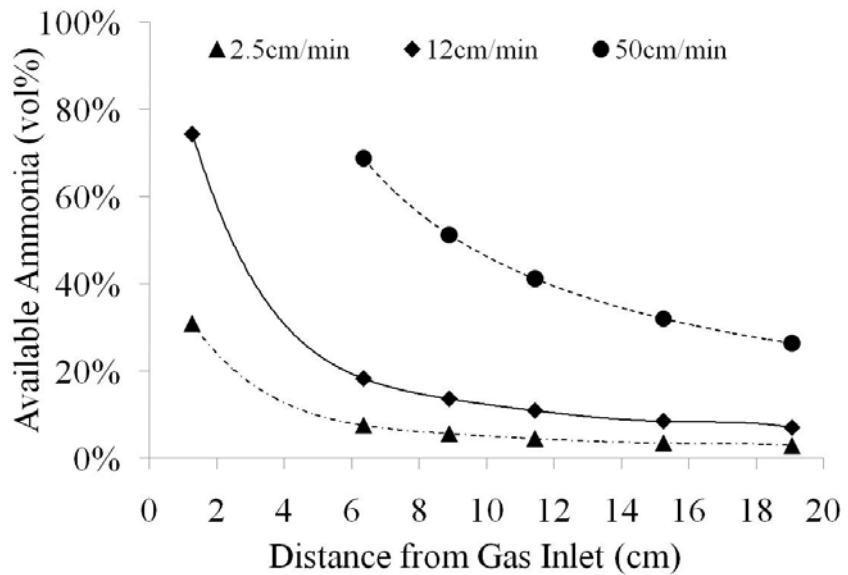


**Figure 2.3.3a** Estimation of available ammonia at 1000C as a function of distance from gas inlet at 3 different NH<sub>3</sub> flow velocities.

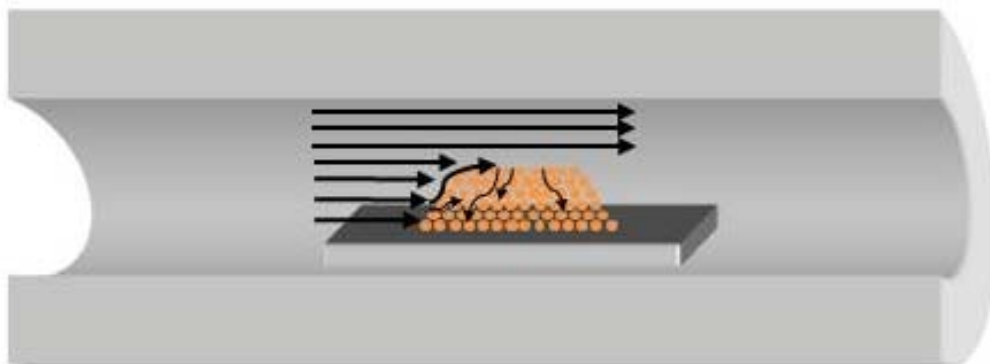


**Figure 2.3.3b** Gas penetration into sample powder bed depth.

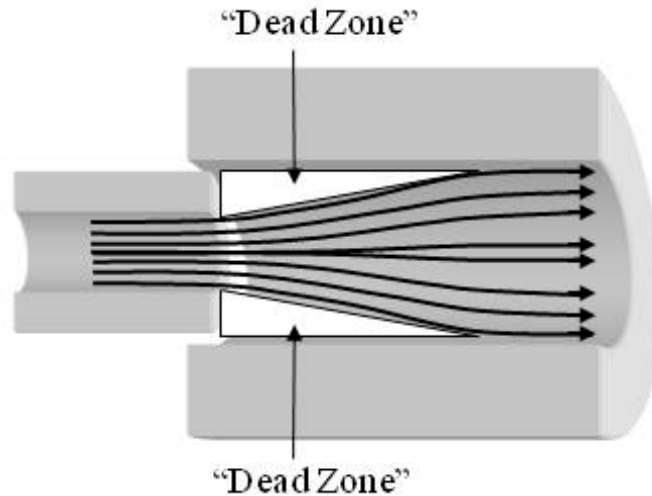


**Figure 2.3.3c:** “Dead Zones” after a change in the circumference of the gas carrier.

## 2.4 CONCLUSION

Temperature exposure of  $\text{NH}_3$  prior to the reaction zone can enhance premature decomposition to  $\text{N}_2\text{-H}_2$ .  $\text{NH}_3$  concentration decreases as a function of distance from the gas inlet. An increase in flow velocity increases  $\text{NH}_3$  concentration and provides greater quantities of  $\text{NH}_3$  at greater distances from the gas inlet. Higher temperature enhances  $\text{NH}_3$  decomposition (to  $\text{N}_2\text{-H}_2$ ) and reduces  $\text{NH}_3$  availability at greater distances from the gas inlet. Furnace configuration should be optimized to provide adequate sample-atmosphere interaction and limit sample placement in “dead zones.” These properties of  $\text{NH}_3$  decomposition will be used to control concentration of active nitriding species and subsequently, reaction rate and purity of oxynitride powders.

## 3 SOLID STATE POWDER SYNTHESIS

### 3.1 INTRODUCTION

#### 3.1.1 Motivation

Chapter 2 correlated processing conditions to gas phase composition. This newly obtained knowledge can be applied to control reaction rate and purity of BaTaO<sub>2</sub>N powder with subsequent extension to other systems, SrTaO<sub>2</sub>N and CaTaO<sub>2</sub>N, to investigate formation ability as a function of A-site cation.

#### 3.1.2 Literature

Literature has identified some important compositional trends when synthesizing perovskite oxynitrides. Marchand et al. produced phase pure BaTaO<sub>2</sub>N and BaNbO<sub>2</sub>N from mixtures of barium carbonate and the binary oxide (Ta<sub>2</sub>O<sub>5</sub> or Nb<sub>2</sub>O<sub>5</sub>).<sup>5</sup> Use of multicomponent oxides (ABO<sub>3.5</sub> A=Sr,Ca and B=Nb,Ta) during ammonolysis eliminated formation of binary (oxy)nitride phases in SrTaO<sub>2</sub>N, SrNbO<sub>2</sub>N and CaTaO<sub>2</sub>N compounds.<sup>8,15</sup> Similar processing was ineffective at producing phase-pure CaNbO<sub>2</sub>N. Rachel et al. and Kim et al. both reported inability to form CaNbO<sub>2</sub>N above 750°C because of irreversible NbO<sub>x</sub>N<sub>y</sub> production.<sup>1,16</sup> Use of flux additions lowered the synthesis temperature to <750°C, allowing production of CaNbO<sub>2</sub>N. Since Rachel et al. used an atomically-mixed multicomponent oxide, it would seem that processing issues, such as inhomogeneities, could be eliminated as a cause for NbO<sub>x</sub>N<sub>y</sub> production in CaNbO<sub>2</sub>N. An alternative explanation is through a lower perovskite structural stability arising from the smaller, less electropositive Ca<sup>2+</sup> cation.

Stable ternary oxynitrides typically consist of highly electropositive elements.<sup>17</sup> Conversely, elements with intermediate electronegativity resulted in either partial

reductions (W,Mo,V,Cr) or formation of metallic constituents (Cd,In,Sb,Pb,Bi). Therefore, electronegativity has significant importance in obtaining stable, oxynitrides. Many other contributions to stability can be envisioned: ionic size, ionic charge, electric field strength of the ion, valence electron configuration, stability of competing phases, etc. Current work discusses electric field strength of the ion, electronegativity and ionic size, since these factors change as a function of A-site cation (Ca,Sr,Ba).

Interestingly, synthesis from multicomponent oxides yielded phase-pure SrTaO<sub>2</sub>N, CaTaO<sub>2</sub>N and SrNbO<sub>2</sub>N compared to synthesis from a carbonate/oxide mixture. One rationale is that the multicomponent oxide provided additional lattice energy stabilization. For example, phase segregation (e.g. formation of Ta<sub>3</sub>N<sub>5</sub>) in a multicomponent oxide has to overcome many more high-energy barriers (bond breaking/rearrangement, solid-state diffusion) in comparison to a binary mixture. The added stabilization energy could promote phase-pure synthesis, whereas, for the niobium counterpart with higher electronegativity (CaNbO<sub>2</sub>N), the added lattice energy was not enough to prevent a binary oxynitride from forming.

### 3.1.3 Work Plan

Ammonolysis variables were systematically changed to control reaction rate and purity of BaTaO<sub>2</sub>N powders. (**Table II**) This is accomplished through quantifying the perovskite cell volume and minor phases present via XRD structural refinements. Work then investigated other systems, SrTaO<sub>2</sub>N and CaTaO<sub>2</sub>N, and compared to BaTaO<sub>2</sub>N results. ATaO<sub>2</sub>N (A=Ba,Sr,Ca) compounds were chosen with regard to literature results on synthesis capability, stability and preliminary electrical characterization.<sup>1,17-19</sup>

Additionally, SrTaO<sub>2</sub>N precursor chemistries are evaluated as means for tailoring reaction rate, structure, composition and/or microstructure.

**Table II.** Synthesis Variables

<b>Compound</b>	<i>Sample Position</i>	<i>Flow Velocity</i>	<i>Temperature</i>	<i>Furnace Configuration</i>	<i>Precursor Form</i>
BaTaO <sub>2</sub> N	sec. 3.3.1	sec. 3.3.2	sec. 3.3.4	sec. 3.3.5	
SrTaO <sub>2</sub> N	sec. 3.3.3				sec. 3.3.6
CaTaO <sub>2</sub> N	sec. 3.3.3				

## 3.2 EXPERIMENTAL

### 3.2.1 Precursor Formation

Oxynitride samples were prepared via ammonolysis. A stoichiometric mixture (with respect to the cations) of ACO<sub>3</sub> and Ta<sub>2</sub>O<sub>5</sub> (A=Ba,Sr,Ca) was ball milled in IPA and subsequently dried at 75°C. Six, 0.5 gram samples of the mixture were evenly spread on flat alumina plates in 2.5cm x 2.5 cm squares and placed in the furnace at discrete intervals. **(Figure 3.2.1a)** To maintain an even temperature throughout the reaction zone, alumina insulation board and fiber refractory were located at the reaction zone ends (0 and 20cm).

Precursor chemistry was altered by forming a multicomponent oxide, ATaO<sub>3.5</sub> (A = Ba,Sr,Ca), or adding flux to the ACO<sub>3</sub>/Ta<sub>2</sub>O<sub>5</sub> mixture. The multicomponent oxide, SrTaO<sub>3.5</sub>, was synthesized by reaction of the corresponding SrCO<sub>3</sub> and Ta<sub>2</sub>O<sub>5</sub> mixture in air at 1000°C for 48hrs with an intermittent grinding at 24hrs. The flux composition was a 1:1 cation stoichiometric mixture of SrCl<sub>2</sub> and KCl corresponding to the eutectic

melting point.  $\text{SrCl}_2$  was used to limit flux incorporation. The mixture was then added in excess of 4 times by weight to the  $\text{SrCO}_3$  and  $\text{Ta}_2\text{O}_5$  mixture and ball milled overnight.

### 3.2.2 Ammonolysis Reaction

The reaction vessel was purged and heated at  $^\circ\text{C}/\text{min}$  to the target temperature ( $1000^\circ\text{C}$  or  $1150^\circ\text{C}$ ) for 20 hours under varying flow velocities (2.0cm/min, 12cm/min & 50cm/min) of anhydrous ammonia. The samples were then cooled at  $^\circ\text{C}/\text{min}$  to  $400^\circ\text{C}$ , where the ammonia was switched to nitrogen gas, and then cooled to room temperature.

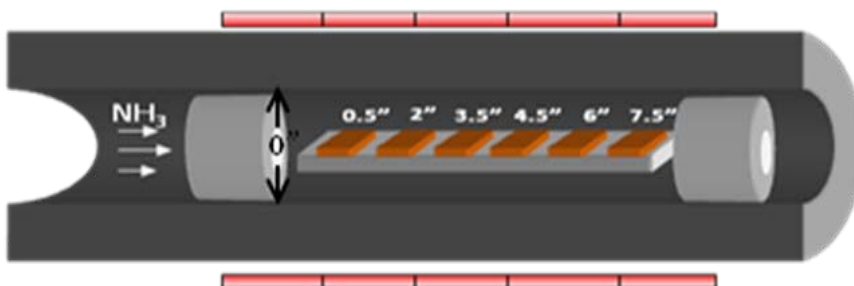


**Figure 3.2.1a:** Synthesis furnace setup. Measurements correspond to sample center.

### 3.2.3 Powder X-Ray Diffraction

Samples were run on a D5000 Siemens Diffractometer with a  $\text{Cu}_{\text{K}\alpha}$  radiation source set at 40keV and 30mA. Data was collected over the angular range of  $20^\circ < 2\theta < 140^\circ$  incrementing at  $0.03^\circ$  with count times of 10 seconds per step. Lattice parameters and concentrations were acquired through structural refinements using TOPAS software. Error bars are included, but are smaller than the data symbols.

### 3.2.4 Chemical Composition Analysis

LECO hot-gas extraction was used to determine anion composition. Equipment was calibrated with NIST and LECO standards and  $\text{Si}_3\text{N}_4$ . Samples were inductively

heated in a graphite-nickel crucible to  $>2800^{\circ}\text{C}$  under a helium atmosphere. Evolved oxygen (in the form of  $\text{CO}_2$ ) was quantified and removed using IR and a LECO-patented adsorbent. Evolved nitrogen (in the form of  $\text{N}_2$ ) was quantified through thermal conductivity.

### **3.2.5 X-Ray Photoelectron Spectroscopy (XPS)**

XPS was performed with a PHI Quantera SXM Spectrometer using a monochromated  $\text{Al}_{\text{K}\alpha}$  radiation source (1486.6eV) operating at 15 watts. The sample area investigated was  $0.01\text{mm}^2$ . High-resolution spectra were collected with a 26eV pass energy at an incident angle of  $45^{\circ}$  relative to the sample surface. Charging effects were minimized through the use of an energy electron gun set at 1V and  $20\mu\text{A}$ . The step size was 0.05eV and signal to noise ratio was 6:1. The binding energy was calibrated using the  $\text{C}_{1s}$  peak associated to an adsorbed carbon surface layer at 284.6eV. For the fitting procedure, FWHM values and peak area ratios of spin orbitals were obtained from literature, the NIST database or experimentally derived using  $\text{Sr}_2\text{Ta}_2\text{O}_7$ ,  $\text{Ta}_2\text{O}_5$ ,  $\text{Ta}_3\text{N}_5$  powders.<sup>20-22</sup> Peak position and peak intensity were allowed to vary.

### **3.2.6 Environmental Scanning Electron Microscopy (ESEM)**

Microstructures were imaged with a Quanta 200F (Field Emission) Environmental SEM/EDAX Genesis system at a 20kv accelerating potential. The system was operated in low vacuum mode at a water base pressure of 0.6 Torr.

## 3.3 RESULTS AND DISCUSSION

### 3.3.1 Sample Position

Positioning samples closer to the gas inlet provides exposure to higher  $\text{NH}_3$  concentrations (refer to section 2.3.3). The effect on oxynitride reaction rate and phase purity is investigated by nitriding  $\text{BaCO}_3\text{-Ta}_2\text{O}_5$  powder mixtures at different distances from the gas inlet (refer to figure 2.3.1a). **Figures 3.3.1a and 3.3.1b** show the resulting cell volume and minor phase concentrations, respectively, of synthesized  $\text{BaTaO}_2\text{N}$  as a function of distance from the gas inlet. The ammonolysis heat treatment was  $1000^\circ\text{C}$  for 20hrs at a  $2.5\text{cm/min}$   $\text{NH}_3$  flow. Samples positioned at 1.3cm, 5.0cm, and 9.0cm have similar cell volumes and no observable oxide minor phases. As distance from the gas inlet increases beyond 9.0cm, cell volume and oxide minor phase concentration (mixture of  $\text{Ba}_3\text{Ta}_5\text{O}_{15}$  and  $\text{Ba}_5\text{Ta}_4\text{O}_{15}$ ) progressively decrease and increase, respectively.  $\text{Ta}_3\text{N}_5$  concentrations were low ( $<1.5\text{wt } \%$ ) and relatively constant.

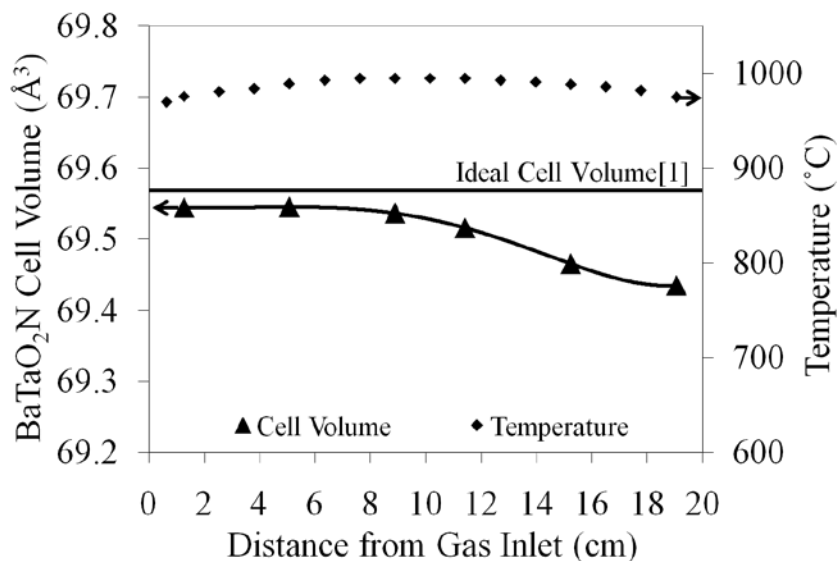


**Figure 3.3.1a** BaTaO<sub>2</sub>N cell volume as a function of distance from gas inlet (1000°C, 20hrs, 2.5cm/min NH<sub>3</sub> flow) Measurement location corresponds to distance measured from gas inlet to center of sample. Ideal cell volume obtained from literature.<sup>8</sup>

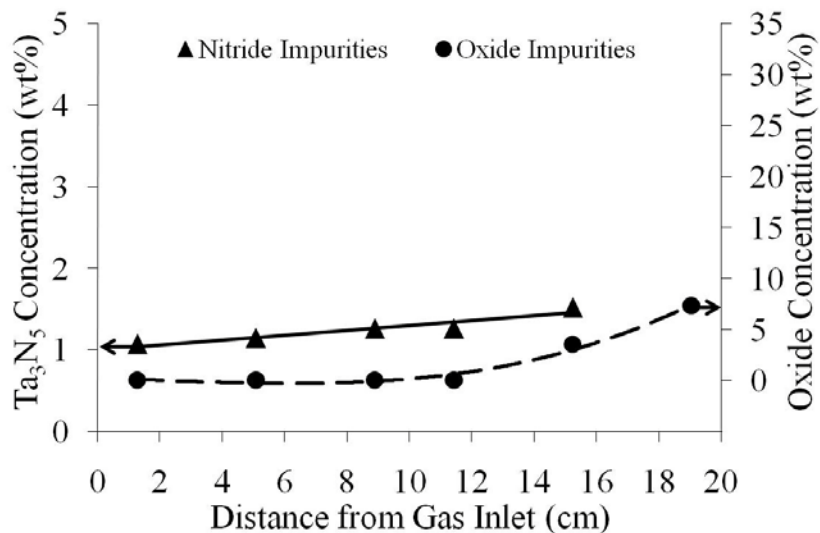


**Figure 3.3.1b** Minor phase concentration as a function of distance from gas inlet (1000°C, 20hrs, 2.5cm/min NH<sub>3</sub> flow). Measurement location corresponds to distance measured from gas inlet to center of sample. Oxide minor phases are a mixture of Ba<sub>3</sub>Ta<sub>5</sub>O<sub>15</sub> and Ba<sub>5</sub>Ta<sub>4</sub>O<sub>15</sub>.

Oxide minor phases (refer to figure 3.3.1b) in the downstream samples (15.0cm & 19.0cm) are attributed to incomplete oxynitride formation. Decreased oxynitride production as a function of distance from the gas intake can result from:

- 1.) Thermal decomposition of  $\text{NH}_3$  and formation of  $\text{N}_2$  (refer to section 2.3.3), lowering the concentration of active nitrogen
- 2.) Depletion of  $\text{NH}_3$  concentration from upstream sample reactions
- 3.) Increased water partial pressure from upstream samples

The slower reaction rate for the downstream samples was investigated by repeating the experiment (slight change in flow velocity was noted, from 2.5cm/min to 2.0cm/min) with samples at positions 1.3cm, 5.0cm, and 9.0cm removed, leaving only the three downstream samples. (**Figures 3.3.1c & d**) Both experiments had matching cell volumes and a similar oxide minor phase trend, highlighting the importance of suppressing premature  $\text{NH}_3$  decomposition via furnace design, flow velocity and sample placement.

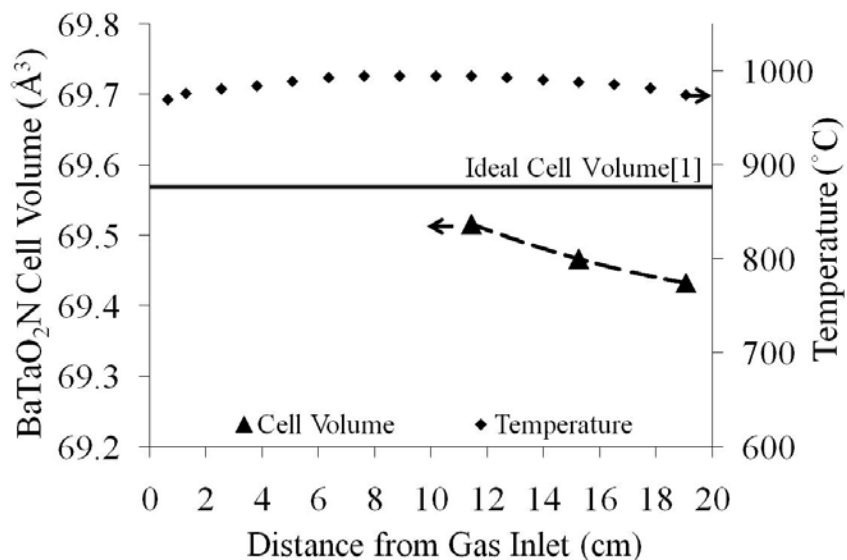


**Figure 3.3.1c** BaTaO<sub>2</sub>N cell volume as a function of distance from gas inlet without samples at the first 3 locations (1000°C for 20hrs, 2.0cm/min NH<sub>3</sub> flow). Measurement location corresponds to distance measured from gas inlet to center of sample. Ideal cell volume obtained from literature.<sup>8</sup>

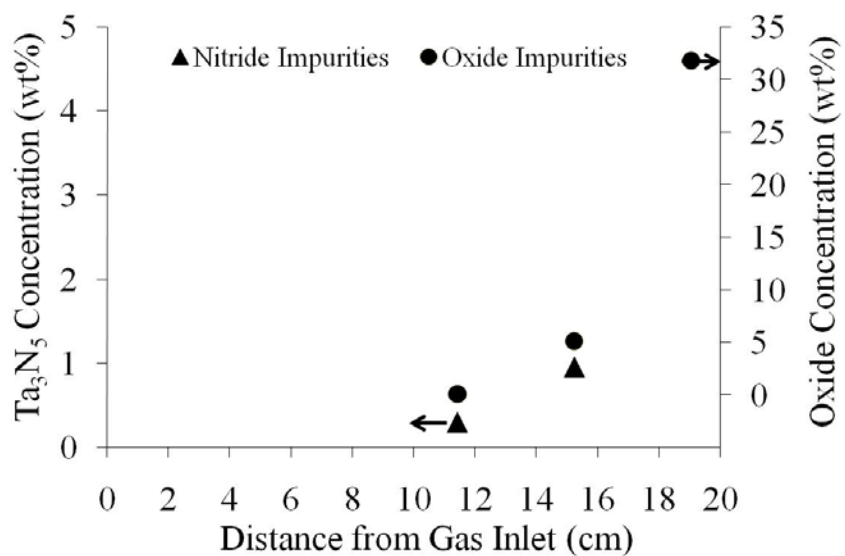


**Figure 3.3.1d** Minor phase concentration as a function of distance from gas inlet without samples at the first 3 locations (1000°C, 20hrs, 2.0cm/min NH<sub>3</sub> flow). Measurement location corresponds to distance measured from gas inlet to center of sample. Oxide minor phases are a mixture of Ba<sub>3</sub>Ta<sub>5</sub>O<sub>15</sub> and Ba<sub>5</sub>Ta<sub>4</sub>O<sub>15</sub>.

It is plausible the BaTaO<sub>2</sub>N cell volume reduction at position  $\geq 11.5$  cm (refer to figures 3.3.1a & d) suggests an incomplete nitrogen exchange in the perovskite structure. This is consistent with the discussion presented by Kim et al.<sup>1</sup> Kim et al. compared the SrNbO<sub>3</sub> and SrNbO<sub>2</sub>N perovskite structures and demonstrated that the oxynitride has greater cell volume, despite the larger ionic radius of Nb<sup>+4</sup> compared to Nb<sup>+5</sup>. In addition, results are consistent with ionic size differences of the anions (IV-coordinated, ionic radii of N<sup>3-</sup> - 1.46Å and O<sup>2-</sup> - 1.38Å).<sup>23</sup> IV-coordinated radii were used, since literature does not have a VI-coordinated ionic radius for N<sup>3-</sup>.

Production of Ta<sub>3</sub>N<sub>5</sub> (refer to figure 3.3.1b) can be understood as competition between solid-state diffusion and nitridation processes. As ammonolysis proceeds, Ta<sub>2</sub>O<sub>5</sub> undergoes nitridation. If sufficient solid-state transport does not occur to stabilize mixed anion octahedra, full nitridation to binary components will take place.

Oxygen and nitrogen contents were measured through LECO, hot-gas extraction. Samples in positions 1.3cm through 9.0cm were combined and sent for analysis, since larger batch sizes are required. LECO, hot-gas extraction analysis revealed that the relatively XRD phase pure oxynitride is nitrogen deficient, (BaTa)<sub>1.053</sub>O<sub>2.163</sub>N<sub>0.784</sub>.

### 3.3.2 Flow velocity

Increasing flow velocity provides greater NH<sub>3</sub> concentrations per interval of time or distance (refer to section 2.3.2) and increases the rate of removal of gaseous byproducts. Two higher velocities, 12cm/min and 50cm/min, were investigated and compared to the previous 2.5cm/min samples (refer to sec. 3.3.1). (**Figures 3.3.2a & b**) As flow velocity increased from 2.5cm/min to 12cm/min, all sample positions had an increase in cell volume (compared to 2.5cm/min samples) and no observable oxide

phases. Further increase to 50cm/min enhanced  $Ta_3N_5$  production at the first three incoming positions with corresponding perovskite cell volume increases.

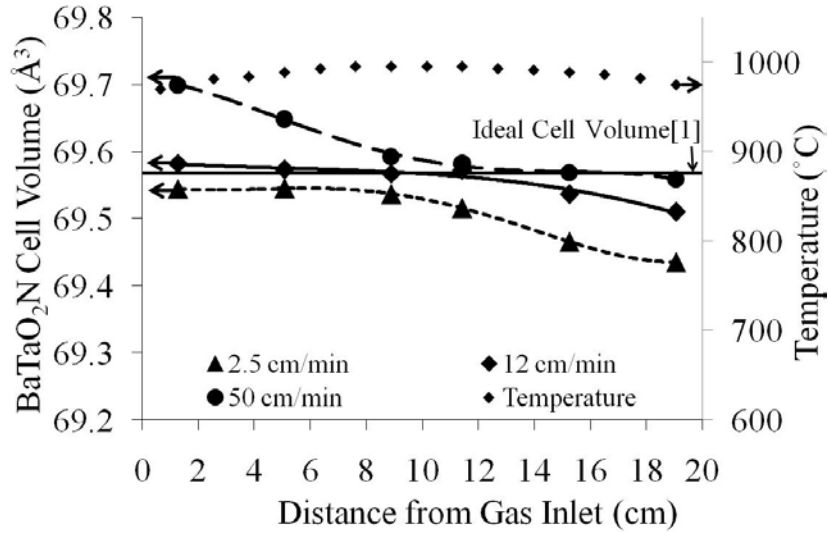


**Figure 3.3.2a** BaTaO<sub>2</sub>N cell volume as a function of distance from gas inlet at 3 different flow velocities (1000°C, 20hrs). Measurement location corresponds to distance measured from gas inlet to center of sample. Ideal cell volume obtained from literature.<sup>8</sup>

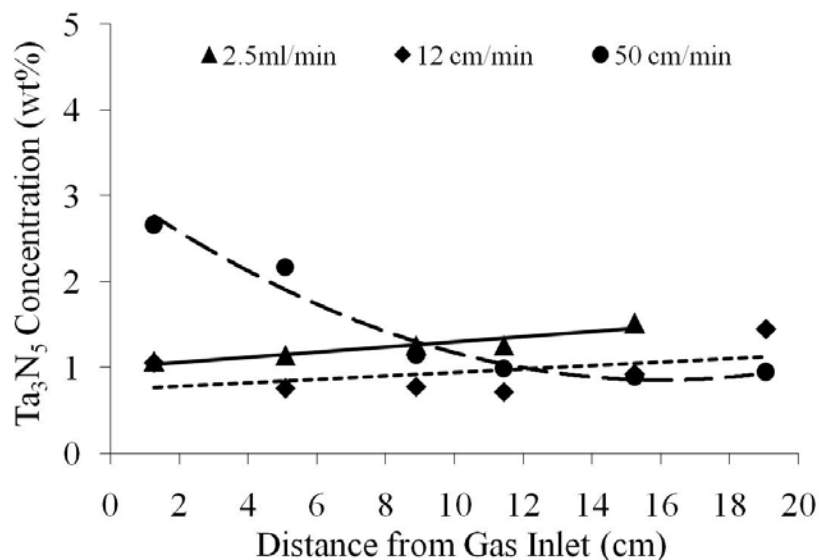


**Figure 3.3.2b**  $Ta_3N_5$  concentration as a function of distance from gas inlet at 3 different flow velocities (1000°C, 20hrs). Measurement location corresponds to distance measured from gas inlet to center of sample.

At high flow velocity (50cm/min), the  $NH_3$  and  $Ta_3N_5$  concentrations as a function of distance from the gas inlet correlate (refer to sec. 2.3.3). At the highest  $NH_3$  concentration (sample located at 1.3cm), the  $Ta_3N_5$  concentration was greatest. As  $NH_3$  concentration diminished (distance from gas intake became greater),  $Ta_3N_5$  production progressively decreased. A high  $NH_3$  concentration enhances the nitride reaction, limiting the available time for solid-state diffusion. Results indicate the upper limit on flow velocity is controlled by production of  $Ta_3N_5$  minor phases and lower limit by reaction rate. Lattice expansion at high flow velocities could result from B-site vacancies. Similar results have been noted for  $BaTiO_3$ , where titanium vacancies enlarged the lattice from anion repulsion.

### 3.3.3 A-Site Exchange

Formation ability as a function of A-site cation was investigated through ammonolysis of  $SrCO_3-Ta_2O_5$  and  $CaCO_3-Ta_2O_5$  powder mixtures. Reaction conditions

were 1000°C, 20hrs, 2.5cm/min NH<sub>3</sub> flow. At positions less than 11.5cm, SrTaO<sub>2</sub>N showed consistent unit cell volumes, minor amounts of Ta<sub>3</sub>N<sub>5</sub> (<0.5wt%) and no observable oxide phases. (Figures 3.3.3a & b) Beyond 11.5cm, results trended similarly to BaTaO<sub>2</sub>N synthesis (refer to sec. 3.3.1). Cell volume decreased and oxide minor phases increased as distance from the gas intake became greater. The CaTaO<sub>2</sub>N samples had similar cell volumes at all positions, excessive Ta<sub>3</sub>N<sub>5</sub> formation (4-8wt%) and no observable oxide phases. (Figures 3.3.3c & 3.3.3d) To account for the structural distortion from a cubic symmetry (SrTaO<sub>2</sub>N-tetragonal and CaTaO<sub>2</sub>N-orthorhombic) cell volumes consistent of 4 unit cells.

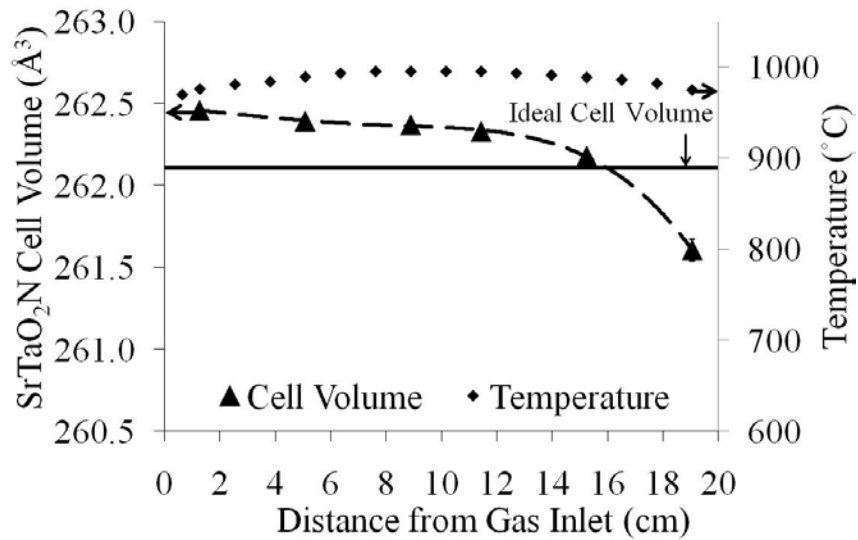


**Figure 3.3.3a** SrTaO<sub>2</sub>N cell volume as a function of distance from gas inlet (1000°C, 20hrs, 2.5cm/min NH<sub>3</sub> flow). Measurement location corresponds to distance measured from gas inlet to center of sample. Ideal cell volume obtained from literature.<sup>15</sup>

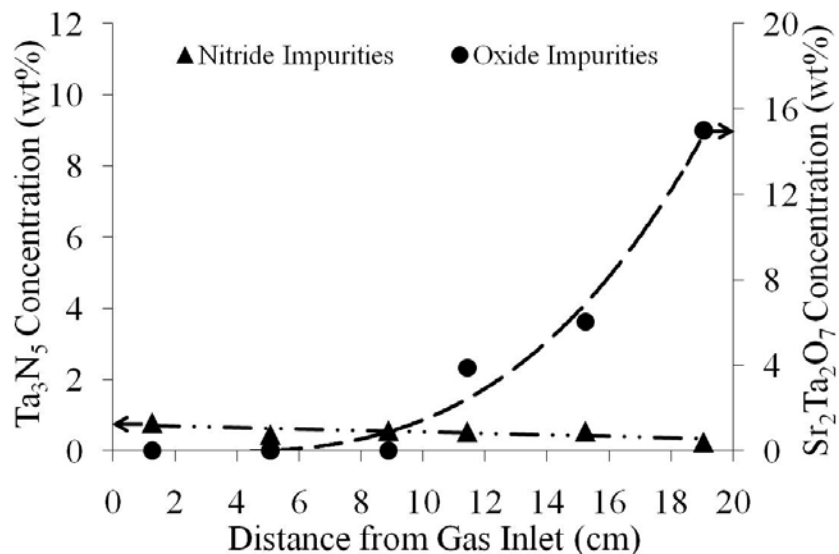


**Figure 3.3.3b** Ta<sub>3</sub>N<sub>5</sub> and Sr<sub>2</sub>Ta<sub>2</sub>O<sub>7</sub> concentrations as a function of distance from gas inlet (1000°C, 20hrs, 2.5cm/min NH<sub>3</sub> flow). Measurement location corresponds to distance measured from gas inlet to center of sample.

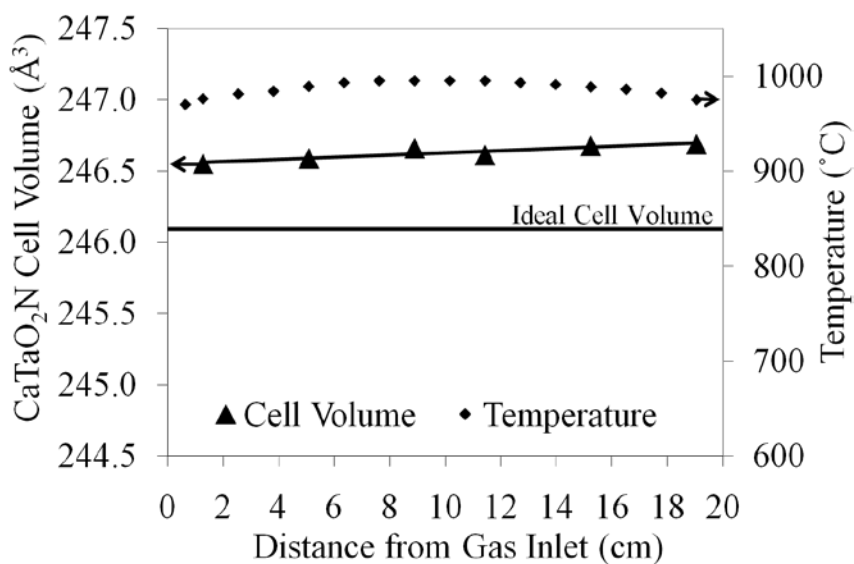


**Figure 3.3.3c** CaTaO<sub>2</sub>N cell volume as a function of distance from gas inlet (1000°C, 20hrs, 2.5cm/min NH<sub>3</sub> flow). Measurement location corresponds to distance measured from gas inlet to center of sample. Ideal cell volume obtained from literature.<sup>24</sup>

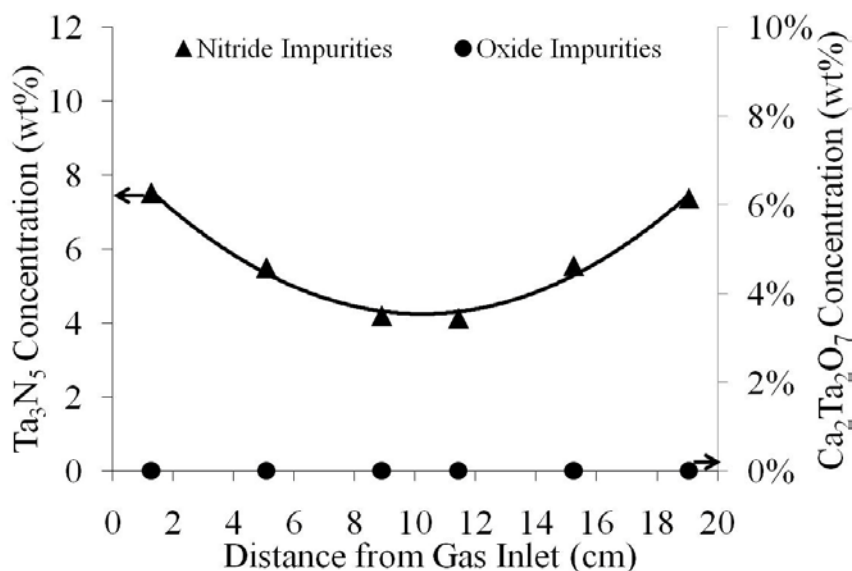


**Figure 3.3.3d** Ta<sub>3</sub>N<sub>5</sub> and Ca<sub>2</sub>Ta<sub>2</sub>O<sub>7</sub> concentrations as a function of distance from gas inlet (1000°C, 20hrs, 2.5cm/min NH<sub>3</sub> flow). Measurement location corresponds to distance measured from gas inlet to center of sample.

For CaTaO<sub>2</sub>N there was no correlation between the Ta<sub>3</sub>N<sub>5</sub> concentration and distance from the gas intake (or NH<sub>3</sub> concentration). Whereas, the Ta<sub>3</sub>N<sub>5</sub> concentration during BaTaO<sub>2</sub>N synthesis (as a function of flow velocity) had a clear dependence upon NH<sub>3</sub> concentration (refer to sec. 3.3.1). Differing trends indicate separate mechanisms. The trending Ta<sub>3</sub>N<sub>5</sub> and NH<sub>3</sub> concentrations for BaTaO<sub>2</sub>N results imply competition between the nitride reaction and solid-state transport. An alternative explanation for the absence of a Ta<sub>3</sub>N<sub>5</sub> and NH<sub>3</sub> concentration trend for CaTaO<sub>2</sub>N arises from structural instability as the A-site cation changes from barium/strontium to calcium. Possible contributing factors to instability are the different electric field strengths, electronegativities and/or ionic sizes of the A-site ions. For example, a change in electronegativity of the A-site cation can reduce structural stability by altering the nature of the transition metal-anion bond (ionic or covalent). This is understood via “inductive effects”.<sup>25</sup>

Inductive effects are more easily described by examining a simple linear bond, where two different cations ( $T^{5+}$ =transition metal and  $A^{2+}$ =alkaline earth metal) bond through one oxygen ion. (**Figure 3.3.3e**) Donation of electron density from  $A^{2+}$  to the adjacent oxygen,  $O^{2-}$ , shifts the electron density towards  $T^{5+}$ . As  $A^{2+}$  electronegativity becomes lower, the covalent character between  $T^{5+}$  and  $O^{2-}$  increases.

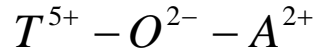


**Figure 3.3.3e** Linear bond schematic for describing inductive effects.

Stabilization of mixed anion octahedra with high oxidation states requires a high degree of covalency between  $T^{5+}$  and  $O^{2-}$  and therefore, an inductive effect from A-site cations.<sup>26 27</sup> For example, comparison of  $AFeO_{3-x}$  compounds ( $A=Ca/Sr/Ba$ ), found only trivalent iron in  $CaFeO_{2.5}$  and large portions of tetravalent iron in  $SrFeO_{3-x}$  and  $BaFeO_{3-x}$ .<sup>25</sup> Electronegative values for alkaline earth metals decrease in the order,  $Ca > Sr > Ba$ , consistent with a weaker inductive effect exerted by calcium and lower structural stability.

Additionally, decrease in the alkaline-earth oxide lattice energy (via a change in electronegativity, ionic field strength or ionic size) can also reduce stability of the mixed anion structure. For example, formation enthalpies increase in the order  $CaO < SrO < BaO$ .<sup>12,28</sup> The higher stability for CaO would lead to less stable mixed-anion systems, possibly promoting phase decomposition.

It is well known in the Ta-O-N system that yttrium, magnesium and scandium substitute for tantalum, forming solid solutions and different polymorphs.<sup>29</sup> Given the smaller ionic radius of calcium relative to strontium and barium, it seems plausible that

calcium can be partially substituted onto the B-site in a similar fashion.<sup>23</sup> (Table III) Other material systems have observed similar results, where calcium substitutes into Ba(Ca,Ti)O<sub>3</sub> with significant B-site occupancy. This would result in excess tantalum, possibly explaining the observed Ta<sub>3</sub>N<sub>5</sub> formation.

Tolerance factors (t) illustrate nonideal packing when using calcium as the A-site ion in ATaO<sub>2</sub>N oxynitrides.<sup>30</sup> (eqn 4)

$$t = \frac{(R_a + R_o)}{\sqrt{2}((R_t + R_o))} \quad (4)$$

R<sub>a</sub>, R<sub>o</sub>, and R<sub>b</sub> represent the ionic radius of the A-site cation, anion and B-site cation in the perovskite structure, ABO<sub>3</sub>. For the calculation, R<sub>o</sub> was taken as a weighted average of nitrogen and oxygen based on the assumed occupation of 4 O<sup>2-</sup> and 2 N<sup>3-</sup> per octahedron. Overall, all three factors for instability, a lower t (**Table III**), stronger binary oxide lattice energy and a weaker inductive effect, are maximized for CaTaO<sub>2</sub>N. This is consistent with the observed decomposition to binary nitrides.

At lower NH<sub>3</sub> concentrations (further away from the gas intake), faster reaction kinetics were observed during CaTaO<sub>2</sub>N synthesis, compared to ATaO<sub>2</sub>N (A=Sr,Ba) compounds (sec. 3.1). This is justified via a lack of observable oxide phases in XRD. Rachel et al. observed similar trends after nitriding A<sub>2</sub>B<sub>2</sub>O<sub>7</sub> powders.<sup>16</sup> Single-phase BaTaO<sub>2</sub>N was synthesized after 126hrs at 1000C, SrTaO<sub>2</sub>N after 90hrs at 1000C and CaTaO<sub>2</sub>N at still shorter times and lower temperatures, 36hrs at 950C. Analogous results were found for ANbO<sub>2</sub>N (A=Sr,Ba) compounds. In addition, oxynitride stability might explain the reaction rate trend. The CaTaO<sub>2</sub>N structure, which is proposed to be

less table, readily over-nitrided to Ta<sub>3</sub>N<sub>5</sub>, indicating a possible greater nitridation rate. This could correlate to shorter required nitridation times during oxynitride formation..

**Table III.** Tolerance Factor (t) and Ionic Radii (r<sub>eff</sub>) in ATaO<sub>2</sub>N (A=Ca,Sr,Ba) Compounds. C.N. is the Coordination Number for the Obtained Ionic Radii

Element	C.N.	r <sub>eff</sub> (Å)	Compound	t
Ca <sup>2+</sup>	12	1.34	CaTaO <sub>2</sub> N	0.95
Sr <sup>2+</sup>	12	1.44	SrTaO <sub>2</sub> N	0.98
Ba <sup>2+</sup>	12	1.61	BaTaO <sub>2</sub> N	1.04
Ta <sup>5+</sup>	6	0.64		
O <sup>2-</sup>	4	1.38		
N <sup>3-</sup>	4	1.46		

### 3.3.3.1 Cation Stoichiometry

XRD did not indicate a calcium-rich phase when excessive Ta<sub>3</sub>N<sub>5</sub> formed during CaTaO<sub>2</sub>N synthesis (sec. 3.3.3). Possible explanations are a:

- A. Weakly crystalline or low concentration minor phase
- B. Low scattering intensity of calcium (Z=20) compared to tantalum (Z=73)
- C. Calcium-rich ternary oxynitride

To investigate formation of a possible calcium-rich ternary oxynitride (C), excess CaCO<sub>3</sub> was batched into the precursor, (1+x)CaCO<sub>3</sub>+0.5Ta<sub>2</sub>O<sub>5</sub> (x=0.11 or 0.25), and compared to a cation stoichiometric mixture, CaCO<sub>3</sub> + 0.5Ta<sub>2</sub>O<sub>5</sub>. Samples were treated at 1000°C for 5hrs under a NH<sub>3</sub> flow of 2.5cm/min and positioned at 2.5-5.0cm from the gas inlet. Powder diffraction indicated no oxide or nitride minor phases. As the excess CaCO<sub>3</sub> increased, cell volume increased, greater XRD peak broadening was observed and

color changed from green-yellow to dull green/white, indicating a possible reduction in nitrogen content. (Figures 3.3.3.1a-c)

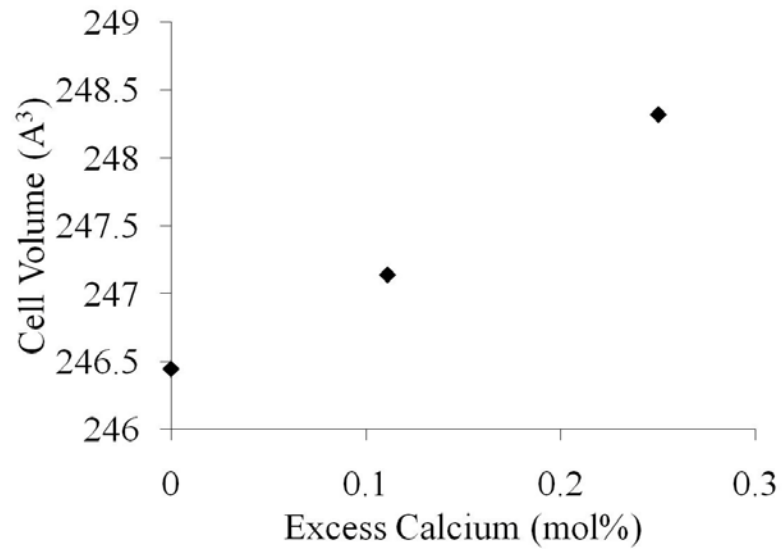


**Figure 3.3.3.1a** CaTaO<sub>2</sub>N cell volume after batching with excess calcium carbonate (1000°C, 5hrs, 2.5cm/min NH<sub>3</sub> flow, positioned at 2.5-5.0cm from gas inlet).

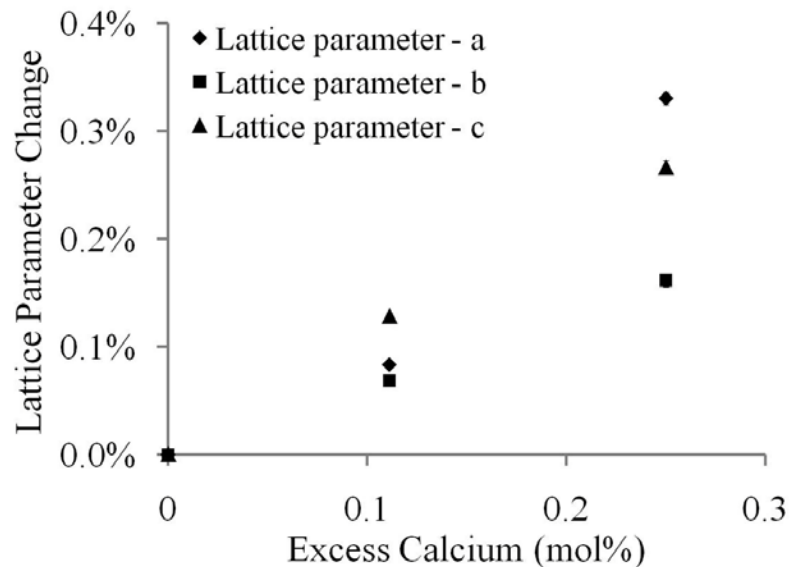


**Figure 3.3.3.1b** CaTaO<sub>2</sub>N cell parameters after batching with excess calcium carbonate (1000°C, 5hrs, 2.5cm/min NH<sub>3</sub> flow, positioned at 2.5-5.0cm from gas inlet).

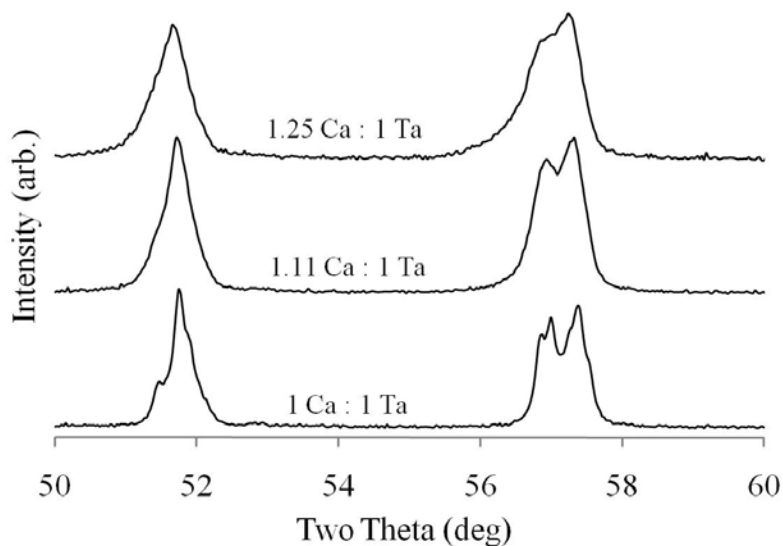


**Figure 3.3.3.1c** CaTaO<sub>2</sub>N diffraction patterns after batching with excess calcium carbonate (1000°C, 5hrs, 2.5cm/min NH<sub>3</sub> flow, positioned at 2.5-5.0cm from gas inlet).

As CaCO<sub>3</sub> excess increases, XRD shows a trend towards a cubic perovskite structure and no detectable minor phases. Consequently, results suggest incorporation of excess calcium into the perovskite. This could explain the lack of calcium-rich minor

phases during CaTaO<sub>2</sub>N synthesis (refer to sec. 3.3.3), when excessive Ta<sub>3</sub>N<sub>5</sub> formed. Currently, the structural effects associated with excess calcium are unknown. A plausible theory is site mixing, where calcium would reside on the A-site and B-site. Similar results have been observed when adding excess CaO to Ba(Ca,Ti)O<sub>3</sub> and excess SrO to Sr(Sr,Nb)O<sub>2</sub>N.<sup>31</sup> Depending upon the atomic location of calcium (such as B-site), a higher concentration could induce greater inductive effects to better stabilize the mixed anion octahedral (refer to sec. 3.3.3).

XPS was used to explore possible changes in the perovskite structure associated with excess calcium by evaluating four potential mechanisms, M1-M4. (**Table IV**) Creation of B-site vacancies was not considered, because the configuration is highly unfavorable energetically. Each electrical compensation mechanism indicates a different response in anion composition as a function of excess CaCO<sub>3</sub> (or cation stoichiometry). (**Table V**) Therefore, examining ionic concentrations (of Ca<sub>2p</sub>, N<sub>1s</sub>, O<sub>1s</sub>) as a function of CaCO<sub>3</sub> content with XPS may indicate a structural change (S1-S4). The surface and interior of the powder were investigated via Ar<sup>+</sup> sputtering (0, 3 and 5 cycles at 2keV-2x2mm) and the area of each XPS peak (Ca<sub>2p</sub>, N<sub>1s</sub>, O<sub>1s</sub>) was normalized to the Ta<sub>4f</sub> peak area.

**Table IV.** Potential Mechanisms for Reaction with Excess CaCO<sub>3</sub> (x=excess CaCO<sub>3</sub>)

M1	A two-phase system (where CaO is below the detectable threshold in XRD) $(y+x)CaCO_3 + \frac{y}{2}Ta_2O_5 + yNH_3 \rightarrow xCaO + yCaTaO_2N + (y+x)CO_2 \uparrow + \frac{3y}{2}H_2O \uparrow$
M2	Calcium on B-site (Ca <sub>Ta''</sub> ), electrically compensate with nitrogen vacancies (V <sub>N'''</sub> ) $(y+x)CaCO_3 + \frac{y}{2}Ta_2O_5 + yNH_3 \rightarrow Ca_{(y+\frac{x}{2})} \left( Ca_{\frac{x}{2}}, Ta_y \right) O_{(2y+x)} N_y + (y+x)CO_2 \uparrow + \frac{3y}{2}H_2O \uparrow$
M3	Calcium on B-site (Ca <sub>Ta''</sub> ), electrically compensate with oxygen vacancies (V <sub>O''</sub> ) $(y+x)CaCO_3 + \frac{y}{2}Ta_2O_5 + yNH_3 \rightarrow Ca_{(y+\frac{x}{2})} \left( Ca_{\frac{x}{2}}, Ta_y \right) O_{(2y+\frac{x}{2})} N_{(y+\frac{x}{2})} + (y+x)CO_2 \uparrow + \frac{3y}{2}H_2O \uparrow$
M4	Calcium on B-site (Ca <sub>Ta''</sub> ), electrically compensate with change in anion chemistry (O <sub>N'</sub> ) $(y+x)CaCO_3 + \frac{y}{2}Ta_2O_5 + yNH_3 \rightarrow Ca_{(y+\frac{x}{2})} \left( Ca_{\frac{x}{2}}, Ta_y \right) O_{(2y+\frac{5x}{2})} N_{(y-x)} + (y+x)CO_2 \uparrow + \frac{2(y-x)}{2}H_2O \uparrow$

**Table V.** Resultant Change in Anion Chemistry for M1-M4 as a Function of Increasing Excess CaCO<sub>3</sub>

M1	No change in the N/Ta ratio and an increase in the O/Ta ratio
M2	No change in the N/Ta ratio and an increase in the O/Ta ratio
M3	An increase in the N/Ta ratio and the slowest rate of increase for the O/Ta ratio
M4	A decrease in the N/Ta ratio and the greatest rate of increase for the O/Ta ratio

Batching with excess CaCO<sub>3</sub> induced greater Ca/Ta ratios, greater O/Ta ratios and lower N/Ta ratios on the powder surface and in the powder interior. This is shown through a change in the relative area of each XPS peak as a function of CaCO<sub>3</sub> content (representative example shown in figure 3.3.3.1d).

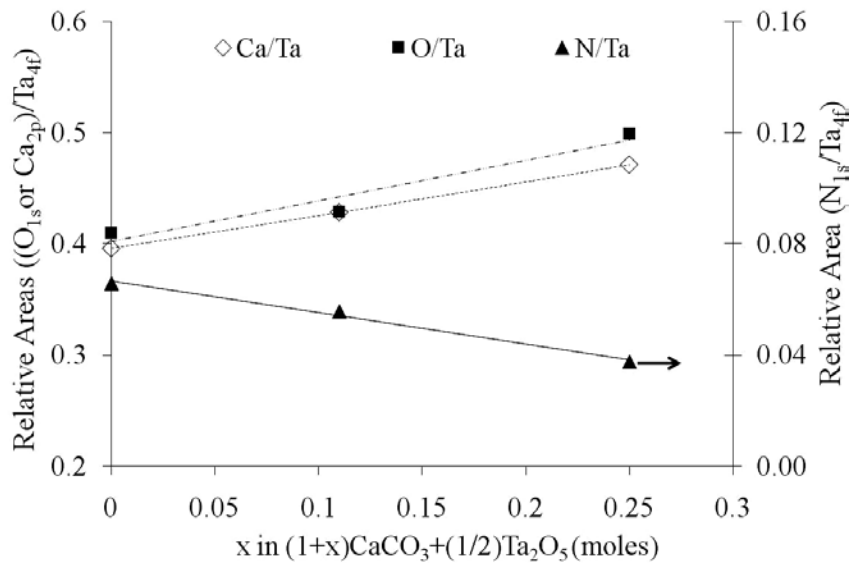


**Figure 3.3.3.1d** Change in relative area of each XPS peak after batching with different levels of excess calcium carbonate. Powder underwent 5 cycles of  $\text{Ar}^+$  sputtering to eliminate surface layer (2keV-2x2mm).

Results suggest the perovskite is modified via mechanism M4 with an increase in oxygen and decrease in nitrogen concentration. The experimental rates of atomic concentration change were then compared to the theoretical rates of change in mechanism M4 (refer to Table IV). The relative peak areas at  $x=0$  were adjusted to the ideal stoichiometry,  $\text{Ca}/\text{Ta}=1$ ,  $\text{N}/\text{Ta}=1$  and  $\text{O}/\text{Ta}=2$  ( $\text{CaTaO}_2\text{N}$ ). The change in the relative peak areas, from  $x=0$  to  $x=0.11/0.25$ , were then taken as a percentage increase or decrease from the ideal stoichiometry. (**Figures 3.3.3.1e-g**) The powder interior (after 3 and 5  $\text{Ar}^+$  sputter cycles) correlates well to predicted rates of change. However, greater deviation from theoretical was observed on the powder surface. It is possible results are complicated from surface entities.

Alternatively to mechanism M4, excess  $\text{CaCO}_3$  could inhibit the nitride reaction via creating a surface layer and gas diffusion barrier. This would provide excess oxygen

and lower nitrogen concentrations. For example, Masuda et al replaced lanthanum with strontium in the compound  $(\text{Sr}_x, \text{La}_{1-x})\text{TiO}_2\text{N}$  and observed a preferential surface segregation of strontium (via XPS).<sup>32</sup> However, current work did not show an enrichment of calcium on the surface. Furthermore, no oxide minor phases (e.g.  $\text{Ca}_2\text{Ta}_2\text{O}_7$  or  $\text{CaO}$ ) associated to an incomplete nitride reaction were observed in XRD. Additionally, the cell volume expanded with decreasing nitrogen content. Where, previous results (sec. 3.3.3) indicate an opposite trend and a reduction in cell volume with incomplete nitride reactions (lower nitrogen contents).

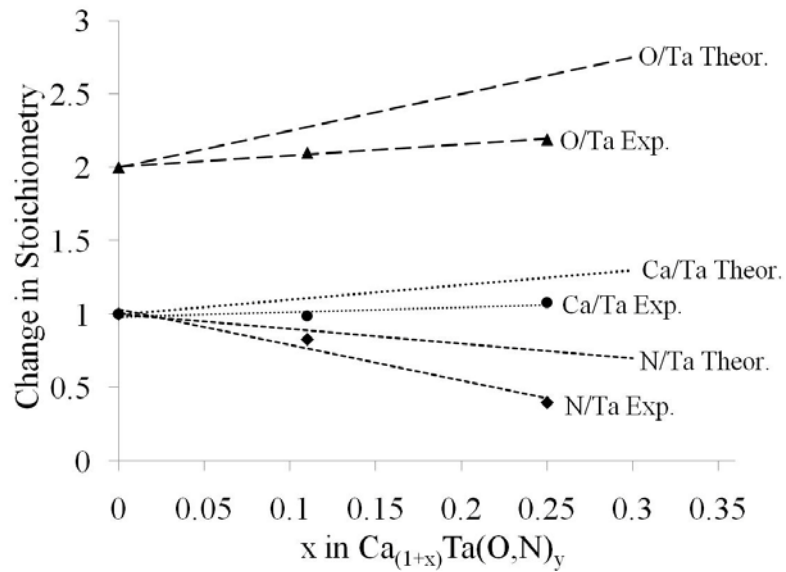


**Figure 3.3.3.1e** Comparison between experimental (Exp.) rates of atomic concentration change with the theoretical (The.) rates of change of scenario S4 at the powder surface.

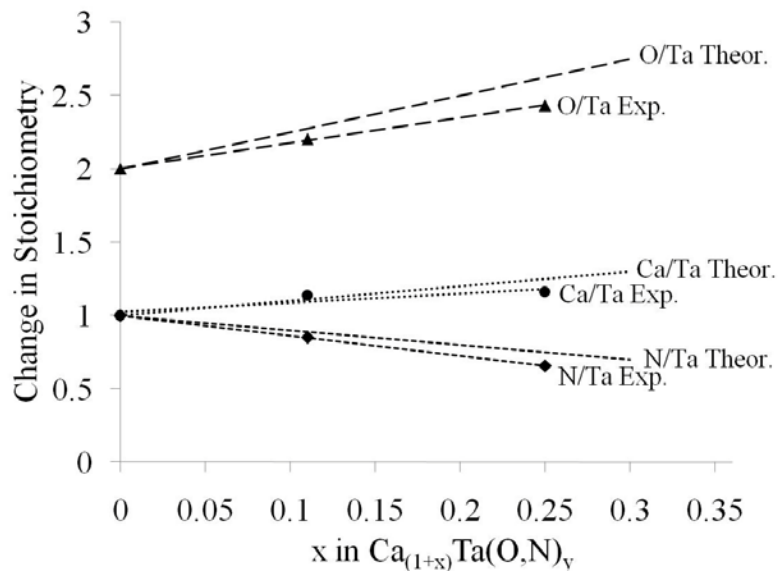


**Figure 3.3.3.1f** Comparison between experimental (Exp.) rates of atomic concentration change with the theoretical (The.) rates of change of scenario S4 after 3 Ar<sup>+</sup> sputtering cycles.

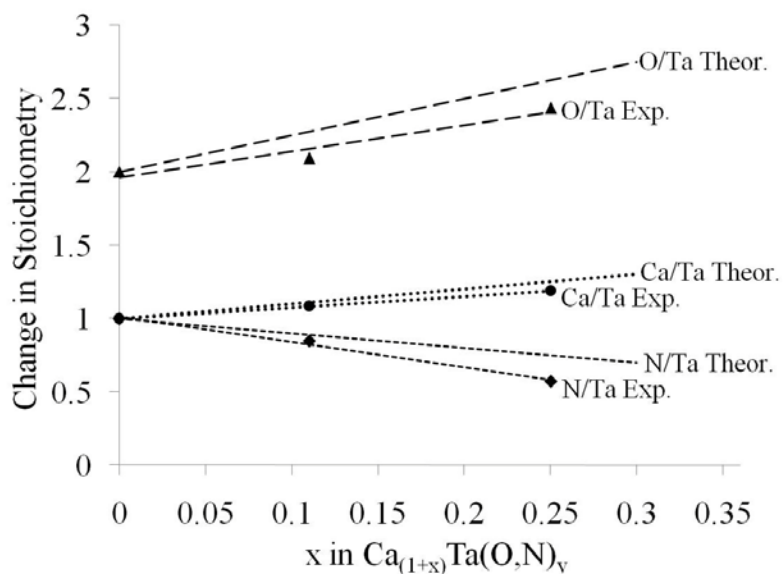


**Figure 3.3.3.1g** Comparison between experimental (Exp.) rates of atomic concentration change with the theoretical (The.) rates of change of scenario S4 after 5 Ar<sup>+</sup> sputtering cycles.

### 3.3.4 Temperature

An increase in temperature decreases  $\text{NH}_3$  availability at downstream positions (refer to section 2.3.2) and enhances solid-state transport. To investigate the effect on oxynitride synthesis, the experiment in section 3.3.1 was repeated at a higher temperature ( $1150^\circ\text{C}$ ). The different positions of the  $\text{BaTaO}_2\text{N}$  samples had similar cell volumes with oxide phases apparent by the second incoming position (5.0cm). (Figures 3.3.4a & b) The sample at position 19.0cm had minimal oxynitride conversion, therefore is not shown. At the first three incoming positions, samples had noticeable powder consolidation and a blackish hue, indicating a possible tantalum reduction.

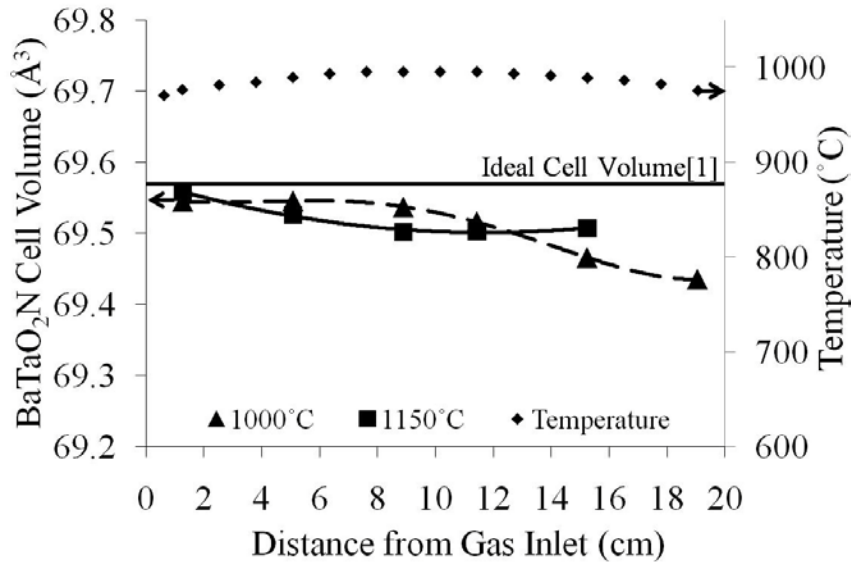


**Figure 3.3.4a**  $\text{BaTaO}_2\text{N}$  cell volume as a function of distance from gas inlet at 2 different temperatures. (20hrs, 2.5cm/min  $\text{NH}_3$  flow) Measurement location corresponds to distance measured from gas inlet to center of sample. Ideal cell volume obtained from literature.<sup>8</sup>

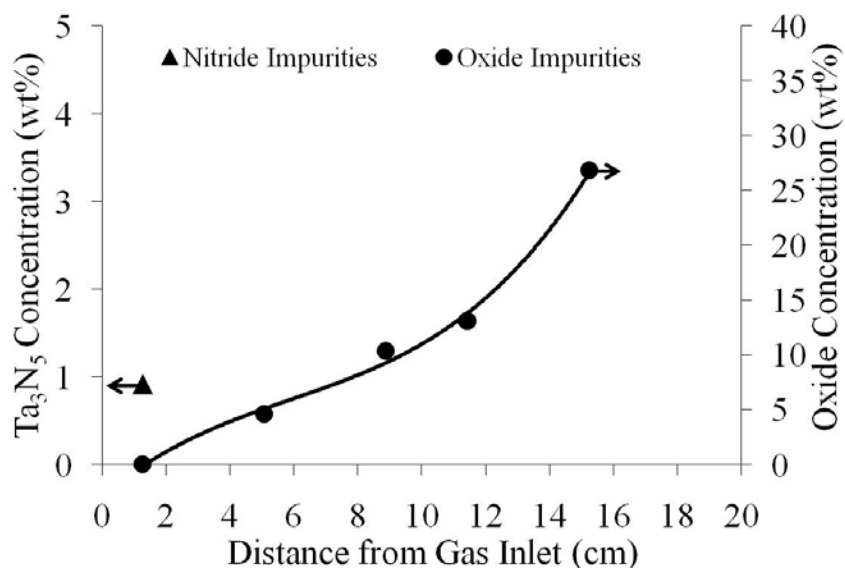


**Figure 3.3.4b** Minor phase concentration as a function of distance from gas inlet. (1150°C, 20hrs, 2.5cm/min NH<sub>3</sub> flow) Measurement location corresponds to distance measured from gas inlet to center of sample. Oxide minor phases are a mixture of Ba<sub>3</sub>Ta<sub>5</sub>O<sub>15</sub> and Ba<sub>5</sub>Ta<sub>4</sub>O<sub>15</sub>.

Only the first position (1.3cm) lacked oxide minor phases, where in section 3.3.1 at 1000°C the first four positions (1.3cm to 11.5cm) lacked detectable oxide minor phases. Results are rationalized through enhanced NH<sub>3</sub> decomposition to N<sub>2</sub> and H<sub>2</sub> and decreased active nitrogen content at higher temperatures (refer to section 2.3.2). It is possible to use elevated flow velocities to enhance NH<sub>3</sub> concentration at downstream positions. However, oxynitride instability at elevated temperatures becomes of increasing concern.<sup>19</sup> Therefore, the upper limit on temperature is controlled by enhanced NH<sub>3</sub> decomposition and structural instability of the oxynitride. Aguiar et al. discuss the lower limit on temperature (~900°C) as slow reaction kinetics.<sup>33</sup> Lower boundaries on synthesis temperature are attributed to limited breakdown of NH<sub>3</sub> on sample grains as well as slow gas and solid-state transport. Lower temperature synthesis of oxynitrides has been realized through flux-assisted and wet-chemistry techniques.

### 3.3.5 Furnace Configuration

Presently, small batch sizes (~1g) are used to maximize exposure to  $\text{NH}_3$ . Additionally, high flow velocities cannot be used from production of  $\text{Ta}_3\text{N}_5$  minor phases. Therefore, to improve the initial design the reaction zone was modified to rotate during synthesis at a rate of ~20 rotations/min with an alumina stir-bar placed inside the reaction zone (refer to figure 2.3.1). The rotating action of the furnace enhances sample surface exposure to the  $\text{NH}_3$  stream and improves powder homogeneity (refer to section 2.3.2). Thirty grams of a  $\text{BaCO}_3$  and  $\text{Ta}_2\text{O}_5$  mixture was placed inside the reaction zone under varying flow rates for 20 hours. (Figure 3.3.5a) No oxide phases were observed in XRD with flow velocities  $\geq 12\text{cm/min}$ . Nitrogen content of the sample at  $50\text{cm/min}$  via LECO hot-gas extraction revealed a close to ideal stoichiometry,  $\text{BaTaO}_2\text{N}_{0.98(3)}$

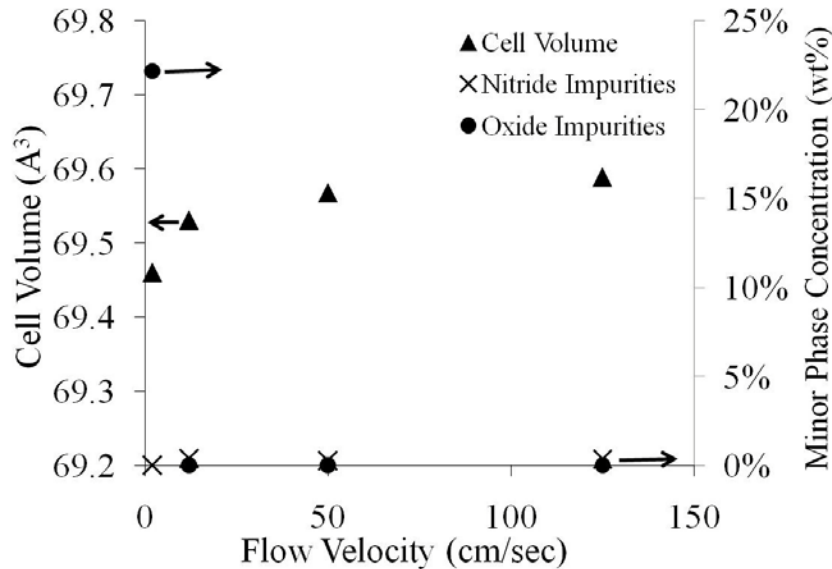


**Figure 3.3.5a**  $\text{BaTaO}_2\text{N}$  cell volume and minor phase concentration as a function of flow velocity with a rotary furnace design. ( $1000^\circ\text{C}$ , 20hrs, samples positioned between 5.0 & 13.0cm). Oxide minor phases are a mixture of  $\text{Ba}_3\text{Ta}_5\text{O}_{15}$  and  $\text{Ba}_5\text{Ta}_4\text{O}_{15}$  and the nitride minor phase is  $\text{Ta}_3\text{N}_5$ .

While changing flow velocity in a non-rotary system (section 3.3.2), it was observed that high concentrations of  $\text{NH}_3$  caused  $\text{Ta}_3\text{N}_5$  formation before solid-state diffusion processes could stabilize the oxynitride. Interestingly, greater flow velocities ( $>12\text{cm/min}$ ) can be used with rotation while achieving minimal production of  $\text{Ta}_3\text{N}_5$  ( $<0.5\text{wt}\%$ ). This is consistent with an increase in sample homogeneity. Additionally, a varying gas-sample interaction may have a contributing role. As rotation proceeds, the exposed particle surface to the atmosphere is constantly changing. This provides fluctuations in the time each surface experiences to the  $\text{NH}_3$  stream and allows solid-state transport and improved particle mixing to progress before a binary nitride phase can form.

### 3.3.6 Precursor Form

Section 3.3.1-3.3.2 indicated production of  $\text{Ta}_3\text{N}_5$  minor phases in all  $\text{ATaO}_2\text{N}$  compositions ( $\text{A}=\text{Ca},\text{Sr},\text{Ba}$ ). Decreasing diffusion distances, increasing particle homogeneity and enhancing solid-state transport can limit irreversible  $\text{Ta}_3\text{N}_5$  formation. For example, Marchand et al. eliminated binary nitride formation through reacting precursors in air to form a multicomponent oxide (usually pyrochlore) prior to ammonolysis.<sup>8</sup> Others have used flux-assisted techniques to accomplish the same task.<sup>16</sup> Additionally, different precursor chemistries can alter reaction rate and powder microstructure. Therefore, three precursor chemistries were evaluated (1-3) as means for tailoring reaction rate, the perovskite structure, anion composition and powder microstructure.

- 1) Ammonolysis of a  $\text{SrCO}_3$  and  $\text{Ta}_2\text{O}_5$  (ST) mixture (examined in sec. 3.3.3)

- 2) Ammonolysis of a multicomponent-precursor oxide (PO),  $\text{SrTaO}_{3.5}$ , formed from pre-reacting  $\text{SrCO}_3$  and  $\text{Ta}_2\text{O}_5$  in air
- 3) Ammonolysis of  $\text{SrCO}_3$ - $\text{Ta}_2\text{O}_5$  mixture with flux additions (FA). The flux composition was a cation stoichiometric mix of  $\text{SrCl}_2$  and  $\text{KCl}$

### 3.3.6.1 Reaction Rate (Powder XRD)

Cell volume and minor phase concentration as a function of distance from the gas intake are shown in **figures 3.3.6.1a & b**, respectively. The ammonolysis treatment was 20hrs at  $1000^\circ\text{C}$  (for ST and PO) or  $900^\circ\text{C}$  (for FA) with a flow velocity of  $2.5\text{cm}/\text{min}$ .

- A. (ST) Consistent perovskite cell volumes to  $11.5\text{cm}$  followed by a progressive decrease at further positions ( $15\text{cm}$  and  $19\text{cm}$ ). (**Figure 3.3.6.1a**) As distance increased from the gas intake, minor oxide phases ( $\text{Sr}_2\text{Ta}_2\text{O}_7$ ) increased. (**Figure 3.3.6.1b**)  $\text{Ta}_3\text{N}_5$  concentrations were low (refer to **Figure 3.3.3b**).
- B. (PO) Minimal change in the perovskite cell volume throughout the reaction zone. (**Figure 3.3.6.1a**) As distance increased from the gas intake ( $\geq 15.0\text{cm}$ ), minor oxide phases increased. (**Figure 3.3.6.1b**) No  $\text{Ta}_3\text{N}_5$  minor phases were detectable.
- C. (FA) A similar perovskite cell volume between all samples. (**Figure 3.3.6.1a**) No observed minor oxide or nitride phases (not shown)

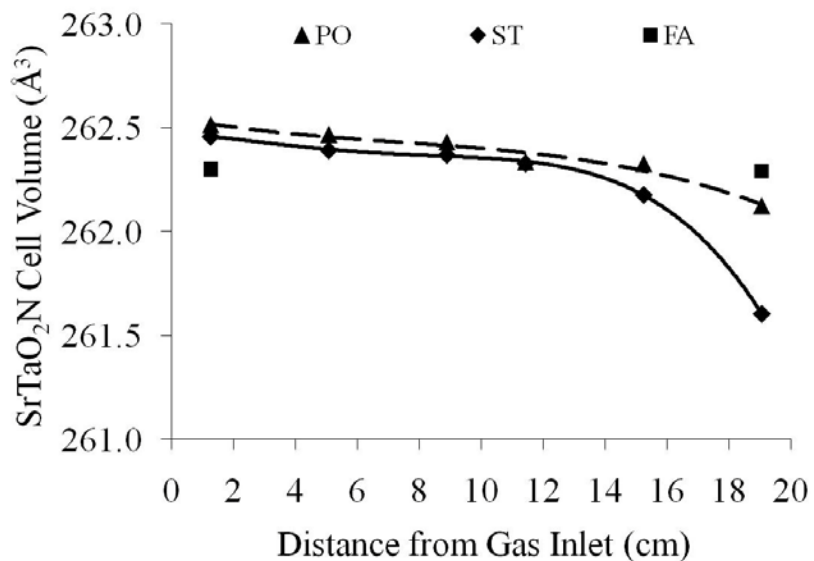


**Figure 3.3.6.1a** SrTaO<sub>2</sub>N cell volume as a function of distance from gas inlet (1000°C, 20hrs, 2.5cm/min NH<sub>3</sub> flow) Measurement location corresponds to distance measured from gas inlet to center of sample. PO = Precursor oxide, ST = Carbonate/oxide mixture, FA = flux-assisted carbonate/oxide mixture.

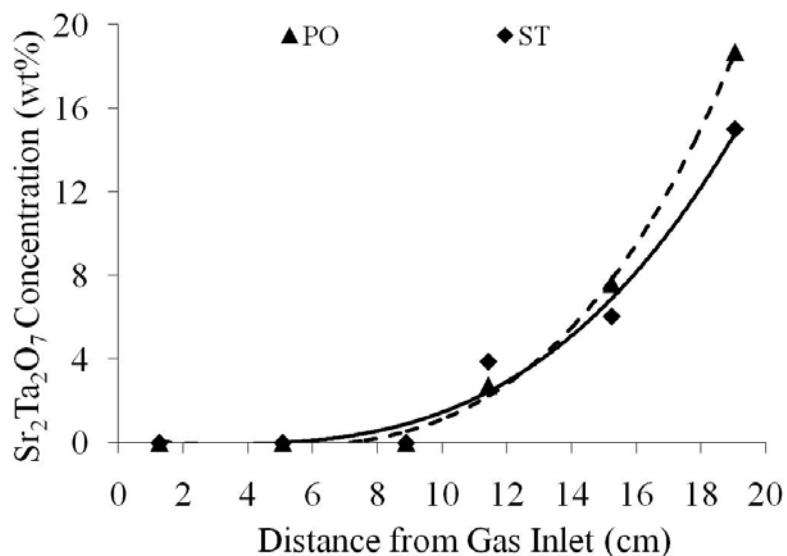


**Figure 3.3.6.1b** Sr<sub>2</sub>Ta<sub>2</sub>O<sub>7</sub> minor phase concentration as a function of distance from gas inlet (1000°C, 20hrs, 2.5cm/min NH<sub>3</sub> flow). Measurement location corresponds to distance measured from gas inlet to center of sample. PO = Precursor oxide, ST = Carbonate/oxide mixture.

Flux additions enhanced oxynitride formation kinetics, since no oxide phases were observed. This is understood through an enhancement in solid-state transport. Upon heating, the flux melts, promoting transport of solid species through either solution-precipitation or capillary action. In addition, adding flux improved utilization of available ammonia, since all samples showed a complete oxynitride conversion. Where, without flux, extended reaction times are required.

### 3.3.6.2 Perovskite Structure (Powder XRD)

The peak profile of the perovskite changed as a function of precursor chemistry. ST and PO samples have greater broadening compared to FA samples. (**Figure 3.3.6.2a**) Broadening is attributed to instrumental and sample effects, where sample broadening is a combination of grain size and microstrain.<sup>34</sup> Rietveld analysis with TOPAS software was used to separate the different contributions.

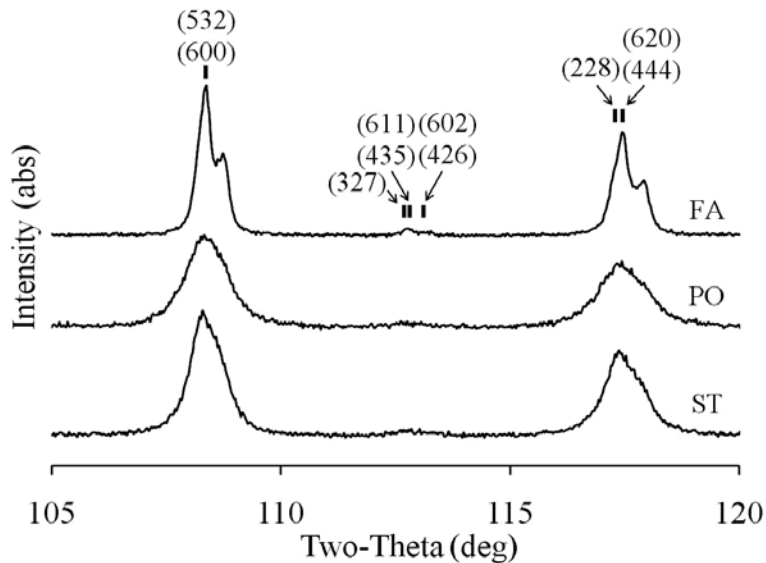


**Figure 3.3.6.2a** Peak profiles after synthesizing SrTaO<sub>2</sub>N in ammonia (20hrs, 0.5” sample position, 1000°C) with three different precursor chemistries: flux assisted (FA), solid-state with SrTaO<sub>3.5</sub> (PO), solid-state with SrCO<sub>3</sub>-Ta<sub>2</sub>O<sub>5</sub> mixture.

ST samples show an increase in microstrain as grain size decreases, suggesting poor crystallinity or internal mobility. (Figure 3.3.6.2b) For PO samples, both size and strain decreased as distance from the gas intake increased. (Figure 3.3.6.2c) No mechanism for this effect is known. Flux additions (FA) resulted in minimal strain broadening (<5%) and larger crystallites (~250nm), consistent with enhanced solid-state transport.

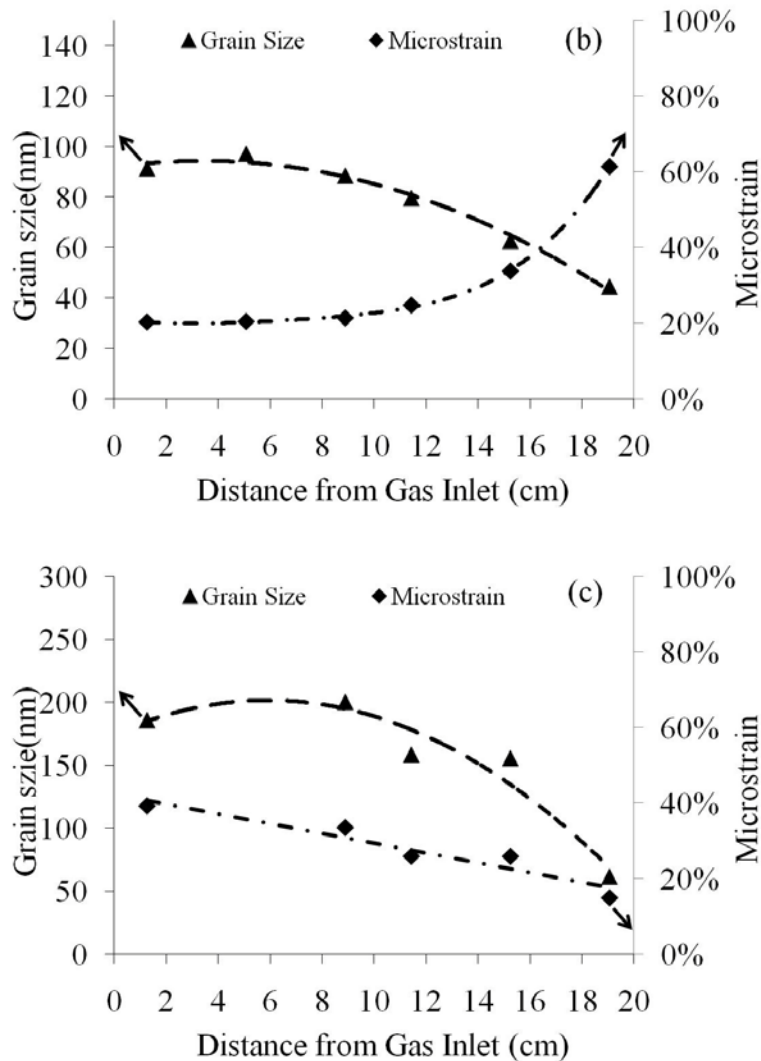


**Figure 3.3.6.2b-c** Microstrain and grain size response of SrTaO<sub>2</sub>N derived from (b) a SrCO<sub>3</sub>-Ta<sub>2</sub>O<sub>5</sub> precursor (ST) and (c) a SrTaO<sub>3.5</sub> precursor (PO).

Further reacting PO samples for an additional 20 hours at 1000°C under a 2.5cm/min flow of NH<sub>3</sub> (total 40hrs) produced no observable structural relaxation or annealing via a minimal change in peak broadening. (**Figure 3.3.6.2d**) Crystallinity is of utmost importance for optimal property response in photocatalysis. For example, TiO<sub>2</sub> has limited photocatalytic response without structural annealing at elevated temperatures.<sup>35</sup> Therefore, it would be desirable to use flux-assisted methods (FA), since high temperature (>1000°C) annealing should be used with caution from limited oxynitride stability.<sup>19</sup>

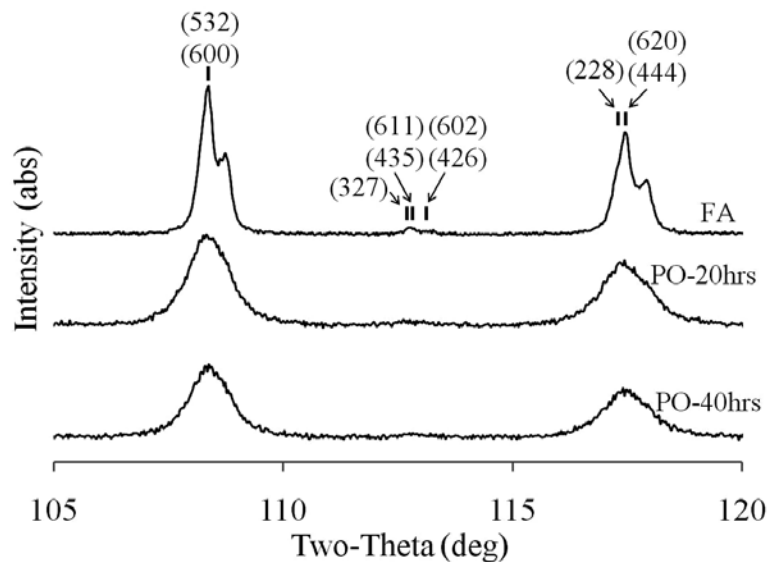


**Figure 3.3.6.2d** SrTaO<sub>2</sub>N diffraction peak profile after synthesizing in ammonia (20hrs and 40hrs, 1.3cm sample position, 1000°C) with two different precursor chemistries, flux assisted (FA) and solid-state with SrTaO<sub>3.5</sub> (PO).

### 3.3.6.3 Anion Composition (LECO Hot-Gas Extraction)

Samples at positions 1.3cm through 9.0cm were combined and sent for compositional analysis (LECO, hot-gas extraction). Analysis provided compositions of (SrTa)<sub>1.01(1)</sub>O<sub>2.00(2)</sub>N<sub>0.99(2)</sub> and (SrTa)<sub>0.96(1)</sub>O<sub>1.90(2)</sub>N<sub>1.14(2)</sub> for ST and PO samples,

respectively. This was not expected, since  $Ta_3N_5$  was identified as a minor phase in ST samples and not PO samples (via XRD). Other possible theories are adsorbed nitrogen species (e.g. NH complexes) or an excess nitrogen exchange for oxygen during ammonolysis.

#### 3.3.6.4 Powder Microstructure (SEM)

Prior to ammonolysis,  $SrTaO_{3.5}$  has a hexagonal, platelet morphology. (**Figure 3.3.6.4a-b**) After ammonolysis of  $SrTaO_{3.5}$  for 20 hours (PO), retention of the crystal shape is apparent with change in topography and/or slight spallation. (**Figure 3.3.6.4c**) The ST sample had small grains,  $\sim 100nm$ , and was highly agglomerated. (**Figure 3.3.6.4d**) Flux additions (FA) showed growth into larger, rod-like crystals. (**Figure 3.3.6.4e**) It is uncertain as whether such growth is a natural, oxynitride crystal habit or if flux interaction preferentially “poisons” or changes the surface energy of planes.

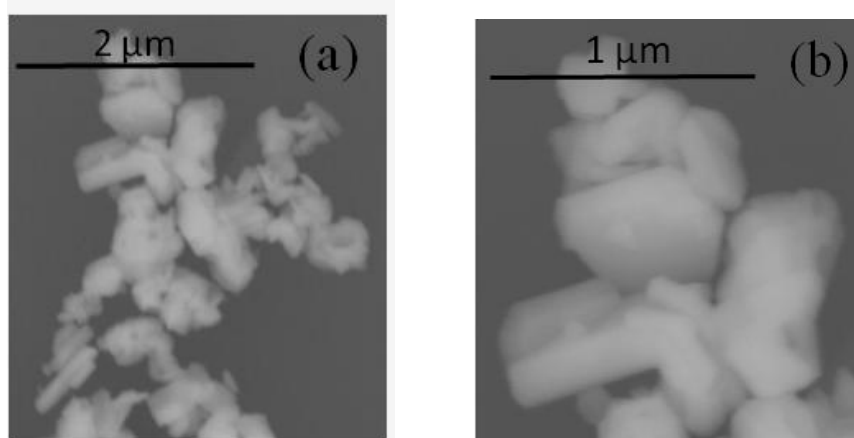


**Figure 3.3.6.4a-b**  $SrTaO_{3.5}$  powder after reacting at  $1000^{\circ}C$  for 48hrs in air.

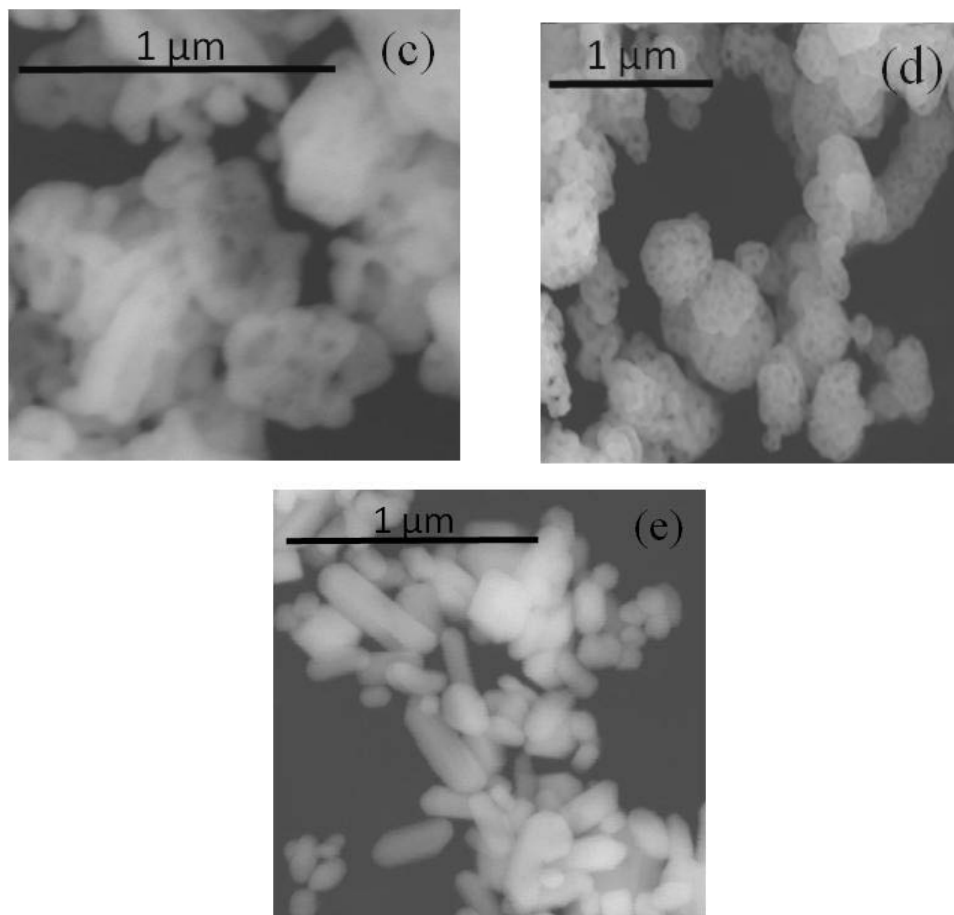


**Figure 3.3.6.4c-e** Different precursor chemistries reacted at 1000°C for 20hrs under an NH<sub>3</sub> flow of 2.5cm/min. **(c)** SrTaO<sub>3.5</sub> (PO), **(d)** SrCO<sub>3</sub> and Ta<sub>2</sub>O<sub>5</sub> mixture (ST) **(e)** Flux assisted SrCO<sub>3</sub> and Ta<sub>2</sub>O<sub>5</sub> mixture (FA).

### 3.6 CONCLUSION

The characteristics of NH<sub>3</sub> decomposition were exploited to control reaction rate and purity of BaTaO<sub>2</sub>N powders (sec. 3.3.1-3.3.2 & 3.3.4-3.3.5). Temperature should be held low upstream of the reaction chamber to minimize premature NH<sub>3</sub> decomposition. To maximize the amount of active nitrogen and non-dissociated NH<sub>3</sub>, samples should be placed closer to the gas inlet (sec. 3.3.1). Upper boundaries on flow velocity are dictated by overnitridation and production of Ta<sub>3</sub>N<sub>5</sub>; whereas, the lower boundary is selected by reaction rate (sec. 3.3.2). With solid-state synthesis, the range of unable synthesis

temperatures is narrow and between 900 -1000°C (sec. 3.3.4). Higher temperatures promote thermal instability of oxynitrides and enhance premature decomposition of NH<sub>3</sub> to N<sub>2</sub>-H<sub>2</sub>. It is possible to use greater NH<sub>3</sub> flow rates at high temperatures to enhance concentration of NH<sub>3</sub> and thus stabilize a loss of structural nitrogen; however, oxynitride decomposition becomes of increasing concern. Below 900°C oxynitride production rate is slow and limited by solid-state diffusion, gas transport and lower concentrations of active nitriding species. These limitations were ameliorated by a larger-batch production process (rotary furnace->30grams) that maintained powder purity (low Ta<sub>3</sub>N<sub>5</sub> concentrations) (sec. 3.3.5). The rotary calcine approach enables investigation of sintering where larger quantities of material are required.

Through proper control over NH<sub>3</sub> decomposition, ATaO<sub>2</sub>N (A=Ba,Sr,Ca) compounds were synthesized and formation abilities compared (sec. 3.3.1 & sec. 3.3.3). A change in A-site composition from barium or strontium to calcium produced increasing amounts of Ta<sub>3</sub>N<sub>5</sub>, inhibiting formation of phase-pure CaTaO<sub>2</sub>N. Results were rationalized through a possible lower CaTaO<sub>2</sub>N structural stability. Observations of phases present during the CaTaO<sub>2</sub>N experiment (via XRD), when excessive Ta<sub>3</sub>N<sub>5</sub> formed, indicated no observable calcium-rich minor phases. This led to batching precursors with excess CaCO<sub>3</sub> in an attempt to form a calcium-rich perovskite (sec. 3.3.3.1). Results suggest calcium can be incorporated into the perovskite as a B-site dopant (Ca<sub>Ta</sub>'') with charge neutrality maintained by replacing nitrogen with oxygen (O<sub>N</sub>·). Using a flux-assisted method to form SrTaO<sub>2</sub>N enhanced reaction kinetics, crystallinity and grain size, compared to ammonolysis of a carbonate/oxide mixture or a pre-reacted multicomponent oxide (SrTaO<sub>3.5</sub>) (sec. 3.3.6)

## 4 STABILITY AND SINTERING

### 4.1 INTRODUCTION

#### 4.1.1 Motivation

Dense, defect-free oxynitride ceramic are essential for electrical property measurements. However, to control purity, while creating dense ceramic, requires an understanding of material stability during sintering. Therefore, the first step is to define stability limits and degradation mechanism(s) for the perovskite oxynitride materials (sec. 4.3.1). These will be compared to the well-studied  $A_3N_4$  and  $A_2N_2O$  (A=Ge and Si) compounds. This will create a foundation for analyzing perovskite oxynitride systems. The knowledge on oxynitride stability will then provide insight into choosing sintering tactic(s) for creating dense ceramic, the foundation for sintering as described in the end of the chapter (sec. 4.3.2).

#### 4.1.2 Literature Review

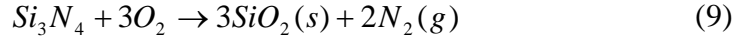
##### 4.1.2.1 Oxynitride and Nitride Stability

At high temperatures, nitrides decompose more readily than oxides. This is explained through a brief thermodynamic assessment.<sup>36</sup> Equations 5-10 compare the free energy change for the decomposition reactions of  $Si_3N_4$  and  $SiO_2$  at 1500K. Decomposition to elemental components requires similar energies (eqn. 5-6). Differences become apparent when forming diatomic gases, where  $N_2$  is more stable and has lower free energy than  $O_2$ . (eqn. 7-8) This leads to lower free energy for the corresponding dissociation reaction to combined elements and hence, lower stability for nitrides compared to oxides.

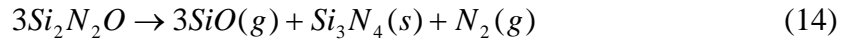




Stability is also dependent upon oxygen content. Traces of oxygen are always present within the furnace, on the material surface, or as lattice species. Reaction between  $Si_3N_4$  and  $O_2$  proceeds through two mechanisms, low temperature oxidation (eqn. 9) and high temperature oxidation. (eqn. 10)



Thermal stability of dual anion systems,  $A_2N_2O$  (where A=Ge or Si), illustrates phase decomposition to binary components.<sup>37</sup> (eqn 11) The oxide,  $AO_2$ , and nitride,  $A_3N_4$ , further break down according to equation 12 and 13. The nitride decomposition rate (fast for  $Ge_3N_4$  and slow for  $Si_3N_4$ ) leads to the following equations 14 and 15.



To summarize, two main instabilities are noted for nitrides and oxynitrides, depending upon oxygen partial pressure. High oxygen contents result in oxidation, whereas inert atmospheres result in phase decomposition and nitrogen loss. Means for extending stability have been through 1) surface passivation to limit oxygen attack, 2) use of nitrogen overpressure to suppress nitrogen loss and 3) compositional modifications.

#### 4.1.2.2 Perovskite Oxynitride Stability

Few papers have been dedicated to high temperature stability of perovskite oxynitrides. Thermal treatment in air oxidizes the oxynitride ( $ABO_2N$ ), usually to a

layered perovskite ( $ABO_{3.5}$ ), through an intermediate state.<sup>38</sup> The onset of oxidation varies between 400°C and 600°C, depending upon composition. The intermediate state is defined as a full replacement of lattice nitrogen with oxygen and a partial retention of lattice nitrogen in the form of a di-nitrogen metal bond with the B-Site cation.<sup>39</sup> Structural conversion from the intermediate state to the final oxide (typically the layered perovskite,  $ABO_{3.5}$ ) occurs at an elevated temperature with a release of nitrogen. A thermochemical study shows weakly bonded di-nitrogen species with structural change from the intermediate to the layered perovskite requiring a majority of the enthalpy of oxidation.<sup>40</sup>

Aguiar et al. investigated thermal stability of  $LaTiO_2N$ ,  $SrNbO_2N$  and  $SrTaO_2N$  in various oxygen pressures.<sup>19</sup> A 20% oxygen concentration resulted in the previously described oxidation process via an intermediate path. Partial  $O_2$  pressures between 20% and 0.5% oxygen resulted in different oxide products with varying chemistries (such as  $A_5B_4O_{15}$ ). Pure argon resulted in nitrogen loss, reduction of the transition metal and phase decomposition. The degradation temperature and rate of decomposition was material dependent with increasing stability in the order,  $SrNbO_2N < LaTiO_2N < SrTaO_2N$ . The range of instability temperatures varied from 870°C to 1200°C.

#### **4.1.2.3 Nitride and Oxynitride Sintering**

As discussed in sec. 4.2.1-4.2.2, (oxy)nitrides tend to degrade at high temperatures (oxidation/decomposition). In addition, compared to oxides, nitrides have greater covalency facilitating refractory behavior and low ionic mobility. These factors make sintering evasive and application use limited. Therefore, multiple tactics to create dense ceramic have been identified. For example, stability can be extended to regions of noticeable densification (process route 1). Degradation can be kinetically limited,

allowing sintering outside stability regimes (process route 2). Sintering temperature can be reduced to lie within the stability regions (process route 3). Some experimental approaches are listed in **Table VI**.

**Table VI.** Various Sintering Tactics Identified in Literature (\* - Investigated in this Study)

Process Route	Process	Chapter
-	*Pressure-less sintering*	4
1	*Gas overpressure*	4
2	Immersion in powder beds	
3	HIPping	
3	*Mechanical pressure*	4
3	*Particle size reduction*	4
3	Microwave sintering	
3	Reaction sintering	
3	Liquid phase sintering	
3	Dopants	
3	*Sol-gel*	5 & 6

Current work investigates sintering under atmospheric, gas and mechanical pressure with a brief study into particle size reduction (sec. 4.3.1-4.3.3). Chapter 6 and 7 examine reducing sintering temperatures via sol-gel tactics.

#### 4.1.3 Work Plan

Thermal stability of SrTaO<sub>2</sub>N and BaTaO<sub>2</sub>N is evaluated with thermogravimetric analysis (TGA), XPS, room temperature XRD and *in situ*, high temperature XRD (HTXRD). (Sec. 4.3.1) The newly obtained knowledge is then applied to various sintering methods (pressure-less, gas overpressure and spark plasma (SPS)) in attempt to create dense ceramic. (Sec. 4.3.2)

## **4.2 EXPERIMENTAL**

### **4.2.1 Powder Synthesis**

Phase-pure starting powders were synthesized with the rotary calciner discussed in chapter 3. Briefly, 30 grams of an  $ACO_3$  ( $A=Sr,Ba$ ) and  $Ta_2O_5$  mixture was placed inside a rotary calciner and ammonolyzed at  $1000^\circ C$  for 20hrs at a 50cm/min ammonia flow. Phase purity was verified via XRD and LECO, hot-gas extraction.

### **4.2.2 Thermogravimetric Analysis**

Thermogravimetric analysis was performed with a Netzsch Jupiter, platinum furnace. Approximately 150mg of oxynitride powder was placed into an alumina sample holder. The sample was purged under UHP nitrogen overnight prior to measurement, until the oxygen content measured at the furnace outtake (with a Thermox, zirconia cell oxygen analyzer) was  $<50$ ppm. The sample was then heated under 40ml/min of UHP nitrogen to  $1300^\circ C$  at  $10^\circ C/min$ , held for 30min and subsequently cooled at  $10^\circ C/min$ . To remove the effect of buoyancy and background noise in the data, a measurement using dried alumina powder was performed using the same experimental procedure. The background measurement was then subtracted from the oxynitride sample data.

### **4.2.3 *In situ*, High Temperature DRIFT**

IR measurements of oxynitride powder were performed with a Nicolet FT-IR spectrometer over the range of  $650cm^{-1}$  to  $4000cm^{-1}$ . The spectra resolution and scan velocity were set at  $4cm^{-1}$  and  $0.4679cm^{-1}/sec$ , respectively. Samples were heated to a temperature of  $800^\circ C$  with spectra taken every  $100^\circ C$ . Temperature was monitored with a platinum thermocouple immersed in the powder bed. The atmosphere was dry, carbon dioxide-free air with a flow rate of  $\sim 30ml/min$ . A total of 200 scans at each temperature were taken to improve the signal to noise ratio.

#### **4.2.4 *In situ*, High Temperature XRD**

Patterns were collected on a Siemens D5000 diffractometer with a  $\text{Co}_{K\alpha}$  radiation source set at 40kV and 30mA. Samples were prepared by mixing oxynitride powder with isopropyl alcohol and applying onto a 99.6% alumina substrate. Data was collected over the angular range of  $10^\circ < 2\theta < 80^\circ$  stepping at  $0.02^\circ$  with count times of 1 second per step. The sample was heated to  $1250^\circ\text{C}$  for 30 minutes with diffraction patterns taken every  $50^\circ\text{C}$ .

#### **4.2.5 Room Temperature Powder XRD**

Patterns were collected on a Phillips Bruker diffractometer with a  $\text{Cu}_{K\alpha}$  radiation source set at 40kV and 30mA. Samples were prepared by mixing oxynitride powder with IPA and applied onto a single crystal, zero background sapphire holder. Data was collected over the angular range of  $10^\circ < 2\theta < 70^\circ$  or  $10^\circ < 2\theta < 140^\circ$  stepping at  $0.02^\circ$  with count times of 3 seconds per step.

#### **4.2.6 XPS**

XPS was performed with a PHI Quantera SXM spectrometer using a monochromated  $\text{Al}_{K\alpha}$  radiation source (1486.6eV) operating at 40W. The sample area investigated was  $0.04 \text{ mm}^2$ . High resolution spectra were collected at 69eV pass energy and 0.1 eV step size with an incident angle of  $45^\circ$  relative to the sample surface. The signal to noise ratio was 6:1. Charging effects were minimized through an electron gun set at 1V and  $20\mu\text{A}$ . The binding energy was calibrated using the  $\text{C}_{1s}$  peak associated with an adsorbed carbon surface layer at 284.6eV. Peak position and intensity were allowed to vary.

#### 4.2.7 Gas Overpressure

For gas overpressure experiments, a graphite resistive, hot isostatic press (HIP) was used. Powder or pellet samples were placed in an alumina crucible with an alumina top and set inside the pressure vessel. Where, upon the chamber was then repeatedly evacuated (<100 millitorr) and backfilled with nitrogen or argon. After the final backfill, the chamber was further pressurized to the desired level at room temperature, followed by a subsequent heating to the desired temperature for 1hr with associated further increase in pressure. Pellets were formed through isostatically pressing powders at ~2,000 psi followed by a cold isostatic pressing at 25,000psi. After pressing, pellets had approximate green densities of 50-60%.

#### 4.2.8 Axial Pressure (Spark Plasma Sintering)

Samples were spark plasma sintered (SPS) at Chiba University in Japan. Prior to sintering, powder was hand ground in an agate mortar for 30 minutes to de-agglomerate the powder. Approximately 1.5 grams of powder was then placed inside a graphite die and sintered under a nitrogen atmosphere, while varying sintering temperature and pressure. The setup is schematically shown in figure 4.2.8a. For comparison, some of the SrTaO<sub>2</sub>N powder was processed through a nanomizer mill at Chiba University to further reduce particle size and break up hard agglomerates.

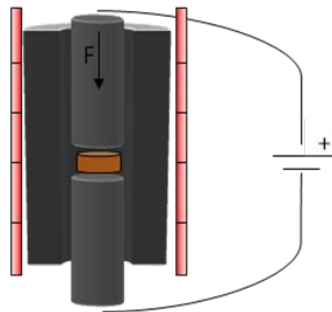


**Figure 4.2.8a:** SPS setup.

## 4.3 RESULTS AND DISCUSSION

### 4.3.1 Thermal Stability

#### 4.3.1.1 Thermogravimetric Analysis

Thermogravimetric analysis probed  $ATaO_2N$  ( $A=Sr,Ba$ ) thermal stability. Under inert atmospheres, three weight losses were observed: at  $\sim 100-200^\circ C$  (1),  $\sim 400-700^\circ C$  (2), and  $\sim 950-1200^\circ C$  (3). (Figure 4.3.1.1a) After treatment, a slight discoloration attributed to oxidation was observed on the top of the sample. The larger portion underneath had a black tint for  $BaTaO_2N$  or green tint for  $SrTaO_2N$ , indicating a possible tantalum reduction.

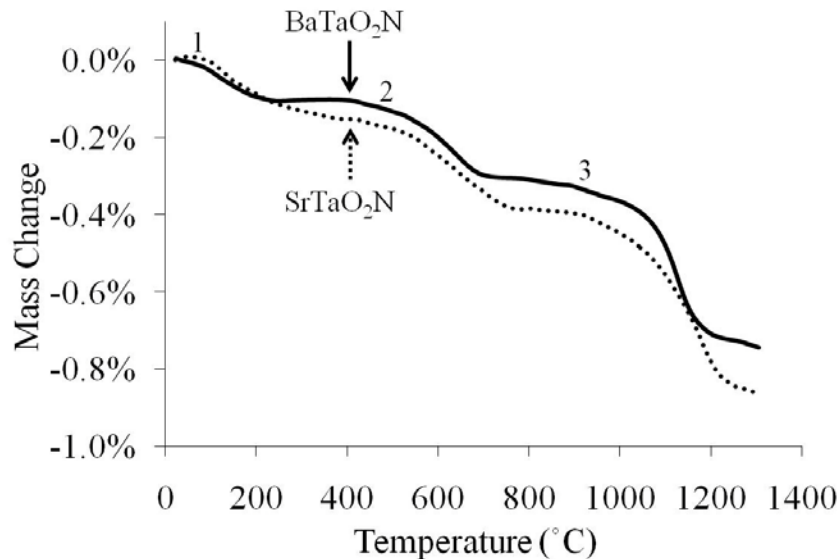


**Figure 4.3.1.1a:** Thermogravimetric results of  $BaTaO_2N$  and  $SrTaO_2N$  under UHP nitrogen ( $\sim 50$ ppm oxygen at furnace outtake, measured with zirconia oxygen cell).

*In situ*, high temperature IR examined causes of weight loss. (Figure 4.3.1.1b) Above  $400^\circ C$ , bands attributed to adsorbed water ( $3000-4000cm^{-1}$ ) completely disappeared. Above  $700^\circ C$ , the spectrum shows removal of adsorbed carbonate bands

(1400-1550 $\text{cm}^{-1}$ ). Through comparison to literature, the higher temperature,  $>950^\circ\text{C}$ , weight loss is associated with  $\text{N}_2$  evolution.<sup>19</sup> Aguiar et al. employed TGA coupled with mass spectroscopy under an inert, argon atmosphere and identified similar weight loss regimes. Water and carbon dioxide evolved at low temperatures with a higher temperature weight loss corresponding to  $\text{N}_2$  evolution.

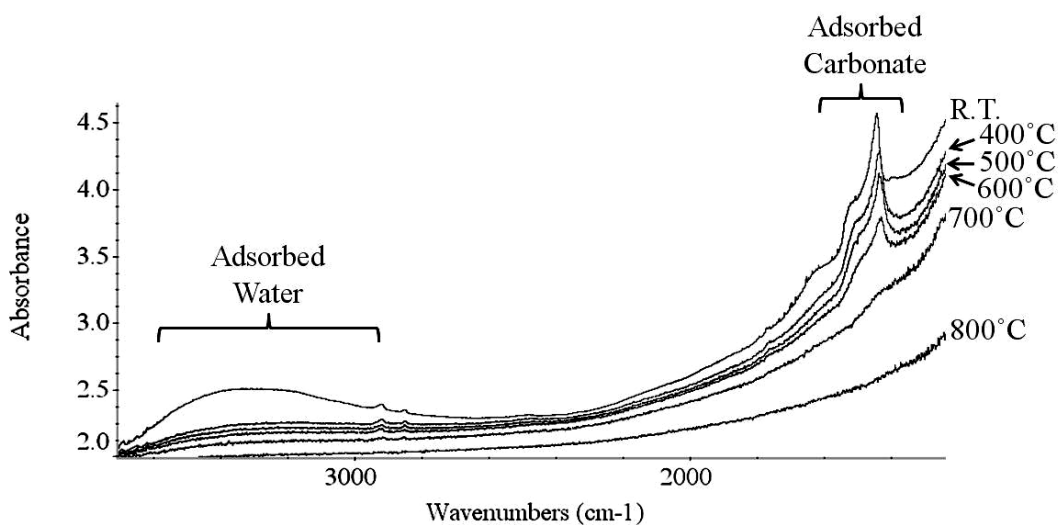


**Figure 4.3.1.1b:** Thermal treatment of “As synthesized”  $\text{SrTaO}_2\text{N}$  in *in situ*, high temperature under UHP nitrogen.

After the TGA thermal treatment,  $\text{SrTaO}_2\text{N}$  had no observable decomposition products (via XRD), a slight cell volume decrease and an increase in crystallinity (through better defined diffraction peaks). **(Figure 4.3.1.1c-d)** Slight alumina contamination was noted from reference powder used during background measurements. For  $\text{BaTaO}_2\text{N}$ ,  $\text{Ta}_4\text{N}_5$  formed, indicating a structural decomposition. **(Figure 4.3.1.1e)**

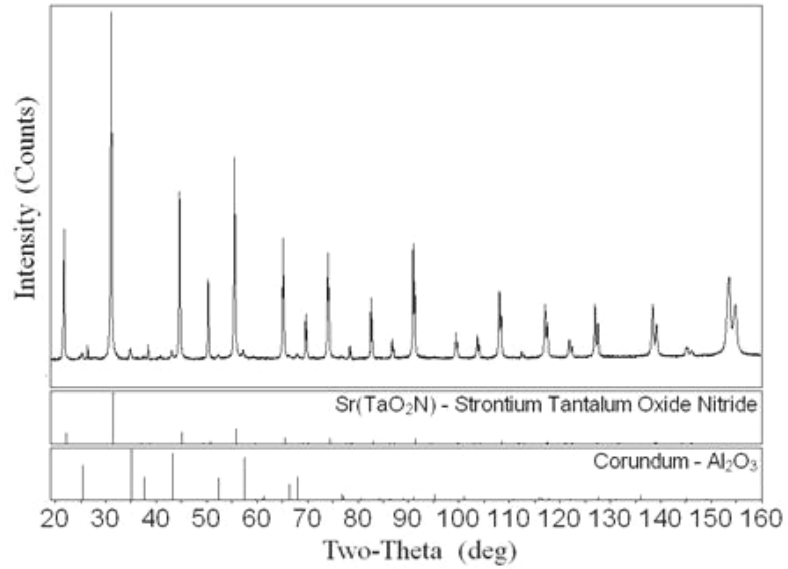


**Figure 4.3.1.1c:** Diffraction results after thermogravimetric analysis of SrTaO<sub>2</sub>N powder (1300°C for 1hr under UHP nitrogen atmosphere).

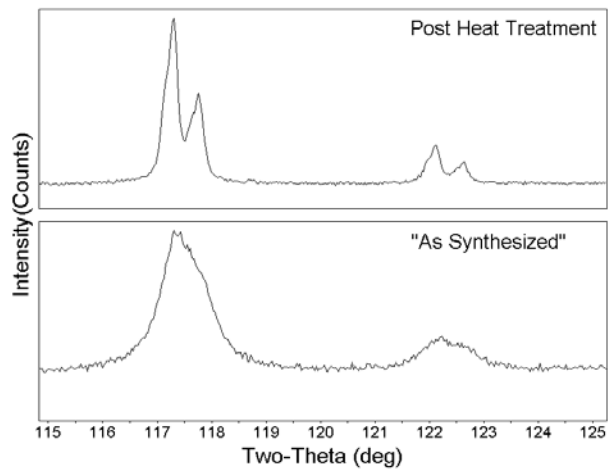


**Figure 4.3.1.1d:** SrTaO<sub>2</sub>N diffraction patterns of thermally treated (1300°C for 1hr under UHP nitrogen atmosphere) and “as synthesized” powder.

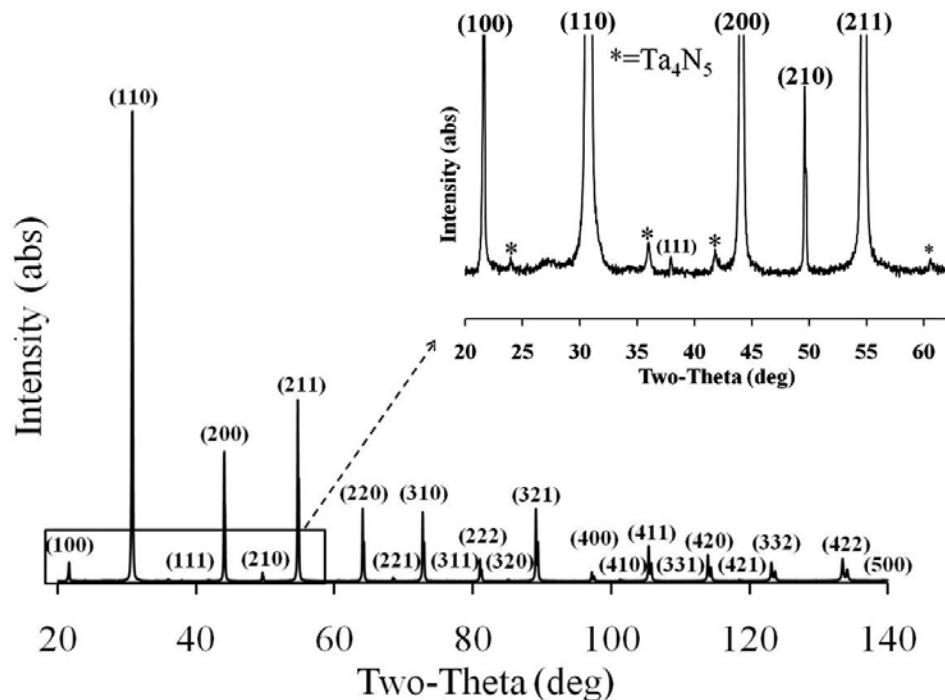


**Figure 4.3.1.1e:** Diffraction results of BaTaO<sub>2</sub>N powder after thermogravimetric analysis (\*)=Ta<sub>4</sub>N<sub>5</sub> minor phase (1300°C for 1hr under UHP nitrogen atmosphere).

Similar to literature on oxynitride stability, the current work identifies the degradation mechanism at high temperature and under inert atmospheres (low oxygen content) as loss of nitrogen and phase decomposition (for BaTaO<sub>2</sub>N). An earlier literature review (Sec. 4.1.2.2) identified the ATaO<sub>2</sub>N (A=Ca,Sr,Ba) compositions as having greater stability, compared to niobates and titanates. Clearly, B-site dependence has been demonstrated. However, A-site exchange did not result in an observable stability change (through comparing onset or concentration of nitrogen loss in the TGA signal).

#### 4.3.1.2 In situ High Temperature XRD

*In situ*, high temperature XRD (HTXRD) investigated structural stability. **Figure 4.3.1.2a and 4.3.1.2b** show the diffraction patterns and cell volume change, respectively, for SrTaO<sub>2</sub>N powder as a function of temperature under a nitrogen atmosphere (oxygen

content measured at outtake to be ~15ppm). Between room temperature and 950°C, the oxynitride is stable. After 950°C, the SrTaO<sub>2</sub>N cell volume decreases followed by oxidation to SrTaO<sub>3.5</sub>.

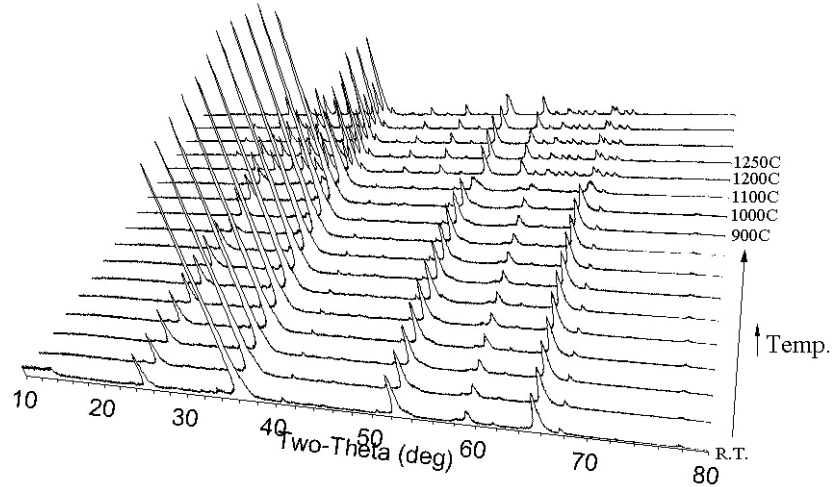


**Figure 4.3.1.2a:** XRD of SrTaO<sub>2</sub>N powder as a function of temperature under a nitrogen atmosphere (oxygen content ~15ppm).

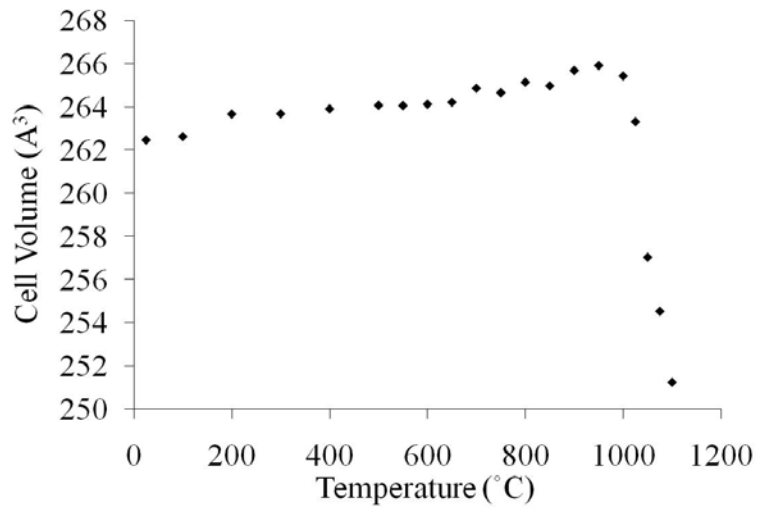


**Figure 4.3.1.2b:** Cell volume of SrTaO<sub>2</sub>N powder as a function of temperature under a nitrogen atmosphere (oxygen content ~15ppm).

Comparison of TGA and HTXRD results shows different high temperature instability mechanisms, even though atmosphere (nitrogen with ~50ppm oxygen) and

heat treatment were similar. Thermogravimetric analysis resulted in loss of weight, no observable minor phases and retention of the perovskite structure. Whereas, material in HTXRD oxidized to  $\text{SrTaO}_{3.5}$ . This is explained through differing sample setups. The sample in HTXRD was evenly spread on an alumina plate in essentially a powder monolayer. This provides high surface exposure to the incoming atmospheric oxygen. Conversely, the sample holder in TGA has a large depth, limiting oxygen exposure to only the top of the powder bed.

Interestingly, onset of pyrochlore formation (via HTXRD) and nitrogen release (via TGA) under inert atmospheres occur at a similar temperature ( $\sim 950^\circ\text{C}$ ). At this point, it is possible the system has enough thermal energy to break lattice nitrogen bonds, promoting phase decomposition or oxidation. Therefore, to retain structural integrity and anion content at these higher temperatures, an active nitrogen source would be required.

## **4.3.2 Sintering**

### **4.3.2.1 Pressure-less Sintering**

To determine densification characteristics, dilatometry was used. Onset of shrinkage was only observed after structural destabilization. (**Figure 4.3.2.1a**) This possibly explains the observed powder consolidation during high temperature synthesis in sec. 4.3.4 as result of oxynitride instability.

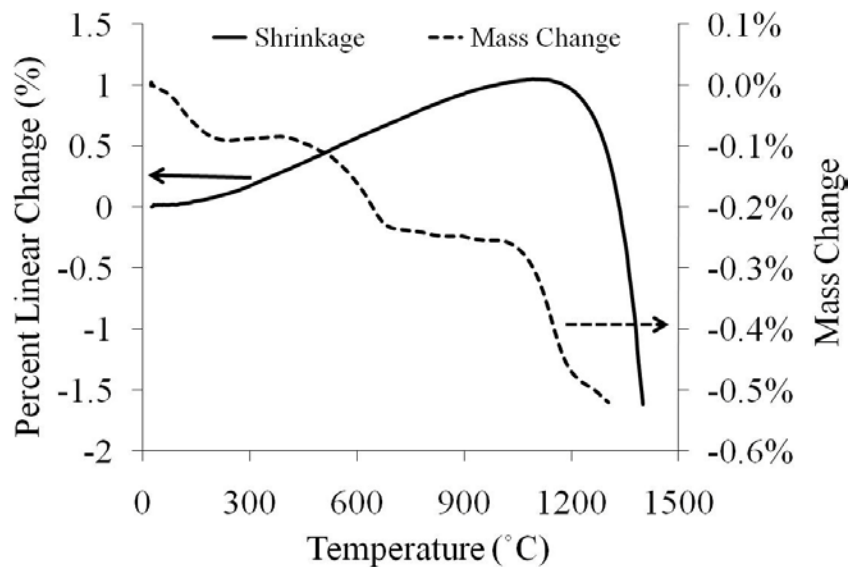


**Figure 4.3.2.1a:** Mass loss and shrinkage of BaTaO<sub>2</sub>N powder as a function of temperature under a 4% H<sub>2</sub>-balance N<sub>2</sub> atmosphere.

To investigate sintering above instability temperatures, a SrTaO<sub>2</sub>N pellet was heat treated at 1275°C under a nitrogen atmosphere. Powder diffraction of the sintered pellet indicated SrTaO<sub>2</sub>N with a minor amount of SrTaO<sub>3.5</sub>. (**Figure 4.3.2.1b**) No attempt was made at identifying the tetragonal distortion in SrTaO<sub>2</sub>N and was indexed in a cubic system.

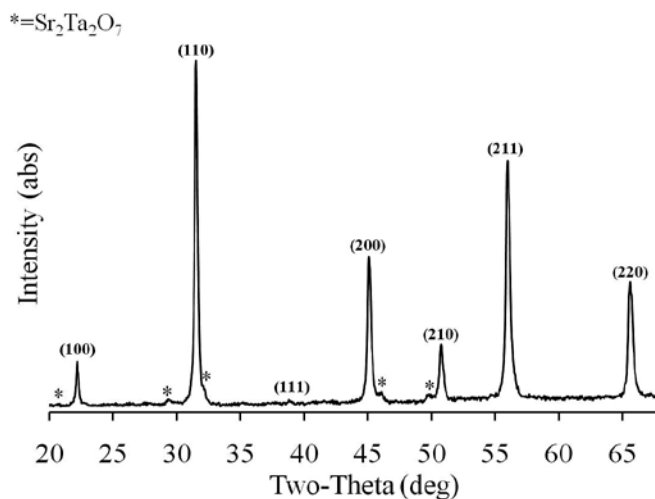


**Figure 4.3.2.1b:** XRD of SrTaO<sub>2</sub>N pellet after sintering at 1275°C in nitrogen.

The pellet was dense with formation of a white coating. XPS of the white coating showed a pure oxide phase and no indication of nitrogen. Mechanically removing the outside coating exposed a green interior. The green interior had minor amounts of nitrogen, compared to the oxynitride before heat treatment. This was determined through evaluating the lattice N1s peak area weighted to the Ta4f peak area before and after sintering. (Figure 4.3.2.1c-d) The lattice peak positions were verified through literature as well as SrTaO<sub>3.5</sub> and SrTaO<sub>2</sub>N powders.<sup>32,41</sup>

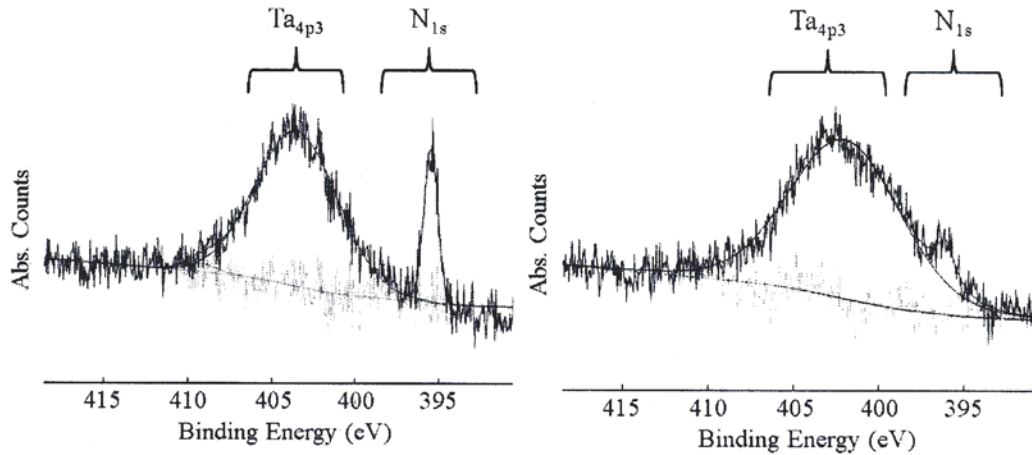


**Figure 4.3.2.1c-d:** XPS spectra of N<sub>1s</sub> environment before (left) and after (right) sintering a SrTaO<sub>2</sub>N pellet at 1275°C for 5hrs. in nitrogen.

In addition, a new, lower binding energy Ta<sub>4f</sub> chemical state developed after sintering. (Figure 4.3.2.1e) This is also supported by the shift in the Ta<sub>4p3</sub> peak in figure 4.3.2.1d. It should be noted that each Ta<sub>4f</sub> environment has two associated spin states (7/2 and 5/2) and therefore, two peaks for each observed chemical state. Comparing spectra of the sintered SrTaO<sub>2</sub>N sample to SrTaO<sub>3.5</sub> reveals the higher Ta<sub>4f</sub> energy state as Ta<sup>+5</sup> bound to oxygen. The degree of chemical shift (~4eV) and binding energy position of the lower energy Ta<sub>4f</sub> state indicates presence of a possible metallic species, Ta<sup>0</sup>, or

alternatively, a low nitrogen content bonding environment.<sup>22,42</sup> The latter seems plausible, since the  $N_{1s}$  peak shifts to  $\sim 396.1\text{eV}$  from  $\sim 395.5\text{eV}$  after sintering. This is consistent with literature reports of similar increases in the  $N_{1s}$  binding energy when comparing  $Ta_3N_5$  to tantalum phases with reduced oxidation states and lower nitrogen contents, such as  $TaN$  or  $TaN_x$ .<sup>43</sup>

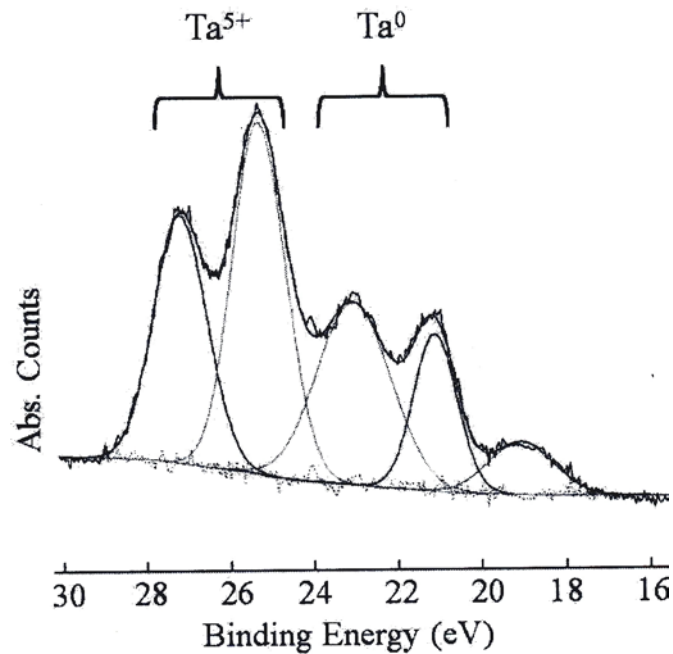


**Figure 4.3.2.1e:** Spectra of  $Ta_{4f}$  environment in the  $SrTaO_2N$  pellet interior after sintering at  $1275^\circ\text{C}$  in nitrogen.

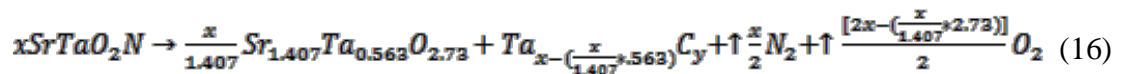
Since XRD did not indicate a metallic or nitride minor phase, the reduced tantalum is attributed to the perovskite structure. Therefore, prior to structural decomposition, it seems the oxynitride degradation mechanism is loss of nitrogen and a tantalum reduction. Alternatively, the lack of minor phases may be attributed to low concentrations or a weakly crystalline phase. However, this seems unlikely from the large concentration of reduced tantalum, as seen through comparing the relative areas of the different tantalum states.

Oxynitride powders undergo loss of structural nitrogen and phase decomposition at ~950C. This inhibits formation of dense ceramic. Hence, proceeding work in this chapter investigates extending stability through gas overpressure, and reducing sintering temperatures through spark plasma sintering (SPS). (refer to sec. 4.1.2.3) Chapter 5 and 6 investigate reducing sintering temperatures via sol-gel thin films.

#### 4.3.2.2 Gas Overpressure

Gas overpressures are commonly employed to limit degradation kinetics and extend material stability to higher temperatures when high vapor pressure components, such as nitrogen, are used. The mechanism(s) for enhancing stability is investigated through changing atmospheres. For example, use of an inert argon atmosphere provides a mechanical contribution,  $\Delta P$ , to enhancing stability. Where, an active nitrogen atmosphere stabilizes material chemically,  $\mu(N)$ , as well as mechanically. Other processing conditions examined, besides atmosphere, are temperature and pressure.

**Figures 4.3.2.2a and 4.3.2.2b** are the diffraction results after varying pressure (0.2 or 10MPa) and atmosphere (argon or nitrogen) during 1400 heat treatments of SrTaO<sub>2</sub>N powders. Treatment in argon resulted in two minor phases (via XRD), TaC and Sr<sub>1.407</sub>Ta<sub>0.563</sub>O<sub>2.73</sub> (STO). This led to the proposed high temperature, instability reaction shown in equation 16. According to the equation, the material undergoes phase decomposition and not oxidation, since no additional oxygen is required for formation of products.



Increasing argon pressure (from 0.2MPa to 10MPa) reduced concentrations of minor phases (through comparing XRD peak intensities of the minor phases weighted to

the oxynitride). However, a change in atmosphere from argon to nitrogen resulted in further decrease in minor phase production. Therefore, mechanical and chemical pressures decrease the rate of phase decomposition.

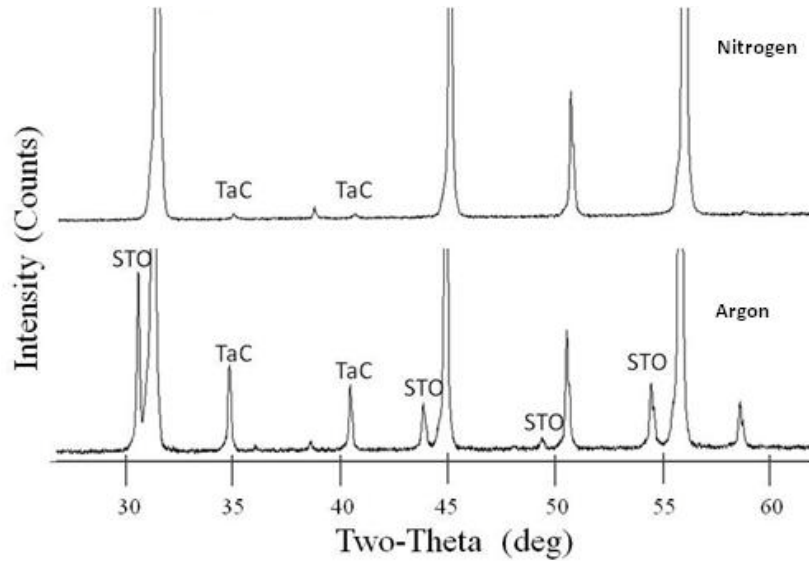


**Figure 4.3.2.2a:** Minor phases observed in SrTaO<sub>2</sub>N after 1400°C heat treatments for 1hr and 0.2MPa pressure. (TaC=Tantalum carbide, STO= Sr<sub>1.407</sub>Ta<sub>0.563</sub>O<sub>2.73</sub>).

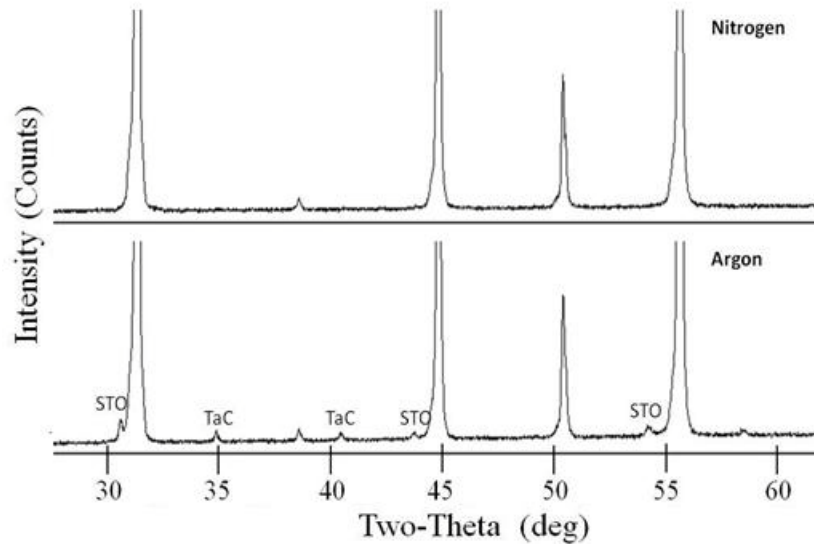


**Figure 4.3.2.2b:** Minor phases observed in SrTaO<sub>2</sub>N after 1400°C heat treatments at 1hr and 10MPa pressure. (TaC=Tantalum carbide, STO= Sr<sub>1.407</sub>Ta<sub>0.563</sub>O<sub>2.73</sub>).

Material decomposition to TaC via carbon (monoxide) contamination has been considered. Justification is through comparing results to literature.<sup>19</sup> Aguiar et al. heated a SrTaO<sub>2</sub>N sample in a TGA-DTA to 1200°C for 30 minutes under an argon atmosphere. Analysis of the thermally treated sample with XRD showed an unidentifiable minor phase with a two-theta diffraction peak at 30.2°. The current work shows the phase decomposition product, Sr<sub>1.407</sub>Ta<sub>0.563</sub>O<sub>2.73</sub>, has a 100% intensity diffraction peak at a similar 2θ position of 30.5°. Therefore, the same minor phase, Sr<sub>1.407</sub>Ta<sub>0.563</sub>O<sub>2.73</sub>, is created regardless of the presence of carbon.

Thermal treatments at 1500°C at two different nitrogen pressures, 102atm. and 10atm, indicate creation of TaC and STO, respectively. (**Figure 4.3.2.2c**)

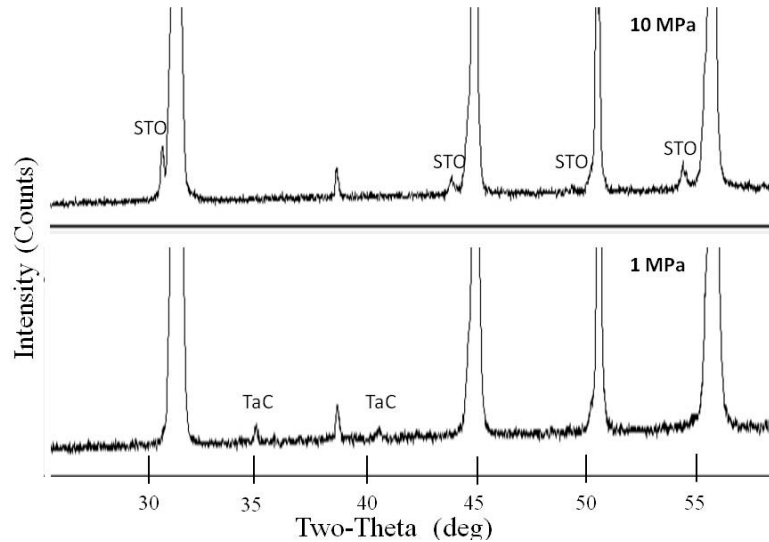


**Figure 4.3.2.2c:** Minor impurity phases of SrTaO<sub>2</sub>N at various pressure and 1500°C for 1hr. (STO= Sr<sub>1.407</sub>Ta<sub>0.563</sub>O<sub>2.73</sub> and TaC=Tantalum carbide).

**Figure 4.3.2.2d** shows the minor phases present (identified by XRD) in SrTaO<sub>2</sub>N after various sintering treatments as a function of temperature and nitrogen pressure. Oxynitride instability becomes very evident, through XRD and color variations, at

temperatures greater than 1400°C. Though stability was enhanced, there was no significant shrinkage prior to 1400°C. ( **Figure 4.3.2.2e** )

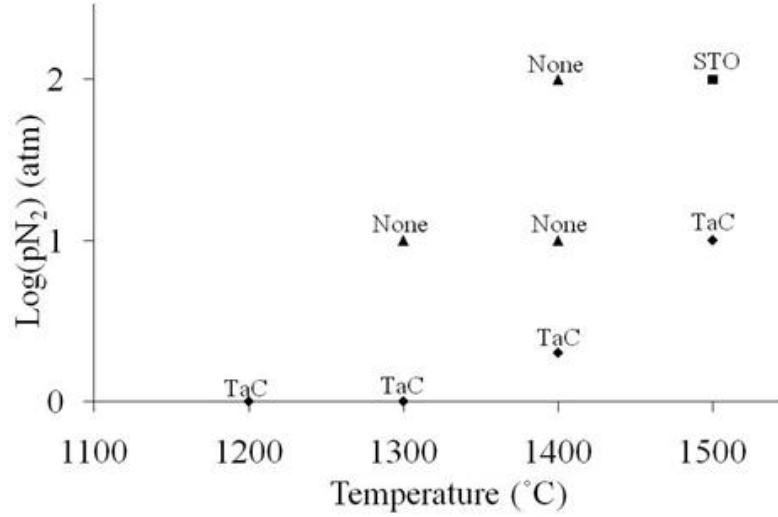


**Figure 4.3.2.2d:** Observed minor phases in SrTaO<sub>2</sub>N at various temperatures and nitrogen pressures for 1hr heat treatments. (TaC=Tantalum carbide, STO= Sr<sub>1.407</sub>Ta<sub>0.563</sub>O<sub>2.73</sub>).

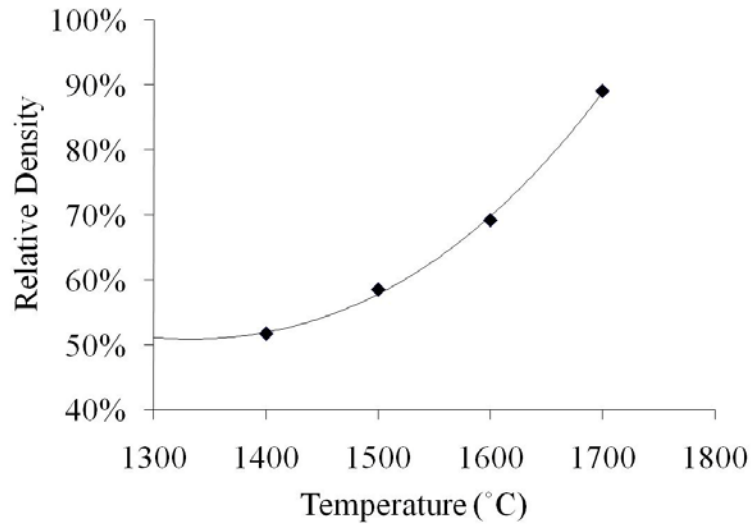


**Figure 4.3.2.2e:** Density of SrTaO<sub>2</sub>N powder compacts after various sintering treatments under ~102 atmospheres nitrogen and 1hr heat treatments.

### 4.3.2.3 Spark Plasma Sintering

Spark Plasma Sintering (SPS) was evaluated for lowering oxynitride sintering temperatures into the region of stability (<1000C). **Figure 4.3.2.3a and 4.3.2.3b** show the densification characteristics of BaTaO<sub>2</sub>N and SrTaO<sub>2</sub>N, respectively, as a function of temperature at three axial pressures. For both compounds and at all pressures, densification is only noted at temperatures of 1000°C.

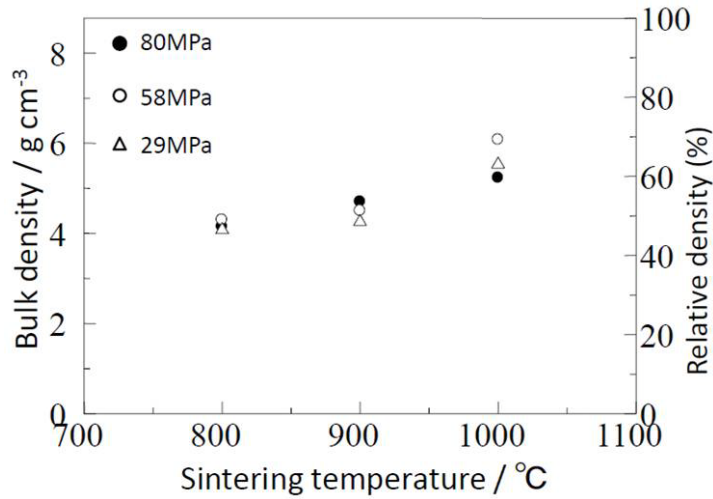


**Figure 4.3.2.3a** Densification characteristics of spark plasma sintered BaTaO<sub>2</sub>N.

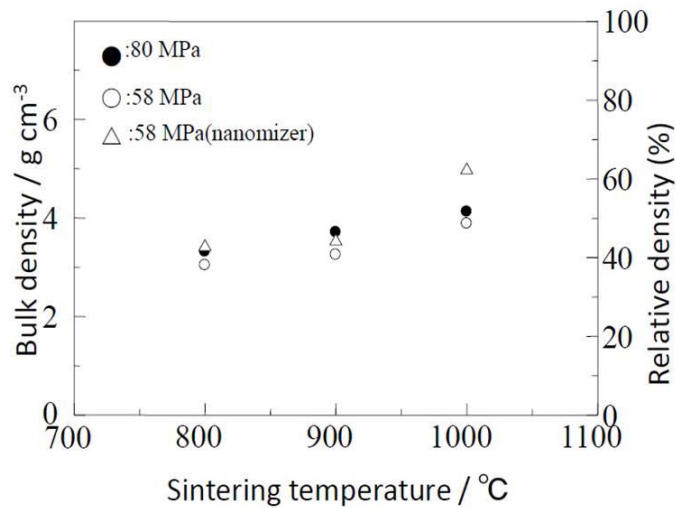


**Figure 4.3.2.3b** Densification characteristics of spark plasma sintered SrTaO<sub>2</sub>N.

Structurally, all sintered samples are phase-pure oxynitride via XRD. (**Figure 4.3.2.3c-d**) However, visual differences are noted. (**Figure 4.3.2.3e**) After an 800°C sintering, pellets retained the typical hue observed after powder synthesis of red and orange for BaTaO<sub>2</sub>N and SrTaO<sub>2</sub>N, respectively. After heat treating at 1000°C, color changed to silver (for BaTaO<sub>2</sub>N) and brown-green (for SrTaO<sub>2</sub>N). Further examining samples sintered at 1000°C revealed a loss of nitrogen (via LECO hot -gas extraction analysis). (**Figure 4.3.2.3f**) Therefore, onset of densification ( $\leq 1000^\circ\text{C}$ ) most likely originates from material instability. The microstructure indicates limited change and densification. (**Figure 4.3.2.3g**)

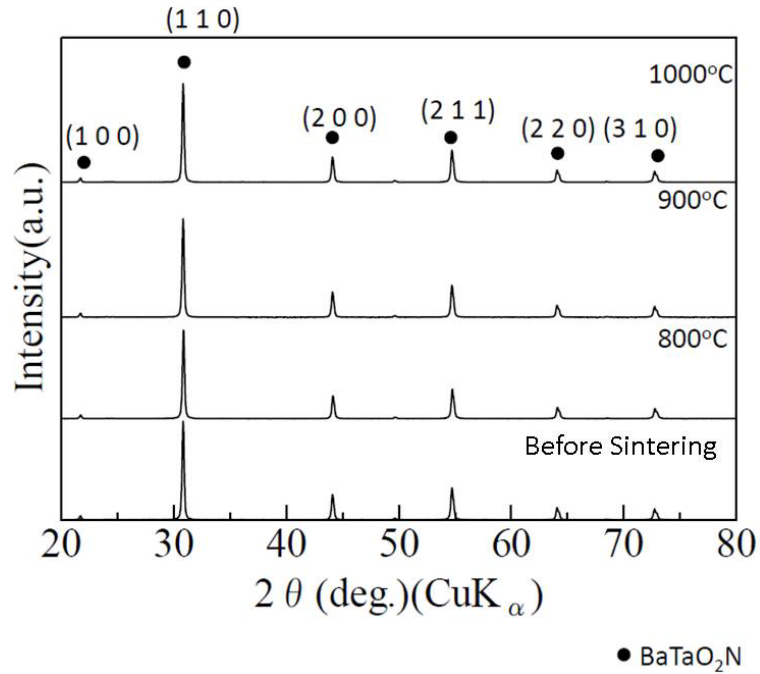


**Figure 4.3.2.3c:** Diffraction data of spark plasma sintered BaTaO<sub>2</sub>N by SPS.

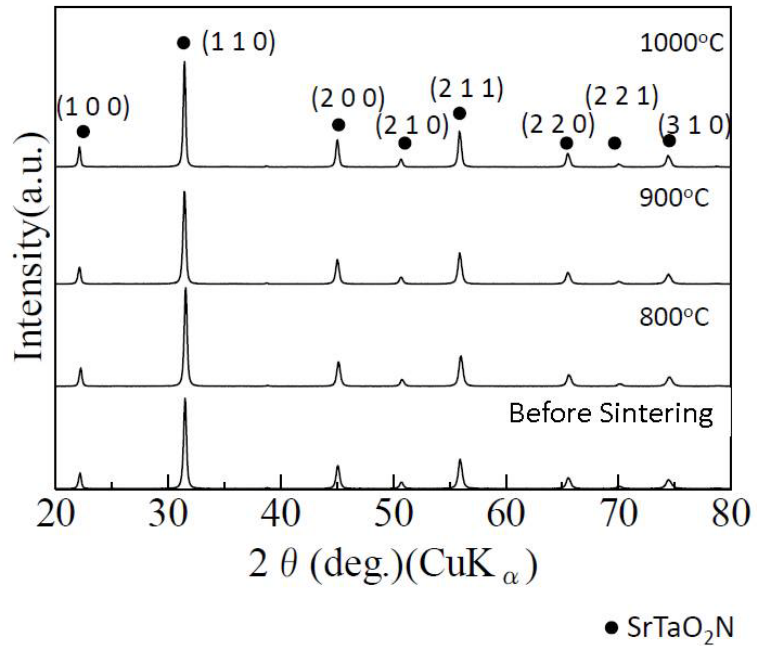


**Figure 4.3.2.3d:** Diffraction data of spark plasma sintered SrTaO<sub>2</sub>N by SPS.



**Figure 4.3.2.3e:** Visual appearance of spark plasma sintered BaTaO<sub>2</sub>N and SrTaO<sub>2</sub>N pellets.

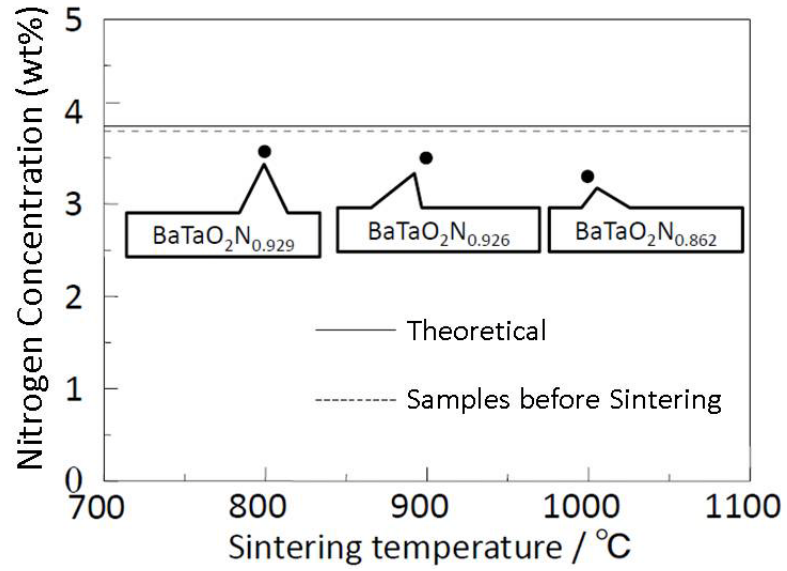


**Figure 4.3.2.3f** Nitrogen content of spark plasma sintered BaTaO<sub>2</sub>N derived from LECO hot-gas extraction analysis.

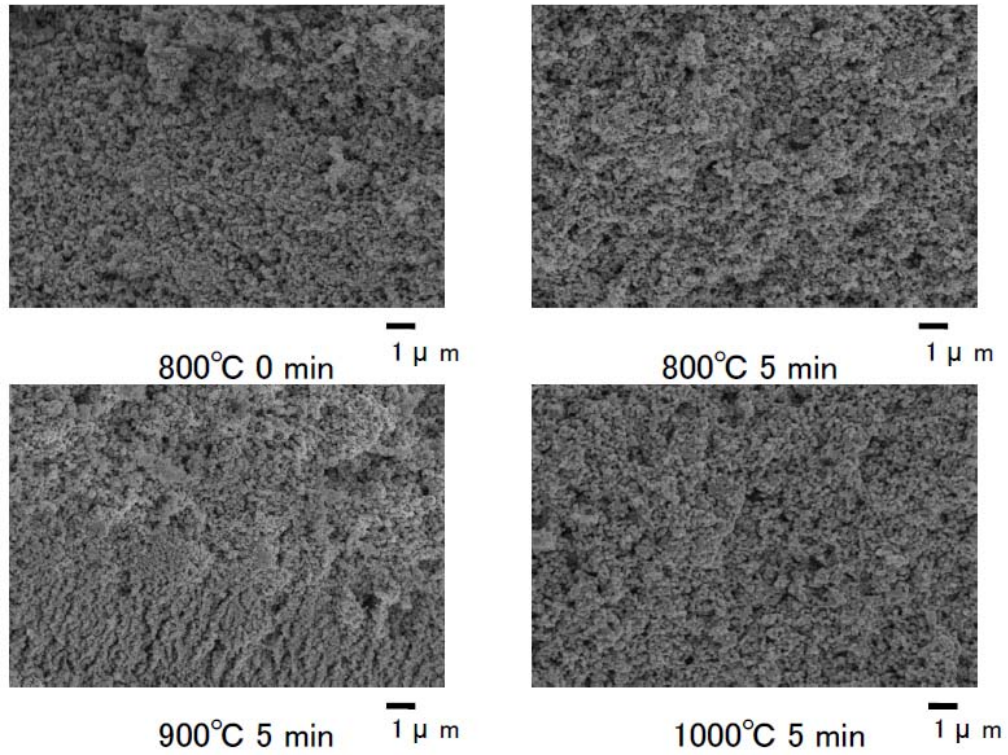


**Figure 4.3.2.3g** Microstructure of spark plasma sintered BaTaO<sub>2</sub>N.

#### 4.4 CONCLUSION

SrTaO<sub>2</sub>N and BaTaO<sub>2</sub>N compounds indicate loss of nitrogen under inert atmospheres at ~950°C (sec. 4.3.1.1). No significant densification was observed below this temperature (sec. 4.3.2.1). Therefore, gas overpressure (sec. 4.3.2.2) and spark plasma sintering (SPS-sec. 4.3.2.3) were investigated as means for increasing stability while decreasing densification temperature and sintering time. An increase in stability was observed with increasing mechanical gas pressure (argon) or chemical pressure (nitrogen) up to ~1400°C. However, densification was minimal. After SPS sintering (at 1000°C, 5 minutes, nitrogen atmosphere), a reduction in nitrogen content was observed (~14% loss of nitrogen) with minimal densification. Attempts to SPS sinter in regions of stability (axial pressures of ~70MPa, at 800 or 900°C) did not produce increases in densification. Further work will investigate wet chemistry and thin films to lower densification temperatures.

## 5 WET CHEMISTRY TACTICS

### 5.1 INTRODUCTION

#### 5.1.1 Motivation

Previous work showed material instabilities at high temperatures caused difficulties in forming dense ceramic. Therefore, wet chemistry processing was considered as a means to lower the ceramic preparation temperature through formation of oxynitride thin films. This leads to the scope of the current chapter: a wet chemistry process for thin film production. The tactics are based on literature review (sec. 5.2) and preliminary experiments (sec. 5.4).

#### 5.1.2 Literature Review

##### 5.1.2.1 Wet Chemistry Overview and Selection

Wet chemistry processing involves creation of a homogeneous solution of cation species, referred to as a sol. The sol then condenses (typically through hydrolysis and condensation reactions); forming a solid phase network, i.e. gel. Gelation provides retention of chemical homogeneity and film. After removal of the organic matrix at low temperatures, the residual metal-oxygen network has limited crystallinity and high surface area, and therefore high reactivity. A final higher temperature treatment promotes crystallization and densification. In addition to lower processing temperatures, wet chemistry provides much greater compositional homogeneity. The component ions in the solution mix at a  $\sim 0.5\text{nm}$  scale compared to  $\sim 10\mu\text{m}$  particles with the conventional ceramic route.<sup>44</sup>

Schwartz et al. divided wet chemistry tactics for synthesizing perovskite oxide thin films into four main categories as distinguished by solution properties and processing

characteristics (precursors, reactivity, extent of chemical interaction, pyrolysis behavior, etc.)<sup>45</sup>:

- 1) Sol-gel with 2-methoxyethanol
- 2) Metallo-organic deposition (MOD) with long-chain complexes
- 3) Hybrid with short-chain complexes
- 4) *In situ* polymerization between hydrocarboxylic acids and glycols (Pechini)<sup>46</sup>

The following paragraphs review each tactic to provide insight into the chosen schemes for investigation. Although each of these has advantages, the first two were deemed undesirable. Sol-gel will not be examined because of complex processing and toxicity of 2-methoxyethanol. MOD processes will not be studied, since limited chemical interactions regularly create phase separated products.

#### **5.1.2.4 Hybrid**

Hybrid processes rely on molecular modification of precursor reagents through reaction with chelating ligands. Therefore, unlike sol-gel, precursors utilize both alkoxide and chelating ligands. Chelating results in less hydrolysis sensitive compounds. Typical chelating ligands are short-chain carboxylates, such as acetate or propionate ligands. Others have used alkanolamines (such as diethanolamine or triethanolamine) dissolved in alcohol or acetylacetonate (AcAc) additions to the carboxylate-modified sol.

Hybrid processing involves simple dissolution of reagents in a solvent, such as acetic acid, in the desired ratio. This offers the advantage of relatively straightforward solution synthesis, compared to the sol-gel process, although reaction complexity is still significant: chelation, hydrolysis, condensation, and esterification.

### 5.1.2.5 Pechini

The Pechini method is based on polymerization of glycols with metal citrates.<sup>47,48</sup> *In situ* polymerization retains metallic homogeneity and prevents precipitation. Typical processing first involves formation of metal complexes through reaction with a multifunctional hydro-carboxylic acid, such as citric acid, tartaric or glycolic acids. The higher stability of citric acid makes it a common choice. Glycol groups, such as ethylene glycol (EG), are then introduced followed by a slight increase in temperature (~80 to 120°C). This promotes formation of an organic ester with the hydro-carboxylic acid, causing gelation of the structure and retention of compositional homogeneity. Disadvantages of this scheme are de-wetting problems during thin film deposition and high solvent evaporation temperatures which typically entrap organics within the precursor matrix.

### 5.1.3 Work Plan

Wet chemistry tactics will be investigated to form oxynitride films suitable for electrical property measurements. Multiple variations of the hybrid and Pechini methods were examined prior to selection of a final method. For film production, the set of assessment criteria for the final method are shown. (**Table VII**)

**Table VII.** Assessment Criteria for Dowselecting the Final Wet Chemistry Route

Process	Assessment Criteria
1) Creation of Sol	1a) High sol stability 1b) High reagent solubility
2) Deposition (onto substrate)	2a) Good substrate wettability
3) Gelation and drying	3a) Elimination of excess solvent 3b) Retention of compositional uniformity (no precipitation)
4) Pyrolysis	4a) Low organic burnout temperature 4b) No metallic component volatilization or segregation
5) Crystallization and Densification	5a) High density 5b) No phase segregation 5c) Creation of desired phase

## 5.4 EXPERIMENTAL

### 5.4.1 Hybrid Synthesis Route

Five types of modifying agents were used, carboxylates (acetate and propionate),  $\beta$ -diketonates (acetylacetonate) and alkanolamines (diethanolamine or triethanolamine). For the carboxylic sols, the solvent (either acetic acid or propionic acid) was first heated to  $\sim 80^\circ\text{C}$ , followed by addition of tantalum isopropoxide ( $\sim 10$ min). After dissolution, strontium acetate or strontium propionate was added until a transparent sol was obtained (30min). (**Figure 5.4.1a**) For the  $\beta$ -diketone-modified sol, AcAc was added in a molar ratio of 1Ta:2AcAc into the carboxylic sol, prior to dissolution of the strontium precursor. (**Figure 5.4.1a**) For alkanolamine-modified sols, tantalum isopropoxide was dissolved in heated methanol, followed by addition of the alkanolamine precursor (diethanolamine or triethanolamine) and then strontium nitrate. (**Figure 5.4.1b**) The

molar ratios of diethanolamine and triethanolamine to metal cations were 20:1 and 10:1, respectively.

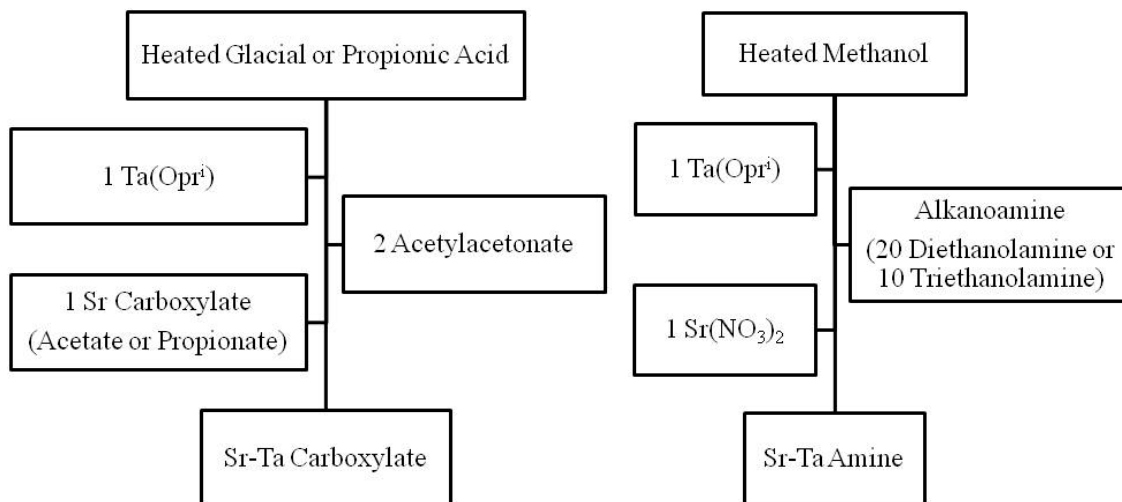


**Figure 5.4.1a:** Procedures for creating carboxylate and  $\beta$ -diketonate sols (left) as well as alkanolamine sols (right).

### 5.4.2 Pechini Sol Synthesis Route

The sol process is schematically shown in **figure 5.4.2a**. Tantalum isopropoxide is dissolved in heated ( $\sim 90^\circ\text{C}$ ) methanol-ethylene glycol ( $\sim 20\text{min}$ ). Citric acid is then added ( $\sim 1\text{hr.}$ ). After dissolution, strontium carbonate is added ( $\sim 12\text{hrs}$ ). The resulting clear sol is further diluted with ethylene glycol (4 moles ethylene glycol to 1 mole citric acid) followed by slow, dropwise addition of ethylenediamine until a pH of 7-9. The pH change results in a highly viscous, yellow sol.

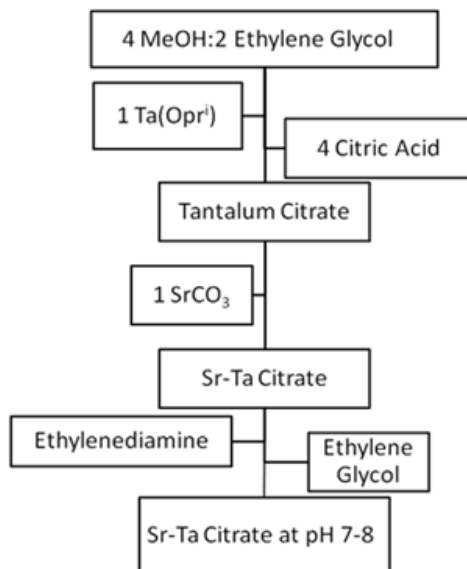


**Figure 5.4.2a:** Procedure for creating strontium-tantalum citrate sol.

### 5.4.3 XRD

Samples were run on a D5000 Siemens Diffractometer with a  $\text{Cu}_{K\alpha}$  radiation source set at 40keV and 30mA. Data was collected over the angular range of  $20^\circ < 2\theta < 100^\circ$  stepping at  $0.03^\circ$  with count times of 4 seconds per step.

### 5.4.4 TGA-DTA

Samples were run on a TA instrument dual beam system. Dried alumina powder was used as a reference and as a calibration for the TGA signal. A constant air flow of 100ml/min was purged over the sample during treatment ( $10^\circ\text{C}/\text{min}$  to  $1200^\circ\text{C}$ ).

## 5.5 RESULTS AND DISCUSSION

### 5.5.1 Creation of Sol

Optimal sol characteristics are high precursor solubility and high stability from hydrolysis or other aging processes. Low stability makes carboxylic sols the least desirable route during sol preparation. Carboxylic sols (acetate, propionate) showed

precipitation after only ~2 weeks. Low stability is attributed to reaction of the precursor water formed *in situ* from esterification of alcohol byproducts (from the alkoxide precursor) with the acid solvent. Pechini,  $\beta$ -diketone, and alkanolamine (diethanolamine and triethanolamine) sols were stable for longer periods. All sols had high solubility in the solvent. An added benefit of all the sol preparation schemes is use of one mixing vessel, minimizing the chance of cationic component loss (from transferring).

### 5.5.2 Gelation and Drying

Goals during gelation are retention of compositional homogeneity (no precipitation) and removal of excess solvent to limit entrapment of residual organics during high temperature processing. For carboxylic and  $\beta$ -diketone sols, drying had to be performed rapidly. Otherwise, phase separated products were observed in XRD after higher temperature treatments. For alkanolamine sols, an unidentifiable phase in XRD formed after drying independent of the procedure.

A 2-step drying procedure was found to be of utmost importance for creation of phase pure products during Pechini processing. Without the initial low temperature gelation at 100-120°C, a visible precipitate was observed and undesirable cation stoichiometric oxides formed after higher temperature treatments,  $\text{Sr}_5\text{Ta}_4\text{O}_{15}$ . (**Figure 5.5.2a**) Low temperatures (<120°C) promote polyesterification and evaporation of water byproducts prior to solvent (ethylene glycol) evaporation. At this stage, viscosity of the sol greatly increased, presumably locking metallic ions into a polymeric, gel network and retaining homogeneity. The heat was then raised to ~200°C to evaporate excess ethylene glycol. Except for alkanolamine sols, all precursors had desirable gelation and drying properties, since precipitation was eliminated and excess solvent could be removed.

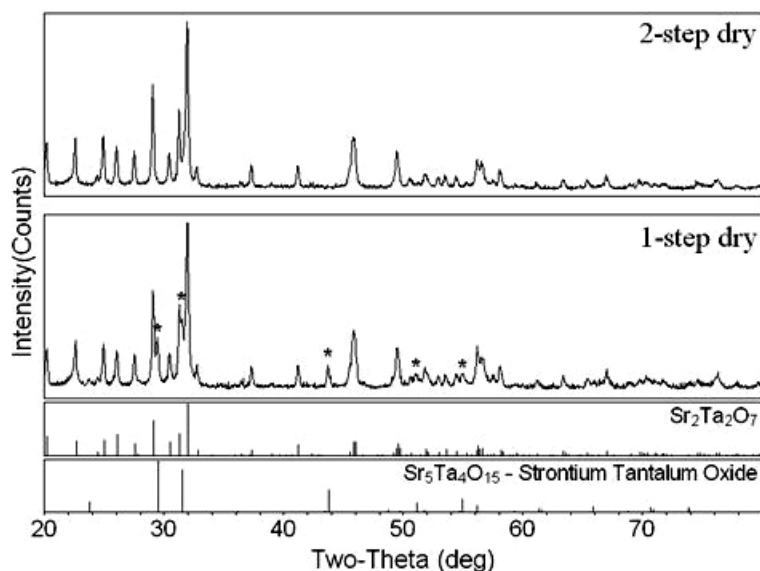


**Figure 5.5.2a:** Creation of non-stoichiometric oxides in the Pechini precursor after 1000°C air crystallization for 1 hour after varying gelation-drying conditions (\* =  $\text{Sr}_5\text{Ta}_4\text{O}_{15}$  minor phase).

### 5.5.3 Pyrolysis

Goals for proper pyrolysis are complete removal of organics (w/o loss of cationic components) and minimal crystallization, retaining a high degree of amorphous and reactive character for the corresponding ammonolysis reaction. This requires low pyrolysis temperatures and minimization of heat evolved. Large excess energy associated with combustion can result in unwanted partial sintering, grain growth, crystallization and possible phase segregation. For example, organic burnoff in air compared to oxygen at 400 for  $\text{LiNiO}_3$  resulted in an amorphous and crystalline precursor, respectively. An oxygen atmosphere enhanced the rate of heat evolved from combustion, providing greater internal temperatures throughout the precursor. To establish an appropriate pyrolysis temperature, TGA-DTA was used.

Weight loss for carboxylate,  $\beta$ -diketone and alkanolamine precursors occurred between 200°C-500°C with a corresponding higher temperature weight loss at 700°C - 850°C for carboxylate/diketone precursors and at 850°C-950°C for alkanolamine precursors. (Figures 5.5.3a & b) The Pechini precursors had no residual organics after 650°C. (Figure 5.5.3c) As mentioned earlier, organics need to be removed with minimal oxide crystallization. Therefore, the required pyrolysis treatment for each precursor will be compared to their corresponding crystallization behavior in air (sec. 5.5.4)

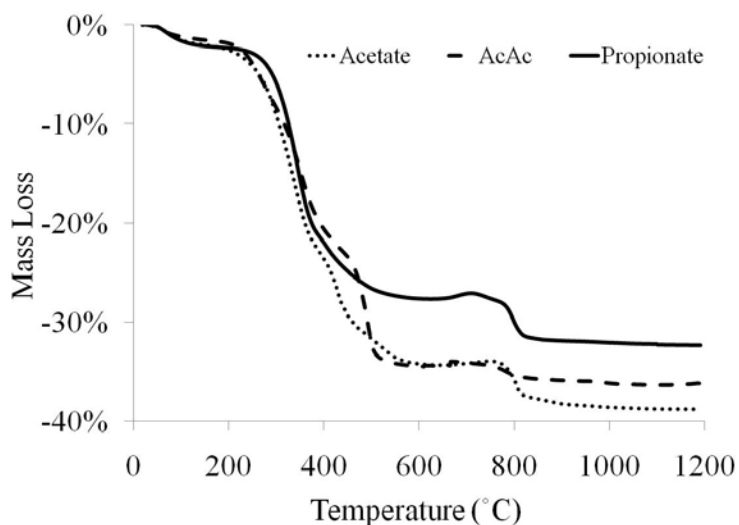


**Figure 5.5.3a** Pyrolysis behavior of the carboxylate and  $\beta$ -diketone precursors in air.

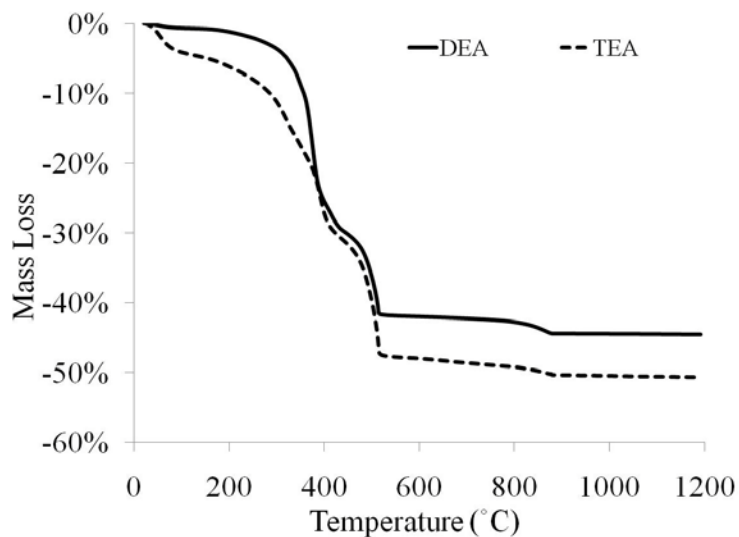


**Figure 5.5.3b** Pyrolysis behavior of the alkanolamine precursors in air.

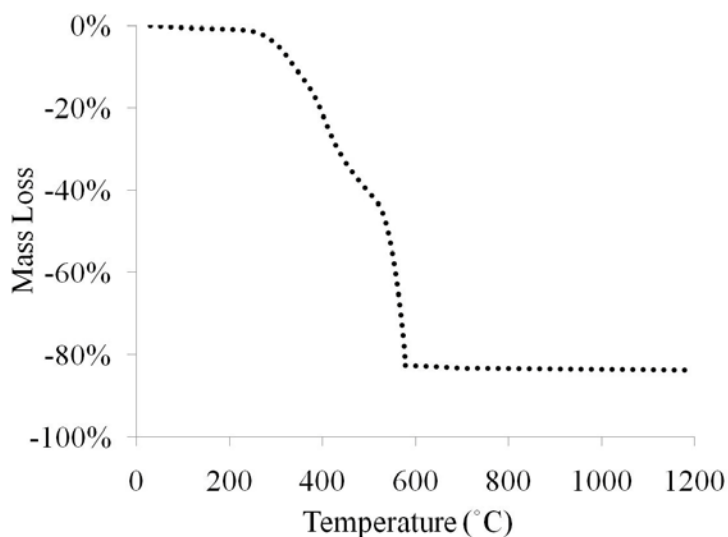


**Figure 5.5.3c** Pyrolysis behavior of the Pechini precursor in air.

#### 5.5.4 Crystallization Behavior

Figures 5.5.4a-c show crystallization behavior in air for representative precursors via XRD. Carboxylate,  $\beta$ -diketone and Pechini precursors had an amorphous structure at 600°C. Upon heating to 800°C, an intermediate perovskite phase crystallizes. A further increase to 1000°C results in pyrochlore formation. Alkanolamine precursors showed

unidentifiable minor phases, indicating precipitation. Therefore, alkanolamine sols will not be investigated further.

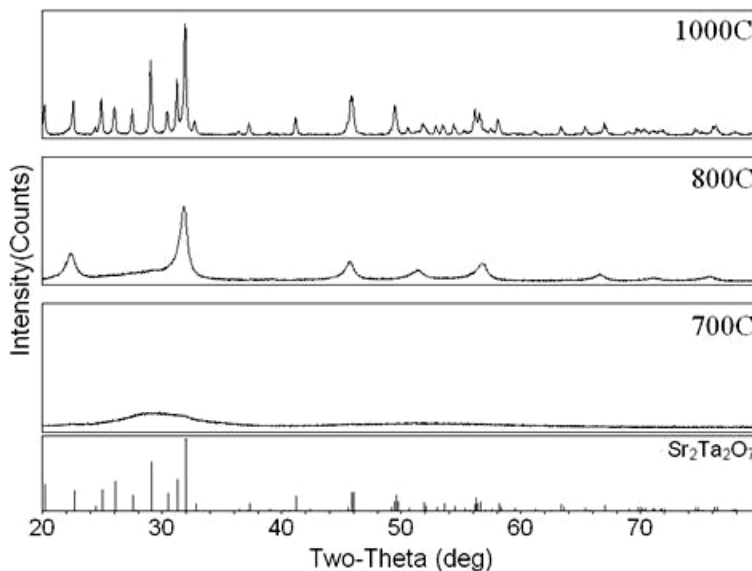


**Figure 5.5.4a:** Crystallization behavior of the acetate precursor in air at various temperatures for 1hr.

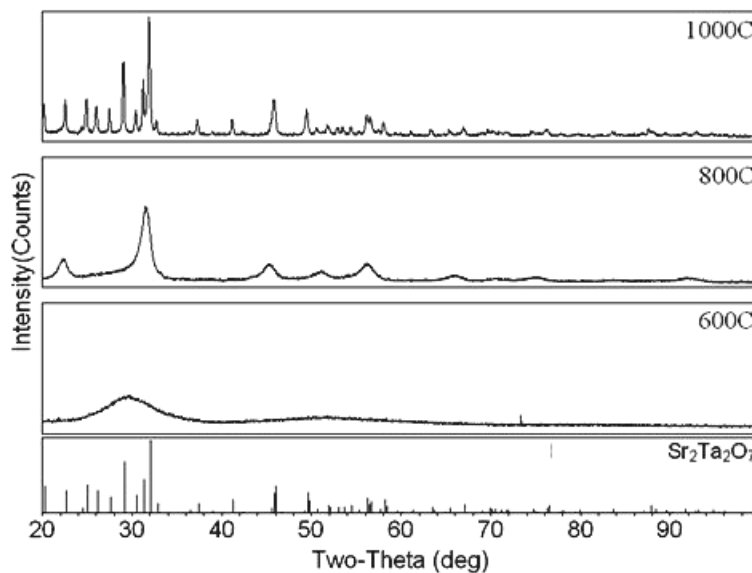


**Figure 5.5.4b:** Crystallization behavior of the Pechini precursor in air at various temperatures for 1hr.

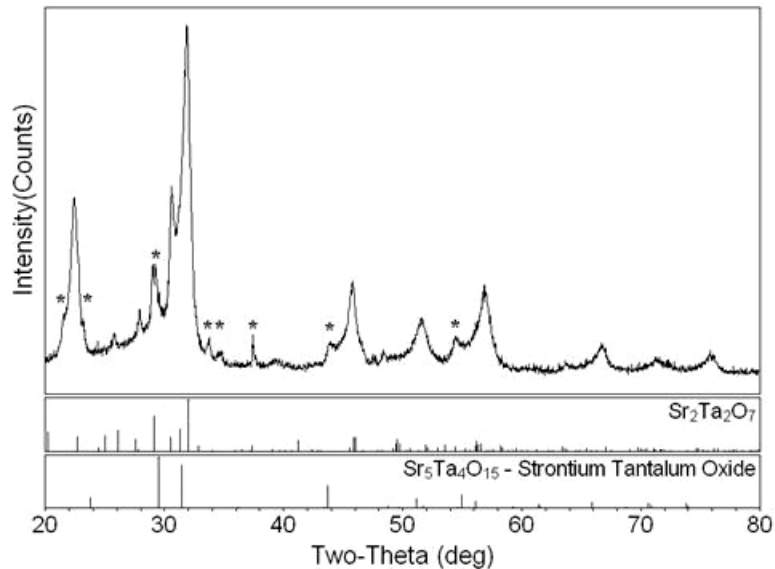


**Figure 5.5.4c:** Crystallization products of the alkanamine precursor in air after 800°C for 1hr.

An intermediate oxide has been observed in thin film work.<sup>49,50</sup> Cell refinement indicated a strontium deficiency,  $\text{Sr}_{0.75}\text{TaO}_3$ , yet no residual strontium impurities were identified via XRD. Composition was determined to be an equal molar ratio tantalum to strontium of 1 to 1 via ICP. EPR did not indicate a tantalum reduction. Raman spectroscopy showed no signs of ionic carbonates, providing evidence against formation of an intermediate carbonate complex or strontium carbonate. Therefore, it is proposed that the true structure was an equally cation defective phase,  $\text{Sr}_{0.85}\text{Ta}_{0.85}\text{O}_3$ , that could not be clearly refined (via XRD) from possible interaction of films with the substrate.

In the current work, XRD refinement of powder of the intermediate oxide indicated a strontium deficiency,  $\text{Sr}_{0.70}\text{TaO}_3$ . However, no strontium-rich minor phase, e.g. SrO or  $\text{SrCO}_3$ , was observed in XRD. **(Figure 5.5.4d)** Comparing XPS spectra to  $\text{Sr}_2\text{Ta}_2\text{O}_7$  confirmed a  $\text{Ta}^{+5}$  valence state bound to oxygen. **(Figure 5.5.4e)** Therefore, the cation-defect model is supported.

Analyzing powder of the intermediate oxide presented a similar stoichiometry,  $\text{Sr}_{0.70}\text{TaO}_3$ , as previous literature with films. This contradicts the assumption, where film-substrate interactions inhibit accurate assessment of site-occupancy in XRD. However, a 0.3 strontium vacancy concentration provides a  $\text{Sr}_{0.70}\text{TaO}_{3.2}$  composition and a 6.7% oxygen excess. Furthermore, no strontium-rich minor phases were observed. An alternative scenario is placement of strontium on the B-site, providing strontium vacancies ( $V_{\text{Sr}}''$ ) and strontium-tantalum site mixing ( $\text{Sr}_{\text{Ta}}'''$ ). This results in an experimentally-observed composition of  $\text{Sr}_{0.70}(\text{Sr}_{0.15},\text{Ta}_{0.85})\text{O}_{2.95}$  and an oxygen deficiency of only 1.7%. Similar results have been observed with strontium-doping in  $\text{Sr}(\text{Sr},\text{Nb})\text{O}_x\text{N}_y$  and calcium-doping in  $\text{Ba}(\text{Ca},\text{Ti})\text{O}_x$ .<sup>31</sup>

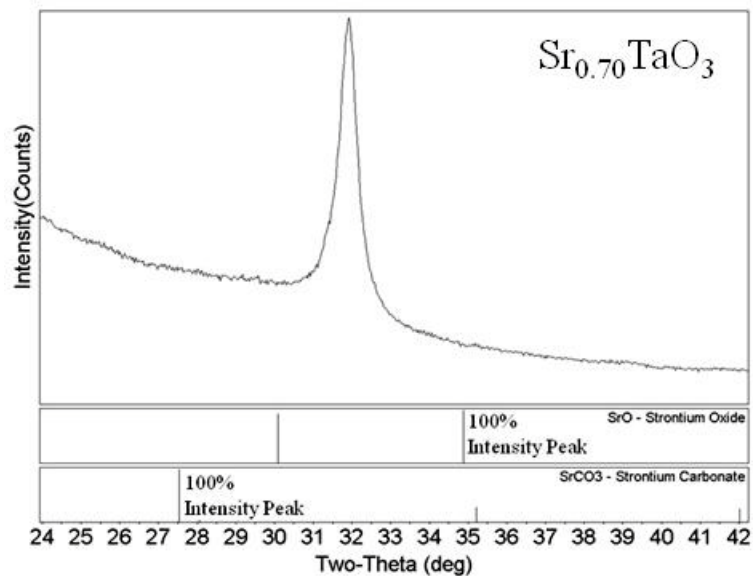


**Figure 5.5.4c:** Overlay of standard SrO and SrCO<sub>3</sub> on the experimental Sr<sub>0.7</sub>TaO<sub>3</sub> diffraction pattern (800°C, 1hr, air).

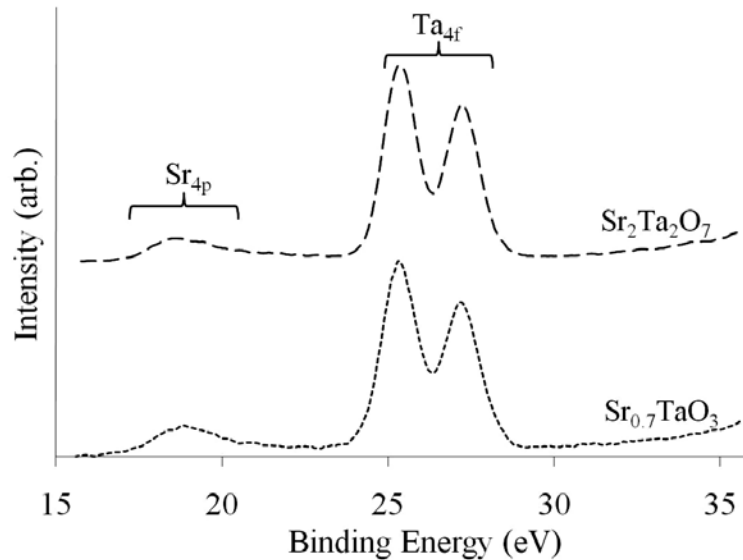


**Figure 5.5.4c:** Comparison of  $\text{Ta}_{4f}$  spectra in  $\text{Sr}_{0.7}\text{TaO}_3$  (800°C, 1hr, air) and  $\text{SrTaO}_{3.5}$  (1000°C, 48hr, air)

## 5.6 CONCLUSION

Carboxylate and  $\beta$ -diketone precursors require high pyrolysis temperatures, promoting partial crystallization (sec. 5.5.3 and 5.5.4). In addition, carboxylic sols have low stability (sec. 5.5.1). Therefore, the Pechini process has the greatest promise for oxynitride film production (chapter 6).

## 6 PEROVSKITE OXYNITRIDE FILM FORMATION

### 6.1 INTRODUCTION

#### 6.1.1 Motivation

Perovskite oxynitrides have exciting application in many fields. Unfortunately, perovskite oxynitrides have low thermal stability, inhibiting formation of dense ceramic and property measurements (refer to chapter 4).<sup>7</sup> Thin films from a wet chemistry precursor are an attractive alternative to create dense oxynitride material (ammonolysis). Therefore, control over  $\text{NH}_3$  decomposition will be employed to fabricate phase-pure, dense oxynitride films for application as thin-film dielectrics. Prior to application, processing needs to be well-defined.

#### 6.1.2 Literature Review

Fabrication of oxide and oxynitride films has minimal procedural differences during sol preparation, drying, thin film application and pyrolysis. After pyrolysis oxide films undergo two structural changes: crystallization and densification.<sup>45</sup> A composition change is not typically required, such as further oxidation. Oxynitride film growth requires an additional chemistry change via a gas-solid reaction with  $\text{NH}_3$  (reduction/nitridation). Hence, producing phase-pure oxynitride films requires control over anion composition.

This has proven to be interesting, since previous work has suggested the perovskite structure can have variable anion composition. Marchand et al produced  $\text{LaTiO}_x\text{N}_y$  films via reactive sputtering with nitrogen levels between  $y = 0-0.75$  (ideal is 1) and only identified a single perovskite phase via XRD.<sup>51,52</sup> Ebbinghaus et al observed similar results in pulse laser deposited  $\text{LaTiO}_x\text{N}_y$  films with nitrogen contents ranging

between  $y = 0.47-0.72$ .<sup>53</sup> Currently, the structure and defect mechanism has not been clarified. Additionally, results show difficulties in producing ideal stoichiometry. Proper control over  $\text{NH}_3$  decomposition and reaction conditions will be used to tailor anion chemistry, providing an in-depth examination and production of phase-pure films (refer to chapters 1 & 2).

Additionally, competition between film formation and the anion-exchange reaction can create two competing scenarios:

1. Formation of oxynitride from an amorphous precursor, followed by densification
2. Densification of an oxide followed by oxynitride formation

It is envisioned (2) could potentially cause compositional variation throughout the film thickness. Since, with a dense film, atmosphere exposure in inner regions is limited. For example, Aguiar et al ammonolyzed a dense, well crystallized oxide film and observed a reduction in nitrogen content as a function of depth.<sup>54</sup> Experimentally, each scenario is examined by changing the oxynitride reaction rate. For example, high  $\text{NH}_3$  flow velocity promotes formation of the oxynitride prior to densification (1). Where, low flows result in oxide densification followed by oxynitride formation (2).

Alternatively, temperature can be modified. However, below 900 the rate of oxynitride synthesis is low and above 1000 phase stability becomes a concern.<sup>19</sup> This produces a minimal synthesis temperature regime (900-1000°C) and hence, limits the ability to manipulate film properties as a function of temperature. Furthermore, low temperatures reduce grain size.<sup>4</sup> If perovskite oxynitrides are ferroelectric, then large grains (>100nm) are desired to provide a domain structure and high permittivity. The ammonolysis temperature was kept at 950°C.

### 6.1.3 Work Plan

Oxynitride films will be created via the Pechini method, while systematically changing flow velocity and reaction time. This study achieves three processing objectives:

(O1) establish reaction conditions for fabricating phase-pure films

(O2) elucidate on the possible perovskite solid-solution ( $\text{SrTaO}_x\text{N}_y$ )

To meet current objectives, O1-O2, requires means for assessing phase purity. This is realized through criteria important in microelectronics and capacitor applications, C1-C5. Each criterion is strategically investigated with a chosen characterization tactic(s). Throughout characterization, results are compared to  $\text{SrTaO}_2\text{N}$  powders considered phase pure (via XRD and LECO, hot-gas extraction analysis in chapter 3).

C1.) Single perovskite phase with correct cell volume in sec. 3.1 (XRD, XPS)

C2.) Correct anion composition in sec. 3.2 (WDS, XPS)

C3.) Homogenous phase (laterally and through film thickness) in sec. 3.3 (EDS, XPS)

C4.) Desired cation valence states in sec. 3.4 (XPS)

C5.) Smooth film morphology and high density in sec. 3.5 (ESEM)

## 6.2 EXPERIMENTAL

### 6.2.1 Thin film deposition

The sol preparation scheme is described in section 5.4.2. For thin film application, the sol was diluted with a methanol-ethylenediamine mixture (1 part sol to 1 part MeOH/EDA (by volume), MeOH/EDA solution with pH of 7-9) and subsequently filtered with a  $0.45\mu\text{m}$  syringe to remove contamination. A dynamic spin coat provided the best film coverage, compared to static. The sol was pipetted onto a polished 99.6% alumina substrate already spinning at 2,000-4,000 rpm, followed by further increase to

6,000rpm for 35sec. Films were then dried at 100-120°C for 8-12hrs to evaporate methanol and promote polymerization. The hot plate was then turned up to 200-220°C for 1-2hrs to evaporate excess ethylene glycol. The dried, brown films were heated to remove organics through a temperature program as follows: 1) 5°C/min to 450°C, 2) 2C/min between 450°C and 600°C and 3) hold at 600°C for 1hr. The procedure was then repeated until the desired thickness, 7 layers. After pyrolysis films were uniform with a white appearance.

### 6.2.2 Ammonolysis Reaction

The ammonolysis temperature was fixed at 950C and sample position at 2” (refer to chapter 1 & 2 for a more detailed explanation). Films were subjected to different ammonia flow velocities and reaction times. (**Table 1**) Each sample is labeled for reference throughout discussion in the format S. X-Y. X stands for flow velocity (cm/min) and Y for reaction time (hrs.). SrTaO<sub>2</sub>N powders were synthesized via a solid-state reaction (refer to section 3.2.1).

**Table VIII.** Processing Conditions Investigated During SrTaO<sub>2</sub>N Film Production

Reaction Time (hrs)	Flow Velocity (cm/min)						
	1	2	4	5	6	18	54
0.5 or 1	S. 1-0.5	S. 2-1					
5	S. 1-5	S. 2-5	S. 4-5	S. 5-5	S. 6-5	S. 18-5	S. 54-5
20	S. 1-20	S. 2-0					

### 6.2.3 XRD

Samples were run on a D5000 Siemens Diffractometer with a Cu<sub>Kα</sub> radiation source set at 40kev and 30mA. Data was collected over the angular range of 20° < 2θ < 80°

stepping at  $0.03^\circ$  with count times of 15 seconds per step. Lattice parameters were acquired through structural refinements using TOPAS software.

#### **6.2.4 ESEM-EDS**

Microstructures were imaged with a Quanta 200F (Field Emission) Environmental SEM/EDAX Genesis system at a 20kV accelerating potential. For EDS, scans were taken over an interaction area of  $\sim 2 \times 2 \text{ mm}$ . Overlap of strontium and tantalum fluorescence peaks in EDS limit accurate atomic assessment of these elements, therefore are not reported. To eliminate substrate signal (Al and O), the accelerating potential was reduced to 10kV.

#### **6.2.5 WDS**

Samples were run on a JEOL-JXA 8200 electron microprobe (WDS) at an accelerating voltage of 15kV and a probe current of  $3 \times 10^{-8} \text{ A}$ . For each film 8 locations were measured and results compiled. A calibration curve correlating nitrogen peak area to nitrogen content was obtained using  $\text{Ta}_3\text{N}_5$ ,  $\text{SrTaO}_{3.5}$  and  $\text{SrTaO}_2\text{N}$  powders and mixtures thereof. Each powder was mixed in an IPA suspension and applied dropwise to alumina substrates to create a flat surface, limiting topographical variations during analysis. Anion chemistry of  $\text{SrTaO}_2\text{N}$  powders was determined via LECO-hot gas-extraction.

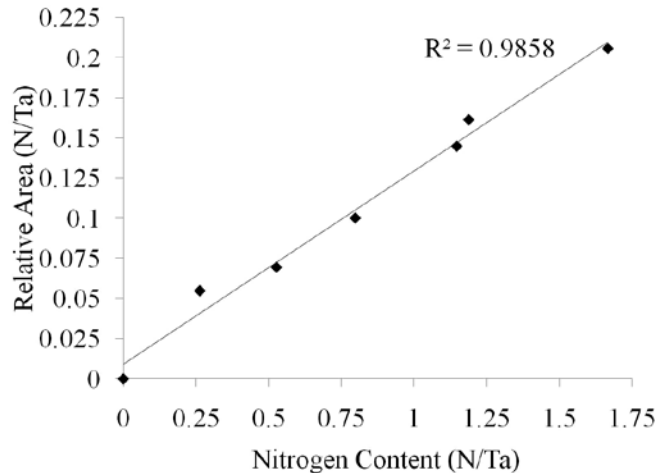


**Figure 6.2.5a** WDS calibration curve correlating relative nitrogen peak area (N/Ta) to nitrogen content.

### 6.2.6 XPS

XPS was performed with a PHI Quantera SXM spectrometer using a monochromated  $Al_{K\alpha}$  radiation source (1486.6eV) operating at 20 watts. The x-ray beam diameter was 100  $\mu$ m. For high resolution spectra, the spectrometer was used in constant pass energy mode at 55eV with an incident angle of 45° relative to the sample plane.

Some  $N_{1s}$  spectra were taken at 26eV pass energy to further improve resolution for qualitative analysis. Charging effects were reduced through use of a low energy electron gun set at 1V and 20 $\mu$ A. The binding energy was calibrated using the  $C_{1s}$  peak associated to an adventitious carbon surface layer at 284.6eV. For the fitting procedure, FWHM values and peak area ratios of spin orbitals were obtained from literature, the NIST database and experimentally derived using  $Ta_2O_5$ ,  $Ta_3N_5$ ,  $SrTaO_{3.5}$  and  $SrTaO_2N$  powders.<sup>20-22</sup> For sputtering, a 3keV  $Ar^+$  source was rastered over an area of 1x1mm. Each cycle was 0.3min in duration. The estimated etch rate for  $SrTaO_2N$  was 20-30nm per cycle, which was determined from the number of cycles required to remove the entire film and the approximate film thickness via SEM.

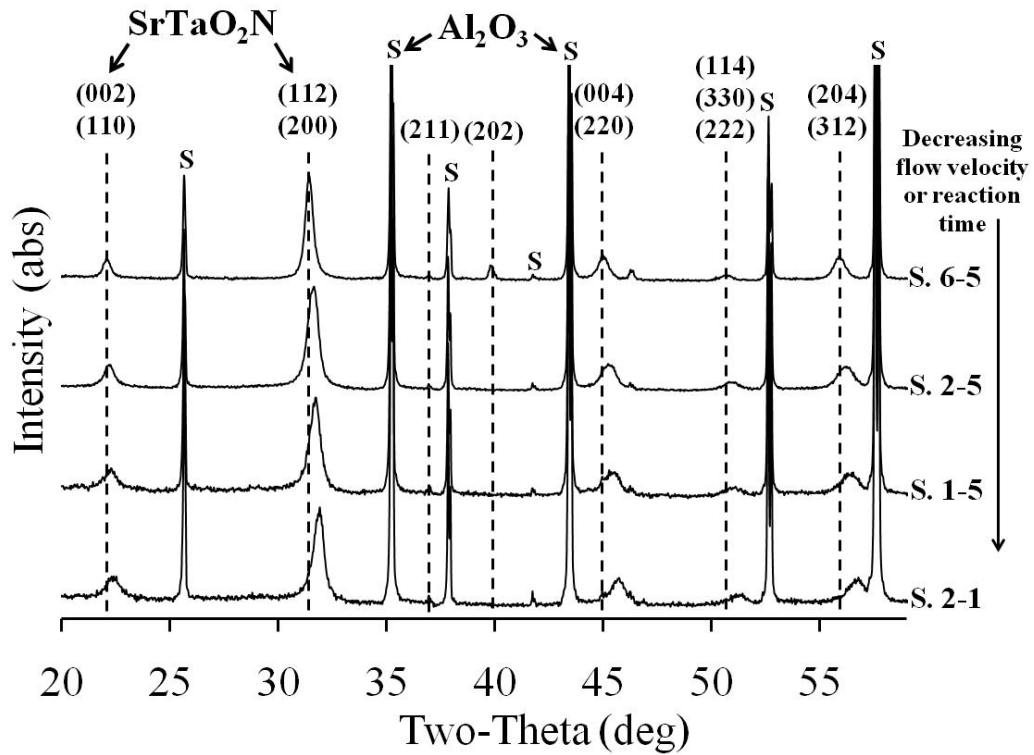
## 6.3 RESULTS

### 6.3.1 Phase Composition and Structure (C1)

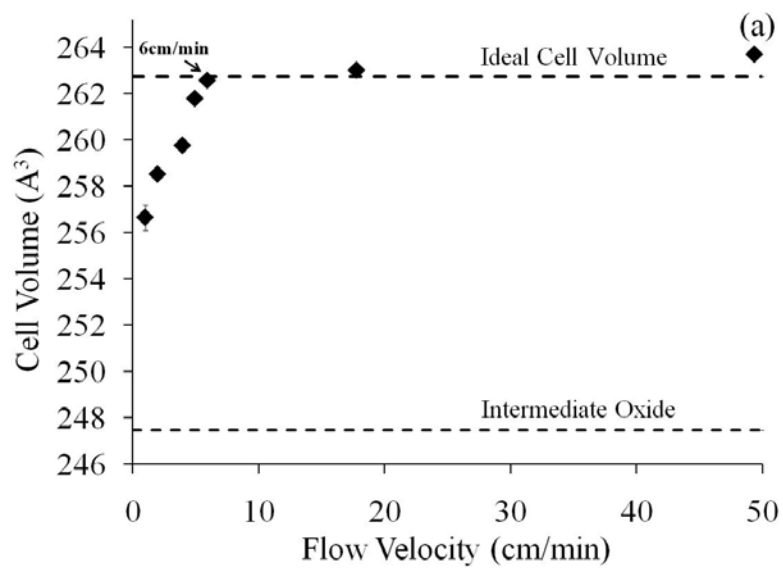
#### 6.3.1.1 XRD Analysis

The intermediate oxide,  $\text{Sr}_{0.75}\text{TaO}_3$ , and oxynitride,  $\text{SrTaO}_2\text{N}$ , both have perovskite structures. Therefore, independent of anion composition, it is possible that only a perovskite phase is detectable in films. However, the oxynitride perovskite has a greater cell volume. This allows the degree of film nitridation to be monitored through examining crystallographic dimensions. Thus, XRD will be used to optimize reaction parameters for producing  $\text{SrTaO}_2\text{N}$  films.

Independent of synthesis conditions, all films show a perovskite structure. **(Figure 6.3.1.1a)** As the  $\text{NH}_3$  flow velocity or reaction time increased, the perovskite cell volume increased. **(Figures 6.3.1.1b-c)** Flow velocities  $\geq 6\text{cm/min}$  ( $950^\circ\text{C}$ , 5hrs) or at  $2\text{cm/min}$  ( $950^\circ\text{C}$ , 20hrs) resulted in the ideal  $\text{SrTaO}_2\text{N}$  cell volume. The cell volume of the intermediate perovskite oxide was obtained from literature ( $69.86 \text{ \AA}^3$  at  $Z=1$ ).<sup>49,50</sup>



**Figure 6.3.1.1a** Diffraction patterns of oxynitride films on an alumina substrate (S) after synthesis under different reaction conditions (dashed lines correspond to SrTaO<sub>2</sub>N diffraction lines<sup>15</sup>).



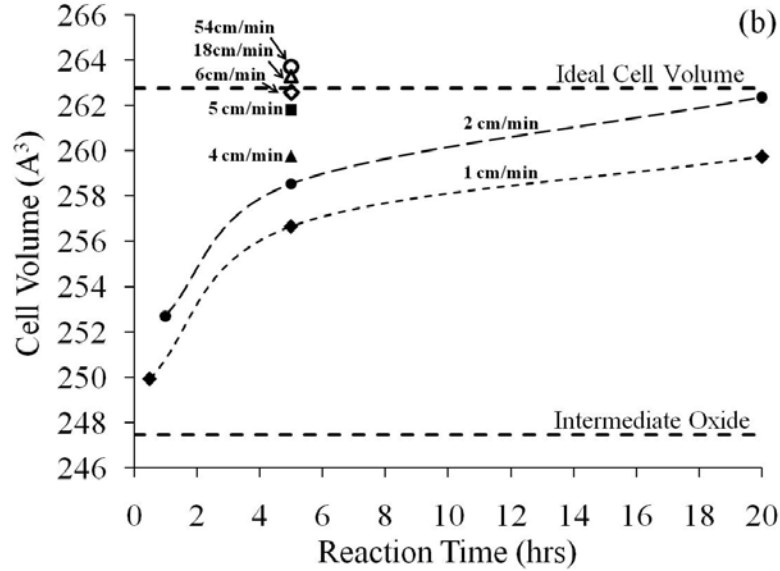


**Figure 6.3.1.1** SrTaO<sub>2</sub>N cell volume of films as a function of flow velocity (950C, 5hrs.) (b) & reaction time (c). Ideal cell volume obtained from previous work (Z=4).

An increase in flow velocity lowered the time required to produce a SrTaO<sub>2</sub>N film. This is consistent with previous work, where higher flow velocities provide greater concentrations of NH<sub>3</sub> and active nitriding species.

### 6.3.1.2 XPS Analysis

XPS was used to examine the N<sub>1s</sub> and O<sub>1s</sub> chemical environment for possible minor phases (below the detectable threshold in XRD) and the process of nitrogen incorporation. For example, besides a lattice exchange, nitrogen can reside as an adsorbed or interstitial species, as well as a nitride minor phase, such as Ta<sub>3</sub>N<sub>5</sub>. Previous work has identified Ta<sub>3</sub>N<sub>5</sub> as a common impurity in BaTaO<sub>2</sub>N powders after high NH<sub>3</sub> flow treatments.

All SrTaO<sub>x</sub>N<sub>y</sub> films and powder indicate N<sub>1s</sub> peaks at ~395.2eV. (**Figure 6.3.1.2a**) For Ta<sub>3</sub>N<sub>5</sub>, the N<sub>1s</sub> peak is located at 396.05eV. These binding energies are typical for lattice entities.<sup>22</sup> Neither powder nor films show an observable peak at 396.05eV and therefore, no detectable Ta<sub>3</sub>N<sub>5</sub> phase.

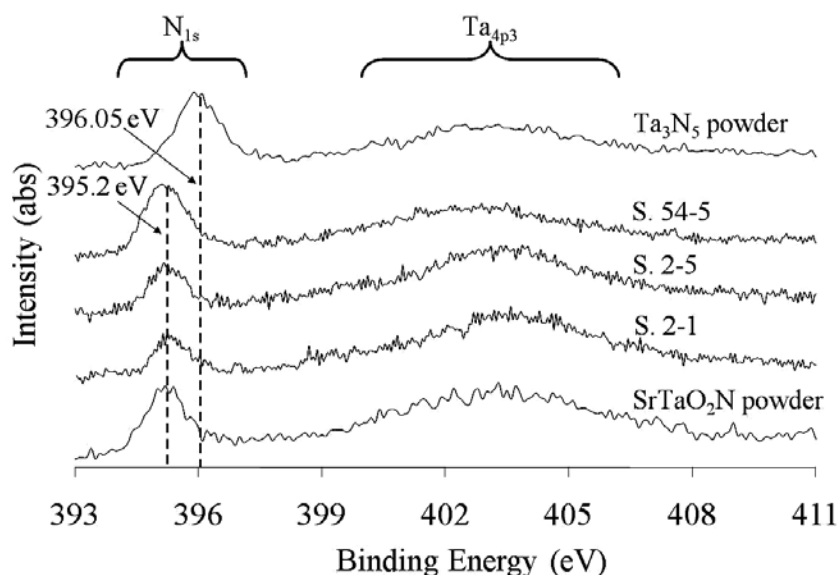


**Figure 6.3.1.2a** Comparison of the N<sub>1s</sub> peak location between a SrTaO<sub>2</sub>N powder, SrTaO<sub>2</sub>N films and Ta<sub>3</sub>N<sub>5</sub> powder at a 26eV constant pass energy and 0.05eV step size.

No additional N<sub>1s</sub> peaks that could be associated with alternative nitrogen species were observed (e.g. adsorbents, interstitial, minor phases). Therefore, results suggest nitrogen is only present in the perovskite anion lattice, supporting XRD observations. However, overlap from the Ta<sub>4p3</sub> peak and the close proximity of the lattice N<sub>1s</sub> peaks of SrTaO<sub>x</sub>N<sub>y</sub> and Ta<sub>3</sub>N<sub>5</sub> may be concealing a minor peak.

All films indicate a similar O<sub>1s</sub> environment and a single lattice state. (**Figure 6.3.1.2b**) Based off literature, the highest binding energy (BE) state (~532.3eV) in the O<sub>1s</sub> spectrum is attributed to adsorbed CO<sub>3</sub><sup>2-</sup> and the middle O<sub>1s</sub> state to OH<sup>-</sup> or O<sup>-</sup>.<sup>55</sup> The anion chemical environments in XPS further suggest all films are single phase.

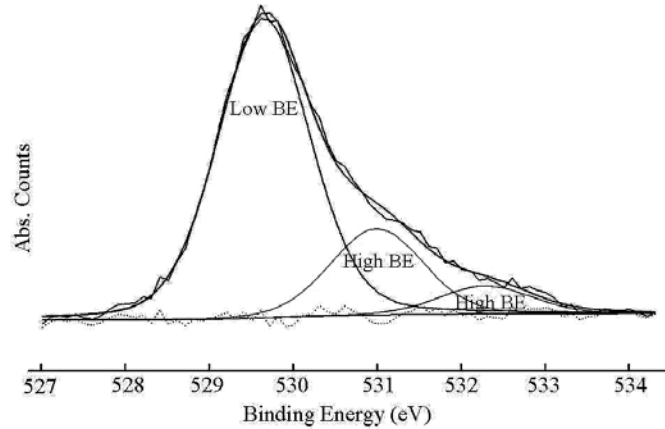


**Figure 6.3.1.2b** Deconvolution of the O<sub>1s</sub> chemical environment.

## 6.3.2 Anion Composition (C2)

### 6.3.2.1 WDS Analysis

To create SrTaO<sub>2</sub>N films requires control over anion composition. Therefore, WDS was used to determine reaction conditions that produce the desired nitrogen level. An increase in flow velocity or reaction time enhanced nitrogen levels in films. A NH<sub>3</sub> flow velocity of 4cm/min (950°C, 5hrs) or 2cm/min (950°C, 20hrs) created films with a nearly ideal nitrogen content (ideal=1). (**Figure 6.3.2.1a & b**) Higher flow  $\geq$ 5cm/min, 950°C, 5hrs) induced excess concentrations (~1.18).

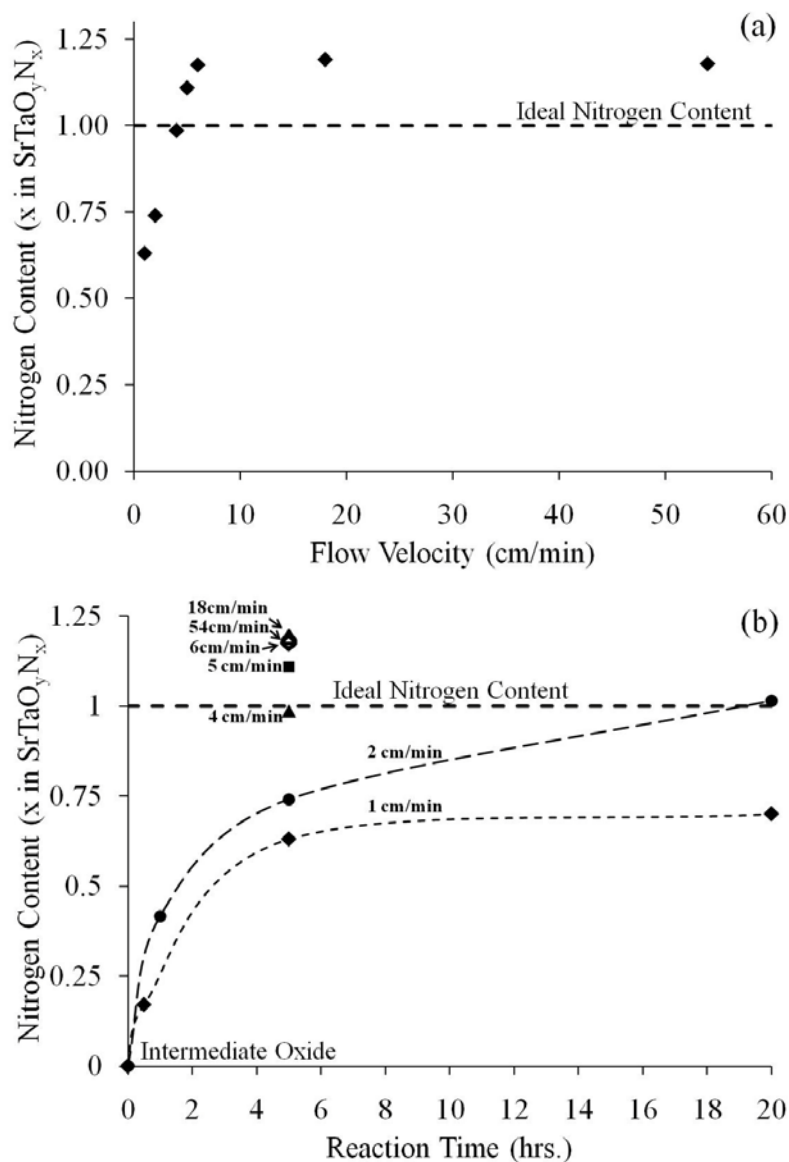


**Figure 6.3.2.1a-b** Nitrogen content (x) in SrTaO<sub>y</sub>N<sub>x</sub> films obtained via WDS as a function of (a) flow velocity (950°C-5hrs) & (b) reaction time. Ideal nitrogen content based on charge balance, SrTaO<sub>2</sub>N.

NH<sub>3</sub> flow velocities  $\geq 6$  cm/min (950°C, 5hrs) or at 2cm/min (950°C, 20hrs) produced films with a perovskite cell volume similar to previous reports.<sup>1,15</sup> However, films showed excess nitrogen content (~1.18). Similar deviation in anion chemistry has been observed in literature. Logvinovich et al. and Kim et al. discuss adsorbents (N1) or a nitride minor phase (N2) as cause for the variation.<sup>1,56</sup> Alternatively to N1 or N2, an

excess replacement of lattice oxygen with nitrogen in the perovskite structure could occur (N3).

Unfortunately, neither mechanism (N1-N3) could be confirmed in present work. A  $Ta_3N_5$  minor phase was not observed with XPS or XRD (N2) and no nitrogen adsorbents were detectable with XPS (N1). However, it is believed films after high  $NH_3$  flow velocities have lattice nitrogen levels similar to  $SrTaO_2N$  powders reported in literature.<sup>1,15</sup> Since, films that contain excess nitrogen ( $\sim 1.18$ ) have a similar color (orange) and perovskite cell volume. Conversely, films with  $\sim 1.00$  nitrogen content (e.g. S. 4-5) had a green color and a lower than expected cell volume (refer to fig. 4).

The effect of anion composition on the perovskite cell volume is shown in **figure 6.3.2.1c**. The cell volume at 0% nitrogen (intermediate perovskite oxide) was obtained from literature ( $69.86 \text{ \AA}^3$  at  $Z=1$ ).<sup>49,50</sup> As nitrogen content increased, the cell volume increased linearly. This volumetric enlargement is consistent with ionic size differences (4 coordinated ionic radii of  $N^{3-}$ ,  $1.46 \text{ \AA}$  and  $O^{2-}$ ,  $1.38 \text{ \AA}$ ).<sup>23</sup>

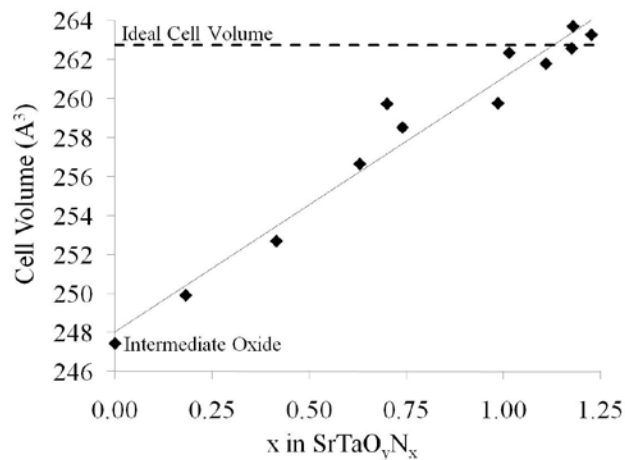


**Figure 6.3.2.1c** Cell volume as a function of WDS-derived nitrogen content for  $SrTaO_xN_y$  films.

### 6.3.2.2 XPS Analysis

It is important to determine the oxygen concentration in films, since reducing conditions during high temperature ammonolysis can induce oxygen deficiencies. With WDS analysis, beam penetration through the film and into the  $\text{Al}_2\text{O}_3$  substrate inhibits accurate assessment. Furthermore, surface contamination (e.g.  $\text{H}_2\text{O}$  or  $\text{CO}_2$ ) adds to the overall oxygen concentration. XPS can eliminate surface contamination via ion sputtering and substrate contribution via a minimal probe depth ( $\sim 10\text{nm}$ ) and thus, was used to evaluate the oxygen concentration in films.

**Figure 6.3.2.2a** shows the  $\text{O}_{1s}/\text{Ta}_{4f}$  peak area as a function of reaction time at different flow velocities (1-54cm/min). The  $\text{Ar}^+$  sputtering treatment was 0.9 min at 3 keV rastered over a 1x1mm area (estimated sputter removal of  $\sim 40\text{-}50\text{nm}$ ). All  $\text{O}_{1s}$  peak areas were normalized to the  $\text{Ta}_{4f}$  peak area. The intermediate oxide  $\text{O}_{1s}/\text{Ta}_{4f}$  peak area was obtained from a film that did not undergo an ammonolysis treatment (only pyrolyzed in air). The  $\text{O}_{1s}/\text{Ta}_{4f}$  peak area for  $\text{SrTaO}_2\text{N}$  was determined through analyzing the proposed reduction in the  $\text{O}_{1s}$  peak area of two oxide films:

- 1.) Non-ammonolyzed film that only experienced pyrolysis at  $600^\circ\text{C}$  (assumed composition of  $1\text{Sr}:1\text{Ta}:3.5\text{O}$ )
- 2.) A film crystallized at  $1000^\circ\text{C}$  for 2hrs in air that showed the pyrochlore structure via XRD (composition of  $\text{Sr}_2\text{Ta}_2\text{O}_7$ , refer to Fig. 2).

The  $\text{O}_{1s}/\text{Ta}_{4f}$  peak area for the non-ammonolyzed and pyrochlore films was 0.441 and 0.449, respectively. After formation of a  $\text{SrTaO}_2\text{N}$  phase, these areas would decrease to  $2/3.5$  of the original value, resulting in an  $\text{O}_{1s}/\text{Ta}_{4f}$  area of 0.252 (non-ammonolyzed) and 0.257 (pyrochlore).

An increase in flow velocity or reaction time caused a decrease in the  $O_{1s}$  peak area. Films synthesized at 5 cm/min  $NH_3$  flow (950C, 5hrs) or at 2 cm/min  $NH_3$  flow (950C, 20hrs) showed a nearly ideal  $O_{1s}/Ta_{4f}$  peak area.

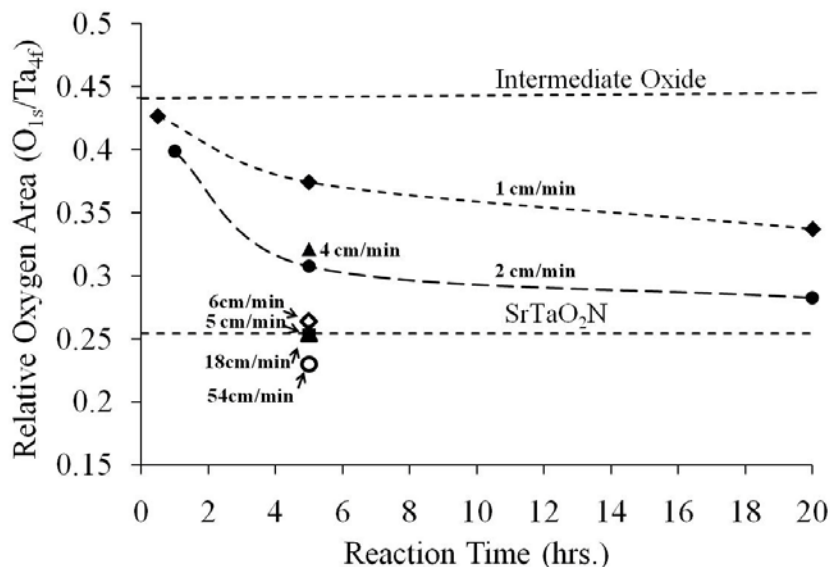


**Figure 6.3.2.2a** The relative  $O_{1s}/Ta_{4f}$  peak area as a function of reaction time at different flow velocities. Film surface was removed via  $Ar^+$  sputter (3keV  $Ar^+$ , 1x1mm, 0.3min per cycle, 3 cycles, estimated sputter removal of ~40-50nm) The ideal peak area is for  $SrTaO_2N$ .

Combining the nitrogen (from WDS) and estimated oxygen (from XPS) concentrations provides an anion stoichiometry of  $SrTaO_{2.22}N_{1.04}$ ,  $SrTaO_{1.99}N_{1.11}$ ,  $SrTaO_{2.08}N_{1.17}$ ,  $SrTaO_{2.00}N_{1.19}$  and  $SrTaO_{1.81}N_{1.18}$  for S. 2-20, S. 5-5, S. 6-5, S. 18-5 and S. 54-5 films, respectively. A comparison of films to two  $SrTaO_2N$  powders synthesized by a solid-state ceramic method ( $SrTaO_{2.02}N_{1.12}$  and  $SrTaO_{1.94}N_{1.18}$ ) reveals similar anion concentrations. Powder compositions were determined via LECO, hot-gas extraction and each powder underwent a similar ammonolysis treatment (rotary-calcining furnace, 1000°C, 20hrs, 54cm/min,  $Ta_3N_5$  impurities <0.5wt%). However, with films the oxygen

concentration consists of only ~10nm of the film depth. Therefore, the entire film was evaluated for compositional homogeneity with sputter depth profiling in XPS analysis (sec. 6.3.3.2).

### 6.3.3 Phase Homogeneity (C3)

#### 6.3.3.1 EDS Analysis

To test for lateral compositional homogeneity, multiple EDS scans at different positions were performed on reduced areas (estimated beam diameter of less than ~250nm) of the S. 2-5 and S. 6-5 films. (Tables 6.3.3.1a & b) Variation was within equipment tolerance and therefore, no heterogeneity was observed.

**Table IX.** EDS, Compositional Results on Reduced Areas of the S. 2-1 Film

Location	Nitrogen Content
Corner (1)	0.41
Corner (2)	0.44
Center-Edge (1)	0.49
Center-Edge (2)	0.41
Center-Edge (3)	0.43
Center (1)	0.47
<u>Average</u>	<u>0.44</u>
<u>Std. Dev.</u>	<u>0.032</u>

**Table X.** EDS, Compositional Results on Reduced Areas of the S. 6-5 Film

Location	Nitrogen Content
Corner (1)	1.24
Corner (2)	1.18
Center-Edge (1)	1.16
Center-Edge (2)	1.19
Center-Edge (3)	1.13
Center (1)	1.21
<u>Average</u>	<u>1.18</u>
<u>Std. Dev.</u>	<u>0.040</u>

### 6.3.3.2 XPS Analysis

Sputter profiling in XPS investigated compositional homogeneity throughout the entire film thickness in films S. 18-5 and S. 1-20. S. 18-5 had stable concentrations after removal of the top surface. (**Figure 6.3.3.2a**) The S. 1-20 film had stable cation levels, diminished nitrogen content and an increase in oxygen content as a function of increasing film depth. (**Figure 6.3.3.2b**)

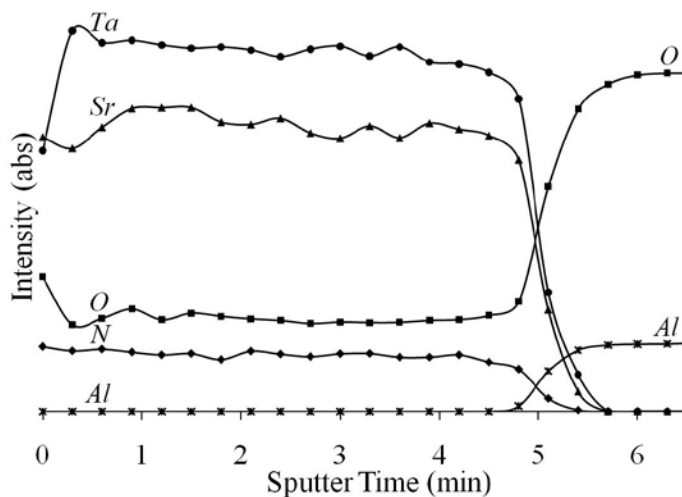


**Figure 6.3.3.2a** XPS sputtering profile of the S.18-5 film (3keV Ar<sup>+</sup>, 1x1mm, 0.3min per cycle) & (950°C, 5hrs, 18cm/min).

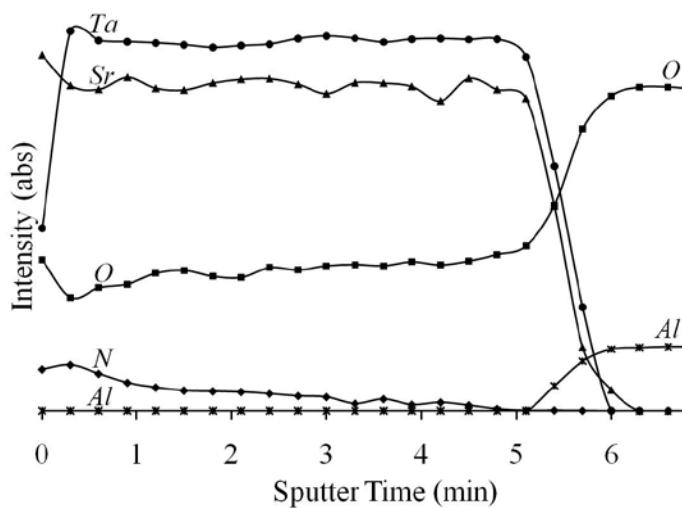


**Figure 6.3.3.2b** XPS sputtering profile of the S.1-20 film (3keV Ar<sup>+</sup>, 1x1mm, 0.3min per cycle) & (950°C, 20hrs, 1cm/min).

Interestingly, the strontium and oxygen concentrations decreased and tantalum concentration increased after removal of the film surface. It is possible the surface is enriched in strontium and oxygen. Similar observations are shown for titanium with BaTiO<sub>3</sub>, where BaCO<sub>3</sub> is the primary surface entity.<sup>57</sup> Alternatively, results could be an

artifact of depth profiling. Since, preferential sputtering would leave increased concentrations of the heaviest and most refractory element, i.e. tantalum. However, this is not consistent with elemental concentrations at the interface (in figures 13 and 14), where strontium and tantalum decrease in tandem with tantalum reaching a zero concentration first. If preferential sputtering existed, residual tantalum would be expected. The increasing O/N ratio as a function of depth for the S. 1-20 film is attributed to limited exposure of  $\text{NH}_3$  in the inner depths of the film. Consequently, higher flow should be used to promote an anion-exchange reaction prior to film densification. A high film density creates a kinetic barrier to gas transport and thus, extends the nitridation reaction time.

#### **6.3.4 Valence State (C4)**

##### **6.3.4.1 XPS Analysis**

To correctly characterize electronic properties, it is important to identify elemental valence states. This is accomplished via XPS. Also, the effect of nitrogen on lattice  $\text{Sr}_{3d}$  and  $\text{Ta}_{4f}$  environments was investigated. Results could reveal multiple phases (e.g. perovskite oxide and oxynitride) at intermediate nitrogen levels that could not be resolvable via XRD.

The  $\text{Sr}_{3d}$  peaks indicated multiple chemical states. (**Figure 6.3.4.1a**) Comparing  $\text{Sr}_{3d}$  spectrums of the oxynitride films to  $\text{SrTaO}_{3.5}$  powder confirms the low BE state as a  $\text{Sr}^{2+}$  lattice entity. Where, the high BE state is ascribed to a surface layer, since the concentration does not change as a function of nitrogen content ( $\text{N}_{1s}/\text{Ta}_{4f}$ ). (**Figure 6.3.4.1b**) A nitrogen exchange caused a slight reduction in the lattice  $\text{Sr}_{3d}$  binding

energy, where a fully nitrated structure shifted the  $Sr_{3d}$  peak by 0.23eV. (not shown) The  $Ta_{4f}$  environment had a different response.

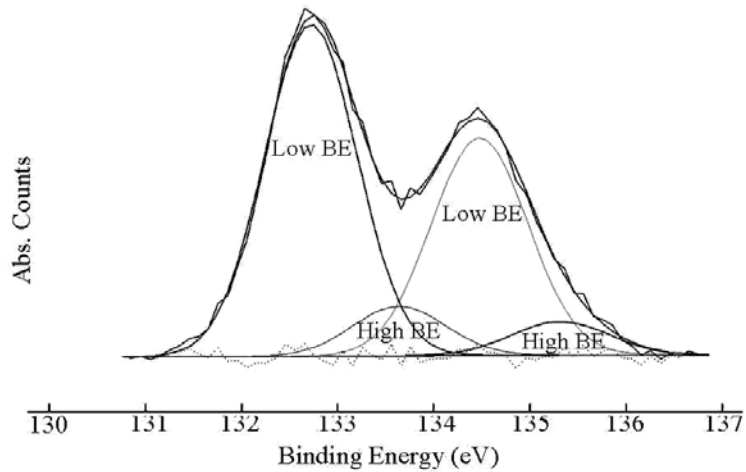


**Figure 6.3.4.1a** Deconvolution of the  $Sr_{3d}$  environment.

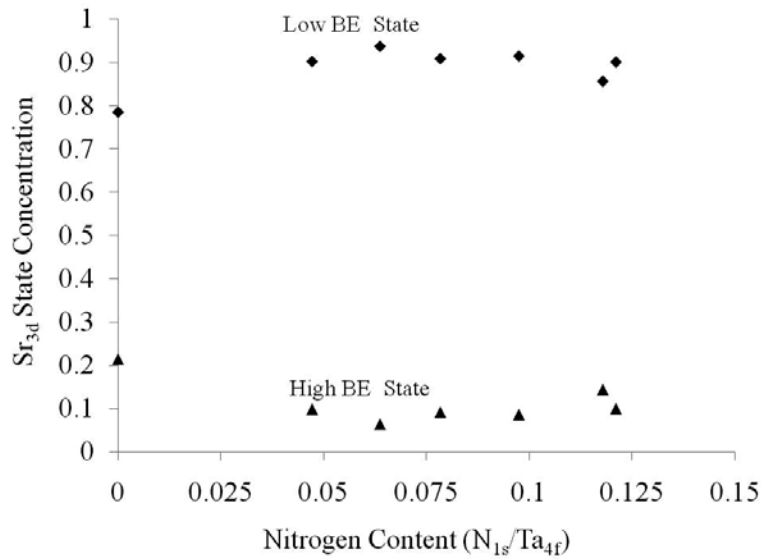


**Figure 6.3.4.1b** Concentration of each  $Sr_{3d}$  state as a function of XPS-derived nitrogen content.

A relationship between nitrogen content and the  $Ta_{4f}$  peak shape was observed.

(**Figure 6.3.4.1c**) At intermediate nitrogen levels, peaks showed broadened features

compared to the pure oxide. As nitrogen content further increased, a high energy shoulder became detectable (indicated with a solid arrow on figure 6.3.4.1c). Extrapolation of the intermediate oxide peak positions assigns the high BE state to an oxide environment (indicated with dotted lines on figure 6.3.4.1c). Therefore, the broadened peak features (at intermediate nitrogen contents) can be associated with overlap of multiple states. For example, fitting of the Ta<sub>4f</sub> environment with only two peaks (one state) created an excessive FWHM and an incorrect area ratio (b/t 5/2 and 7/2 orbitals). Addition of another state (four peaks total) provided a good fit (via a low chi square value) with peak area ratios, FWHM and BE separations correlating well to the pre-determined values from SrTaO<sub>3.5</sub> and SrTaO<sub>2</sub>N powders, as well as those in literature. Representative fits are shown in **figures 6.3.4.1d-g**.

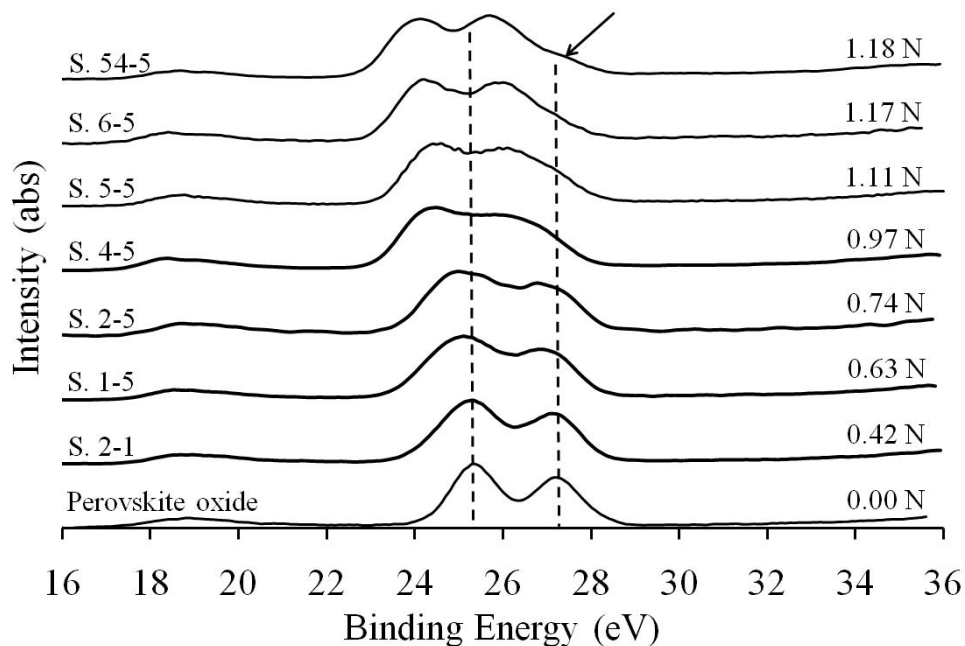


**Figure 6.3.4.1c** Ta<sub>4f</sub> environment as a function of nitrogen content and flow conditions. The arrow and dotted lines correspond to discussional points in the text.

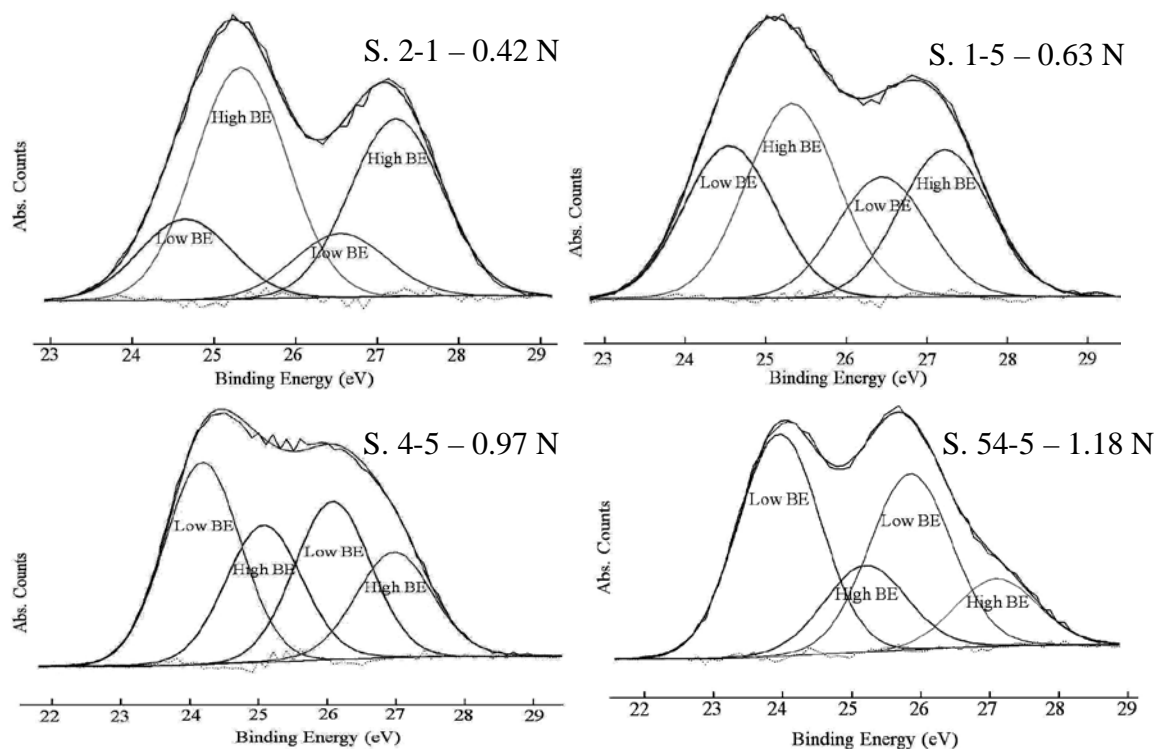


**Figure 6.3.4.1d-g** Deconvolution of the Ta<sub>4f</sub> environment for films with various nitrogen content (nitrogen content (N) refers to values derived from WDS).

The high BE state is assigned to Ta<sup>+5</sup> bound to oxygen. To determine the origin of the oxide (as either a residual oxide environment from an incomplete ammonolysis reaction or a surface entity), the concentration of each state as a function of nitrogen content was examined. (**Figure 6.3.4.1h**) As nitrogen levels become greater, content of the low and high BE states increase and decrease, respectively. Therefore, the high BE environment is attributed to a residual oxide state from an incomplete nitride reaction. However, the oxide is never completely eliminated. This limited concentration can be attributed to a surface entity. Assignment of the low BE state is more involved.

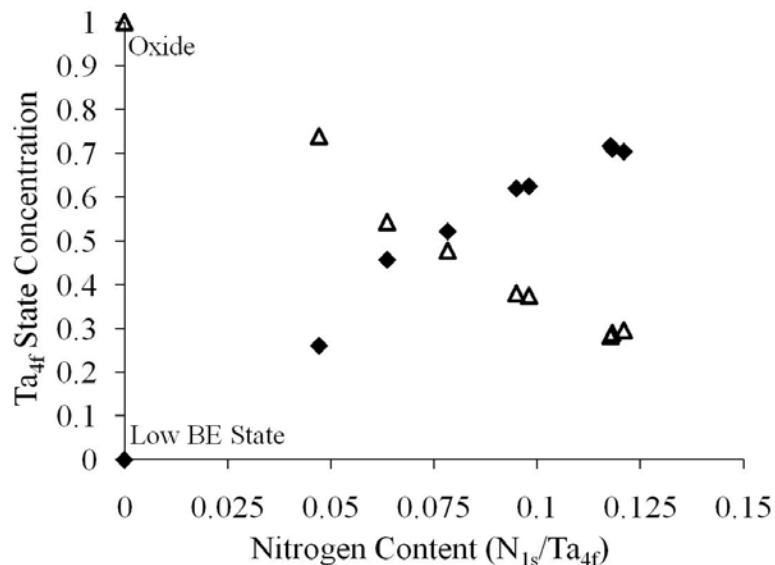


**Figure 6.3.4.1h** Concentration of each Ta<sub>4f</sub> state as a function of XPS-derived nitrogen content.

The low BE environment could arise from a reduction in the tantalum valence state (e.g. Ta<sup>+5</sup> to Ta<sup>+4</sup>) or from a change in chemical environment following a nitrogen exchange. Further insight is gained through comparing results with literature and to SrTaO<sub>2</sub>N powder samples from previous work (Chp. 3). Powder showed similar Ta<sub>4f</sub> environments and an anion composition determined from LECO hot-gas extraction that was approximately stoichiometric, SrTaO<sub>2.02</sub>N<sub>1.12</sub>. (**Figure 6.3.4.1i**) Since the chemistry correlates to Ta<sup>5+</sup>, it is assumed the low BE state does not result from a change in valence.

In addition, literature has pointed to a similar BE decrease upon nitridation of Ta<sub>2</sub>O<sub>5</sub>.<sup>41</sup> Where, conversion to Ta<sub>3</sub>N<sub>5</sub> resulted in a 1.6eV lower Ta<sub>4f</sub> BE state. In current work, the lower BE state is at 1.43eV from the intermediate oxide. Therefore, it is not unreasonable that the low BE state arises from nitrogen incorporation.

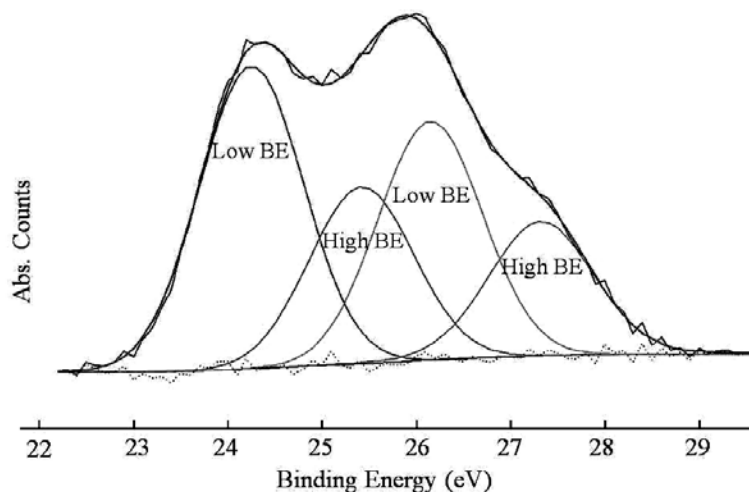


**Figure 6.3.4.1i** Deconvolution of the Ta<sub>4f</sub> environment for a solid-state synthesized SrTaO<sub>2</sub>N powder (Low BE=oxynitride, High BE=oxide).

The BE of each state as a function of nitrogen content is shown in **figure 6.3.4.1j**. As nitrogen levels increased, the oxide state changed minimally and the oxynitride state moved to lower energy. It seems the oxynitride environment is primarily affected by nitrogen incorporation.

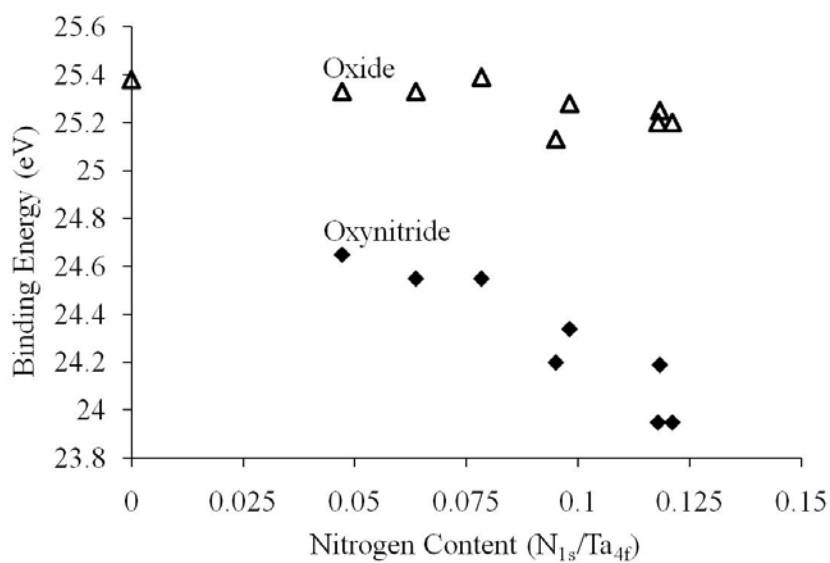


**Figure 6.3.4.1j** Binding energy for each Ta<sub>4f</sub><sup>7/2</sup> state as a function of XPS-derived nitrogen content.

Interestingly, the oxide to oxynitride conversion resulted in two Ta<sub>4f</sub> lattice environments with a significant reduction in the BE of the Ta<sub>4f</sub> peaks (~1.43eV). Where, the Sr<sub>3d</sub> environment shows only one state and a slight decrease in BE (~0.23eV). It is plausible the electronic structure of Sr<sup>2+</sup> and O<sup>2-</sup> do not undergo significant change. This is rationalized since Sr<sup>2+</sup> and O<sup>2-</sup> have high ionic character and an almost complete transfer of valence electrons. Therefore, a minimal dependence on chemistry and structure can be expected; however, Ta<sup>5+</sup> (and other transition metals) has partial covalent character and higher electronic polarizability and thus provides high sensitivity to changes in chemical environment.<sup>58</sup>

Reproducing films revealed variability in the Ta<sub>4f</sub> chemical environment via XPS. A few films showed an additional state at low BE (marked in **Figure 6.3.4.1k** as “new state”). Multiple phases were not observed with XRD.

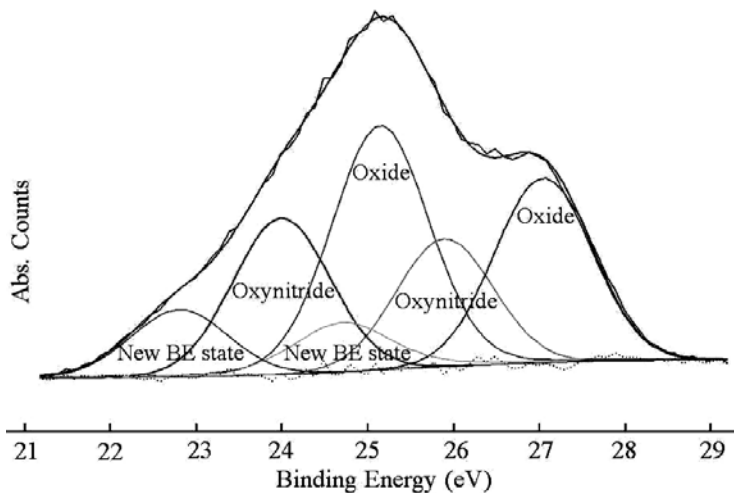


**Figure 6.3.4.1k** Deconvolution of the Ta<sub>4f</sub> environment of a S. 18-5 film with a new, lower BE state (950°C, 5hrs, 18cm/min).

Possible theories on the origin of the new environment are:

- 1.) A locally reduced valence state
- 2.) Clustered anion vacancies
- 3.) Low concentration minor phase

Examining relative areas of each state indicate a decline in area of the Ta<sub>4f</sub> oxynitride environment, compared to samples without the new BE state (refer to figures 17a-d). Hence, it seems the Ta<sub>4f</sub> oxynitride state is reduced in concentration and/or valence. One plausible explanation is the presence of a TaN<sub>x</sub> phase. For example, the new state is 1.19 eV lower in BE than the oxynitride state. Literature has noted a similar shift of ~1.2eV upon reduction of Ta<sub>3</sub>N<sub>5</sub> to TaN<sub>x</sub> with a valence state of ~Ta<sup>4+</sup>.<sup>43</sup> Alternatively, a Ta<sup>4+</sup> state could reside within the perovskite structure, since no minor phases were observed in XRD. Further work is merited to distinguish between these alternatives.

### **6.3.5 Microstructure (C5)**

#### **6.3.5.1 SEM Analysis**

A high flow and low reaction time resulted in films with smaller grains and higher density, compared to extended reaction time at low flow. Representative images are shown in **figures 6.3.5.1a-c**. No observable change in compositional homogeneity was observed via back-scatter contrast. The fracture surface of a SrTaO<sub>2</sub>N film with layer depositions reveals a relatively dense film. (**Figure 6.3.5.1d**)

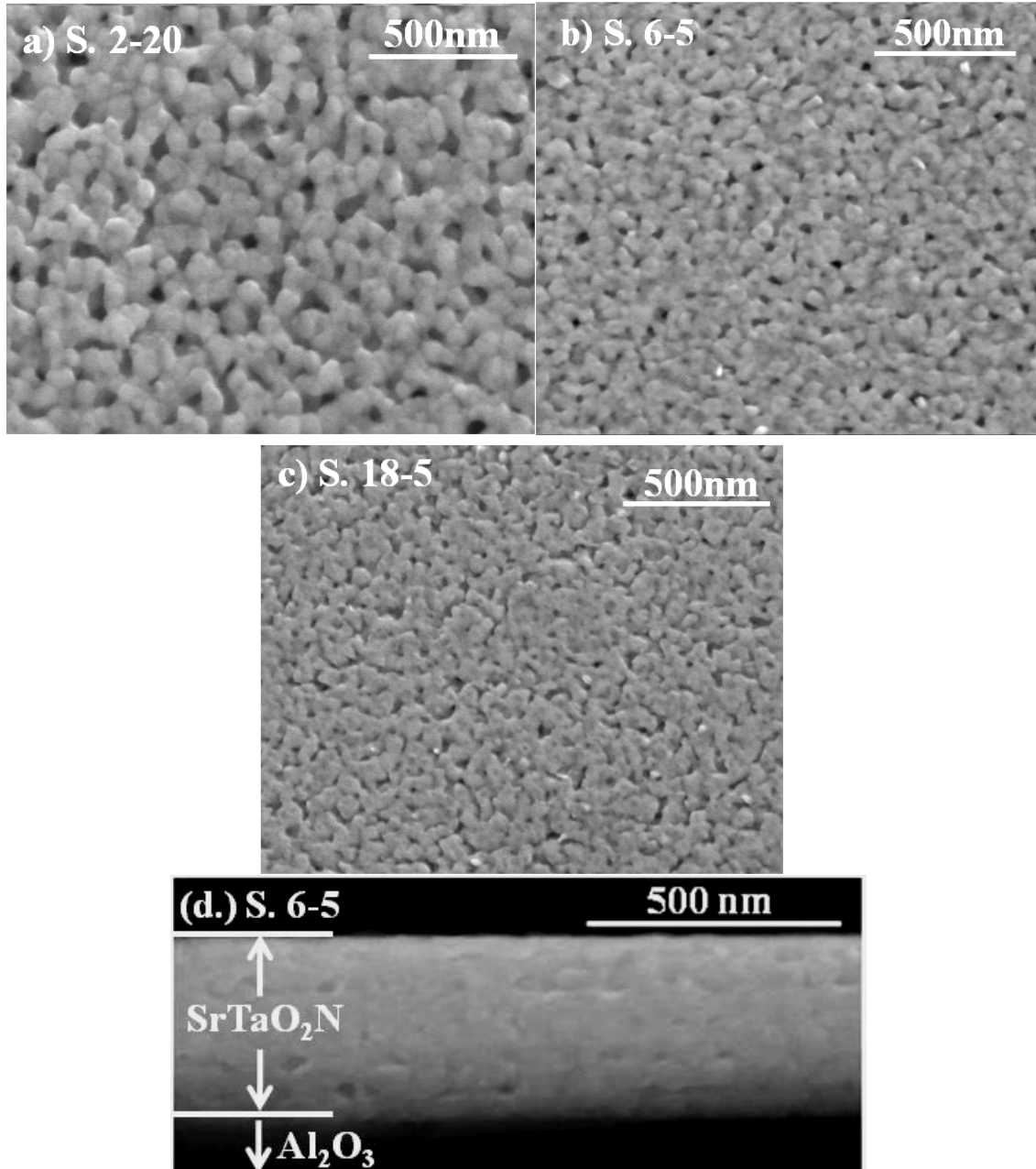


**Figure 6.3.5.1a-c** Secondary images of SrTaO<sub>2</sub>N films at varying flow velocity (950°C, 5hrs) and **(d)** cross-section of a fractured film with 7 layer depositions (S. 6-5).

It is possible the extended reaction time for S. 2-20 promoted grain coarsening. Alternatively, the formation of the SrTaO<sub>2</sub>N phase during earlier stages of synthesis with sample S. 18-5 could inhibit grain growth. This is understood since, nitrides typically have lower ionic mobility compared to oxides from the greater covalent character.

## 4.0 Conclusion

This paper had two objectives: optimize reaction conditions for fabricating phase-pure SrTaO<sub>2</sub>N films and discuss a potential mechanism for production of a SrTaO<sub>x</sub>N<sub>y</sub> phase.

### 4.1 Optimized Reaction Conditions

Temperature should be kept below 1000°C to ensure structural stability of the oxynitride and above 900°C to enhance reaction kinetics and increase grain size (refer to sec. 1.0). The lower limit on flow velocity (<6cm/min) is set by reaction rate (sec. 6.3.1.1 & sec. 6.3.2.1). At a low flow velocity the concentration of active nitriding species in the atmosphere is limited, increasing reaction time to fully nitride samples. Caution should also be taken to ensure an ideal oxygen stoichiometry (sec. 6.3.2.2), consistent anion composition through the film thickness (sec. 6.3.3.2) and stabilization of a Ta<sup>+5</sup> valence state (sec. 6.3.4.1). Additionally, it seems possible to control film microstructure through changing NH<sub>3</sub> reaction conditions. A higher flow and lower reaction time produced smaller grains and a denser film (sec. 6.3.5).

Based on these observations, reaction conditions for oxynitride film production are: 950°C, sample position at 4cm from the gas inlet with either an NH<sub>3</sub> flow velocity of ≥2cm/min for 20 hours or ≥6cm/min for 5 hours. Films had a smooth-dense microstructure, a single perovskite phase, homogeneous anion composition (laterally and through the film thickness) and no indication of oxygen deficiency or metallic reduction. However, nitrogen content in films was higher than expected (~1.18). Comparison of films to literature with SrTaO<sub>2</sub>N powder indicates similar perovskite cell volumes, anion compositions and color (orange). On the contrary, films with ~1.00 nitrogen content had

a green color and a lower than expected cell volume. Therefore, it is believed films synthesized under the selected reaction conditions have lattice nitrogen levels similar to SrTaO<sub>2</sub>N powders reported in literature.

#### **4.2 Mechanism for producing a SrTaO<sub>x</sub>N<sub>y</sub> phase**

Results indicate a possible perovskite structure able to sustain variable anion composition, SrTaO<sub>x</sub>N<sub>y</sub> (A). Alternatively, multiple phases could exist that were not observable in XRD from peak overlap, since the oxide (Sr<sub>0.7</sub>TaO<sub>3</sub>) and oxynitride (SrTaO<sub>2</sub>N<sub>y</sub>) have similar crystal structures (B).

Examining the Ta<sub>4f</sub> BE shift as a function of nitrogen concentration (figure 15) provides a possible means for discerning between these alternatives: (A) single phase (SrTaO<sub>x</sub>N<sub>y</sub>) or (B) two-phase system (SrTaO<sub>2</sub>N-Sr<sub>0.7</sub>TaO<sub>3</sub>). In a two-phase system (B), the defined anion ratio for the oxynitride (at 2N<sup>3-</sup>:4O<sup>2-</sup>) results in a set Ta<sub>4f</sub> BE and chemical environment. In this case, an increase in nitrogen concentration does not change the Ta<sub>4f</sub> environment (or BE) and only increases the concentration of the Ta<sub>4f</sub>-oxynitride state. With a single phase (A), a nitrogen increase would lower the Ta<sub>4f</sub> BE of the oxynitride state from a change in the anion ratio and thus, tantalum chemical environment. Therefore, the decrease in the Ta<sub>4f</sub>-oxynitride BE as nitrogen content increases (figure 15) is suggestive of a single perovskite with variable anion composition (A).

Findings signify dramatic change in the Ta<sup>+5</sup> electronic environment within a single perovskite phase. This could be induced through the lower N<sup>3-</sup> electronegativity (3.04), compared to O<sup>2-</sup> (3.44), therefore causing greater covalency and lower electronic polarizations.<sup>59</sup> In addition, Feng et al showed with first principle-DFT calculations that

in a similar compound, BaTaO<sub>2</sub>N, the tantalum ion displaces 0.1 Å towards nitrogen.<sup>60</sup> It is possible that this displacement could also contribute to the lower BE tantalum environment, since literature has pointed to a similar relationship between bond distance and binding energy.<sup>61</sup>

For a perovskite with variable anion composition, various electrical compensation mechanisms can be envisioned:

E1) Cation vacancies

E2) Anion interstitials (e.g. N<sup>x</sup>, O<sup>2-</sup>, CO<sup>2-</sup>)

E3) Metallic reductions (e.g. Ta<sup>5+</sup> to Ta<sup>4+</sup>)

For E2, no presence of additional anion peaks, besides those ascribed to lattice entities in the perovskite phase or an adsorbed surface layer, were observed. For E3, the Ta<sub>4f</sub> environment did not indicate a reduction in valence in low nitrogen content films or high defect concentrations (O<sub>N</sub><sup>·</sup>). Therefore, E2 and E3 are not considered plausible electrical compensation mechanisms. Literature proposed the intermediate oxide to be a cation-defect structure. Hence, results suggest E1 as means for achieving electrical neutrality.

Investigation into the proposed variable anion composition perovskite (SrTaO<sub>x</sub>N<sub>y</sub>) could prove to be an exciting avenue for tailoring electrical properties and resistivity. Bud et al. showed the intermediate perovskite oxide to have low dielectric loss and low permittivity. Perovskite oxynitrides demonstrate high permittivity and high loss factors. Optimization of anion chemistry could provide a favorable balance of properties. Additionally, it might be possible to control cation vacancy concentration for application as ionic conductors.

## REFERENCES

1. Y.-I. Kim, P.M. Woodward, K.Z. Baba-Kishi, and C.W. Tai, "Characterization of the Structural, Optical, and Dielectric Properties of Oxynitride Perovskites  $AMO_2N$  (A=Ba, Sr, Ca; M = Ta, Nb)." *Chem. Mater.*, **16** [7] 1267-76 (2004).
2. X. Gouin, R. Marchand, and Y. Laurent, "Infrared Dielectric Response of  $BaTaO_2N$ ," *Solid State Commun.*, **93** [10] 857-9 (1995).
3. M. Jansen and H.P. Letschert, "Inorganic Yellow-Red Pigments without Toxic Metals," *Nature*, **404** [6781] 980-2 (2000).
4. M. Higashi, R. Abe, T. Takata, and K. Domen, "Photocatalytic Overall Water Splitting under Visible Light Using  $ATaO_2N$  (A=Ca,Sr,Ba) and  $WO_3$  in a  $IO_3^-/I^-$  Shuttle Redox Mediated System," *Chem. Mater.*, **21** [8] 1543-9 (2009).
5. R. Marchand, F. Pors, Y. Laurent, O. Regreny, J. Lostec, and J.M. Haussonne, "Perovskites Oxynitruées Utilisées en tant que Matériaux Dielectriques," *J. Phys., Colloq.*, **47** [2] 901-5 (1986).
6. R. Caracas and R.E. Cohen, "Prediction of Polar Ordered Oxynitride Perovskites," *Appl. Phys. Lett.*, **91** [9] 1-3 (2007).
7. R. Marchand, Y. Laurent, J. Guyader, P. L'Haridon, and P. Verdier, "Nitrides and Oxynitrides: Preparation, Crystal Chemistry and Properties," *J. Eur. Ceram. Soc.*, **8** [4] 197-213 (1991).
8. R. Marchand, F. Pors, and Y. Laurent, "Elaboration and Characterization of New Oxynitrides with a Perovskite Structure," *Rev. Int. Hautes Temp. Refract.*, **23** [1] 11 (1986).
9. E. Gunther, R. Hagenmayer, and M. Jansen, "Structural Investigations on the Oxidinitrides  $SrTaO_2N$ ,  $CaTaO_2N$  and  $LaTaON_2$  by Neutron and X-ray Diffraction," *J. Inorg. Chem.*, **626** [7] 1519-25 (2000).
10. C.F. Floe, "Section III: The Floe Nitriding Process - A Study of the Nitriding Process Effect of Ammonia Dissociation on Case Depth And Structure," pp. 144-71 in *Source Book on Nitriding*. American Society for Metals, Metals Park, OH, 1977.
11. M. Katsura, "Thermodynamics of Nitride and Hydride Formation by the Reaction of Metals with Flowing  $NH_3$  " *J. Alloys Compd.*, **182** [1] 91-102 (1992).
12. M.W. Chase Jr., C.A. Davies, J.R. Downey Jr., D.J. Frurip, R.A. McDonald, and A.N. Syverud, *JANAF Thermochemical Tables Third Edition - Part II, Cr-Zr*,

Vol. 14,; p. 1530. American Chemical Society and American Institute of Physics, New York, 1985.

13. K.T. Jacob, R. Verma, and M. Mallya, "Nitride Synthesis Using Ammonia and Hydrazine-a Thermodynamic Panorama," *J. Mater. Sci.*, **37** [20] 4465-72 (2002).
14. D. Pye, *Practical Nitriding and Ferritic Nitrocarburizing*; pp. 50-1. ASM International, Materials Park, OH, 2003.
15. F. Pors, P. Bacher, R. Marchand, Y. Laurent, and G. Roult, "Neutron Diffraction Structural Study of the SrTaO<sub>2</sub>N Oxynitride Perovskite and of the Ba<sub>1-x</sub>Sr<sub>x</sub>TaO<sub>2</sub>N Solid Solution," *Rev. Int. Hautes Temp. Refract.*, **24** [4] 239-46 (1988).
16. A. Rachel, S. G. Ebbinghaus, M. Gungerich, P.J. Klar, J. Hanss, A. Weidenkaff, and A. Reller, "Tantalum and Niobium Perovskite Oxynitrides: Synthesis and Analysis of the Thermal Behaviour," *Thermochim. Acta*, **438** [1-2] 134-43 (2005).
17. Y.-I. Kim and P.M. Woodward, "Syntheses and Characterizations of Complex Perovskite Oxynitrides LaMg<sub>1/3</sub>Ta<sub>2/3</sub>O<sub>2</sub>N, LaMg<sub>1/2</sub>Ta<sub>1/2</sub>O<sub>5/2</sub>N<sub>1/2</sub>, and BaSc<sub>0.05</sub>Ta<sub>0.95</sub>O<sub>2.1</sub>N<sub>0.9</sub>," *J. Solid State Chem.*, **180** [11] 3224-33 (2007).
18. R. Marchand, F. Tessier, A.L. Sauze, and N. Diot, "Typical Features of Nitrogen in Nitride-Type Compounds," *Int. J. Inorg. Mater.*, **3** [8] 1143-6 (2001).
19. R. Aguiar, D. Logvinovich, A. Weidenkaff, A. Reller, and S.G. Ebbinghaus, "Thermal Oxidation of Oxynitride Perovskites in Different Atmospheres," *Thermochim. Acta*, **471** [1-2] 55-60 (2008).
20. E. Atanassova and D. Spassov, "X-ray Photoelectron Spectroscopy of Thermal Thin Ta<sub>2</sub>O<sub>5</sub> Films on Si," *Appl. Surf. Sci.*, **135** [1-4] 71-82 (1998).
21. B.V. Crist, "Advanced Peak-Fitting of Monochromatic XPS Spectra," *J. Surf. Anal.*, **4** [3] 428-34 (1998).
22. C.D. Wagner, A.V. Naumkin, A. Kraut-Vass, J.W. Allison, C.J. Powell, and J.R. Rumble, "NIST X-ray Photoelectron Spectroscopy Database, Version 3.5 " (2003) National Institute of Standards and Technology. Accessed on: December 2010. Available at <<http://srdata.nist.gov/xps/>>
23. R.D. Shannon, "Revised Effective Ionic Radii and Systematic Studies of Interatomic Distances in Halids and Chalcogenides," *Acta Crystallogr., Sect. A*, **32** [5] 751-67 (1976).
24. J. Grins and G. Svensson, "Synthesis of Oxynitride Perovskites [AZr<sub>x</sub>Ta<sub>1-x</sub>O<sub>2+x</sub>N<sub>1-x</sub> A=Ca,Sr,Ba and 0<x<1]," *Mater. Res. Bull.*, **29** [7] 801-9 (1994).

25. J. Etourneau, J. Portiera, and F. Menilb, "The Role of the Inductive Effect in Solid State Chemistry; How the Chemist Can Use it to Modify both the Structural and the Physical Properties of the Materials.," *J. Alloys Compd.*, **188** [19] 1-7 (1992).
26. F. Tessier and R. Marchand, "Ternary and Higher Order Rare-Earth Nitride Materials: Synthesis and Characterization of Ionic-Covalent Oxynitride Powders," *J. Solid State Chem.*, **171** [1-2] 143-51 (2003).
27. F. Chevire, F. Tessier, and R. Marchand, "Optical Properties of the Perovskite Solid Solution  $\text{LaTiO}_2\text{N-A}\text{TiO}_3$  (A = Sr, Ba)," *Eur. J. Inorg. Chem.*, **2006** [6] 1223-30 (2006).
28. M.W. Chase Jr., C.A. Davies, J.R. Downey Jr., D.J. Frurip, R.A. McDonald, and A.N. Syverud, *JANAF Thermochemical Tables Third Edition - Part I, Al-Co*, Vol. 14.,; pp. 350,713. American Chemical Society and American Institute of Physics, New York, 1985.
29. M. Lerch, J. Janek, K.D. Becker, S. Berendts, H. Boysen, T. Bredow, R. Dronskowski, S.G. Ebbinghaus, M. Kilo, M.W. Lurney, M. Martin, C. Reimann, E. Schweda, I. Valov, and H.D. Wiemhofer, "Oxide Nitrides: From Oxides to Solids with Mobile Nitrogen Ions," *Prog. Solid State Chem.*, **37** [2-3] 81-131 (2009).
30. V.M. Goldschmidt, *V. M. Matem Naturvid Klasse*, **2**, 97 (1926). As cited in H. Wolff and R. Dronskowski, "First-Principles and Molecular-Dynamics Study of Structure and Bonding in Perovskite-Type Oxynitrides  $\text{ABO}_2\text{N}$  (A=Ca, Sr, Ba; B=Ta, Nb)," *J. Comput. Chem.*, **29** [13] 2260-7 (2008).
31. Y.H. Han, J.B. Appleby, and D.M. Smyth, "Calcium as an Acceptor Impurity of Barium Titanate ( $\text{BaTiO}_3$ ).," *J. Am. Ceram. Soc.*, **70** [2] 96-100 (1987).
32. Y. Masuda, R. Mashima, M. Yamada, K. Ikeuchi, K.-i. Murai, G.I.N. Waterhouse, J.B. Metson, and T. Moriga, "Relationship Between Anion and Cation Nonstoichiometries and Valence State of Titanium in Perovskite-Type Oxynitrides  $\text{LaTiO}_2\text{N}$ ," *J. Ceram. Soc. Jpn.*, **117** [1] 76-81 (2009).
33. R. Aguiar, A. Weidenkaff, C.W. Schneider, A. Reller, and S.G. Ebbinghaus, "Synthesis and Properties of Oxynitrides  $(\text{La,Sr})\text{Ti}(\text{O,N})_3$  Thin Films," *Prog. Solid State Chem.*, **35** [2-4] 291-8 (2007).
34. G. Will, "1.2.10 Line Broadening: Crystallite Size, Strain and Stress," pp. 37-9 in *Powder Diffraction: The Rietveld Method and the Two-Stage Method*. Springer, New York, 2006.

35. B. Ohtani, Y. Ogawa, and S.-i. Nishimoto, "Photocatalytic Activity of Amorphous-Anatase Mixture of Titanium(IV) Oxide Particles Suspended in Aqueous Solutions," *J. Phys. Chem. B*, **101** [19] 3746-52 (1997).
36. N.E. Brese and M. O'Keeffe, "Crystal Chemistry of Inorganic Nitrides," *Struct. Bonding (Berlin)*, **79**, 309 (1992).
37. M. Billy, J.-C. Labbe, and P. Lortholary, "Stabilité Et Mécanisme De Décomposition Thermique Des Oxynitrides De Silicium Et De Germanium," *Mater. Chem.*, **4** [2] 189-200 (1979).
38. L. Le Gendre, R. Marchand, and B. Piriou, "Raman Scattering Investigations of Dinitrogen Entities in Oxidized LaTiO<sub>2</sub>N Perovskite," *Eur. J. Solid State Inorg. Chem.*, **34** [9] 973-82 (1997).
39. L. Le Gendre, R. Marchand, and Y. Laurent, "A New Class of Inorganic Compounds Containing Dinitrogen-Metal Bonds," *J. Eur. Ceram. Soc.*, **17** [15-16] 1813-8 (1997).
40. F. Tessier, L.L. Gendre, F. Chevire, R. Marchand, and A. Navrotsky, "Thermochemistry of a New Class of Materials Containing Dinitrogen Pairs in an Oxide Matrix," *Chem. Mater.*, **17** [13] 3570-4 (2005).
41. M. Hara, E. Chiba, A. Ishikawa, T. Takata, J.N. Kondo, and K. Domen, "Ta<sub>3</sub>N<sub>5</sub> and TaON Thin Films on Ta Foil: Surface Composition and Stability," *J. Phys. Chem. B*, **107** [48] 13441-5 (2003).
42. T. Hino, S. Mustofa, M. Nishida, and T. Araki, "The Effect of 5 Mass% O<sub>3</sub> Gas on PLD of Tantalum Oxide," *Appl. Surf. Sci.*, **189** [1-2] 1-6 (2002).
43. J.-S.M. Lehn, P.v.d. Heide, Y. Wang, S. Suh, and D.M. Hoffman, "A New Precursor for the Chemical Vapor Deposition of Tantalum Nitride Films," *J. Mater. Chem.*, **14** [21] 3239-45 (2004).
44. R.C. Mehrotra, *History of Precursors*; pp. 1-16. World Scientific, Singapore, 1989.
45. R.W. Schwartz, T. Schneller, and R. Waser, "Chemical Solution Deposition of Electronic Oxide Films," *C. R. Chim.*, **7** [5] 433-61 (2004).
46. M.P. Pechini, Sprague Electric Company, "Method of Preparing Lead and Alkaline Earth Titanates and Niobates and Coating Method Using the Same to Form a Capacitor," U.S. Pat. 3,330,697, 1967.
47. K. Nishio and T. Tshuchiya, "Sol-Gel Processing of Thin Films with Metal Salts," pp. 59-76 in *Handbook of Sol-gel Science and Technology: Processing*,

*Characterization, and Applications, Vol. 1.* Edited by H. Kozuka. Kluwer Academic New York, 2005.

48. V. Petrykin and M. Kakihana, "Chemistry and Applications of Polymeric Gel Precursors," pp. 77-103 in *Handbook of Sol-gel Science and Technology: Processing, Characterization, and Applications, Vol. 1.* Edited by H. Kozuka. Kluwer Academic New York, 2005.
49. T.J. Boyle and M.A. Rodriguez, Sandia Corporation, "Perovskite Phase Thin Films and Method of Making," U.S. Pat. 6,153,317, 2000.
50. M.A. Rodriguez, T.J. Boyle, B.A. Hernandez, D.R. Tallant, and K. Vanheusden, "A New Metastable Thin-Film Strontium Tantalate Perovskite," *J. Am. Ceram. Soc.*, **82** [8] 2101-5 (1999).
51. C. Le Paven-Thivet, L. Le Gendre, J. Le Castrec, F. Chevire, F. Tessier, and J. Pinel, "Oxynitride Perovskite  $\text{LaTiO}_x\text{N}_y$  Thin Films Deposited by Reactive Sputtering," *Prog. Solid State Chem.*, **35** [2-4] 299-308 (2007).
52. L.L. Gendre, C.L. Paven, J. Pinel, D. Fasquelle, J.C. Carru, F. Chevire, F. Tessier, and R. Marchand, "Lanthanum Titanium Oxynitride Thin Films," *Silic. Ind.*, **69** [5-6] 165-71 (2004).
53. S.G. Ebbinghaus, H.-P. Abicht, R. Dronskowski, T. Muller, A. Reller, and A. Weidenkaff, "Perovskite-Related Oxynitrides - Recent Developments in Synthesis, Characterisation and Investigations of Physical Properties," *Prog. Solid State Chem.*, **37** [2-3] 173-205 (2009).
54. R. Aguiar, D. Logvinovich, A. Weidenkaff, H. Karl, C.W. Schneider, A. Reller, and S.G. Ebbinghaus, "Physical Properties of  $(\text{La,Sr})\text{Ti}(\text{O,N})_3$  Thin Films Grown by Pulsed Laser Deposition," *Mater. Res. Bull.*, **43** [6] 1376-83 (2008).
55. J.-C. Dupin, D. Gonbeau, P. Vinatier, and A. Levasseur, "Systematic XPS Studies of Metal Oxides, Hydroxides and Peroxides," *Phys. Chem. Chem. Phys.*, **2** [6] 1319-24 (2000).
56. D. Logvinovich, L. Bocher, D. Sheptyakov, R. Figi, S.G. Ebbinghaus, R. Aguiar, M.H. Aguirre, A. Reller, and A. Weidenkaff, "Microstructure, Surface Composition and Chemical Stability of Partly Ordered  $\text{LaTiO}_2\text{N}$ ," *Solid State Sci.*, **11** [8] 1513-9 (2009).
57. R. Lacey, "A Study of the Microchemistry of Nanocrystalline  $\text{BaTiO}_3$  with Tetragonal and Pseudocubic Room Temperature Symmetries"; Ph.D. Thesis. Alfred University, Alfred, NY, 2007.

58. V.V. Atuchin, J.-C. Grivel, and Z. Zhang, "Core Level Photoemission Spectroscopy and Chemical Bonding in  $\text{Sr}_2\text{Ta}_2\text{O}_7$ ," *Chem. Phys.*, **360** [1-3] 74-8 (2009).
59. L. Pauling, "The Nature of the Chemical Bond. IV. The Energy of Single Bonds and the Relative Electronegativity of Atoms," *J. Am. Chem. Soc.*, **54** [9] 3570-82 (1932).
60. C.M. Fang, G.A. de Wijs, E. Orhan, G. de With, R.A. de Groot, H.T. Hintzen, and R. Marchand, "Local Structure and Electronic Properties of  $\text{BaTaO}_2\text{N}$  with Perovskite-Type Structure," *J. Phys. Chem. Solids*, **64** [2] 281-6 (2003).
61. V.V. Atuchin, J.-C. Grivel, and Z. Zhang, "Core Level Photoemission Spectroscopy and Chemical Bonding in  $\text{Sr}_2\text{Ta}_2\text{O}_7$ ," *Chem. Phys.*, **360** [1-3] 74-8 (2009).